

NAVAL POSTGRADUATE SCHOOL

Monterey, California



DISSERTATION

**USE OF SHIP-MOUNTED ACOUSTIC DOPPLER
CURRENT PROFILER DATA TO
STUDY MESOSCALE OCEANIC CIRCULATION
PATTERNS IN THE ARCHIPIELAGO DE
COLON (GALAPAGOS ISLANDS)
AND THE GULF OF THE FARALLONES**

by

John M. Steger

June, 1997

Dissertation Supervisors:

Curtis A. Collins
Franklin B. Schwing

Approved for public release; distribution is unlimited.

19971105 040

REPORT DOCUMENTATION PAGE			Form Approved OMB No. 0704-0188	
Public reporting burden for this collection of information is estimated to average 1 hour per response, including the time for reviewing instruction, searching existing data sources, gathering and maintaining the data needed, and completing and reviewing the collection of information. Send comments regarding this burden estimate or any other aspect of this collection of information, including suggestions for reducing this burden, to Washington Headquarters Services, Directorate for Information Operations and Reports, 1215 Jefferson Davis Highway, Suite 1204, Arlington, VA 22202-4302, and to the Office of Management and Budget, Paperwork Reduction Project (0704-0188) Washington DC 20503.				
1. AGENCY USE ONLY (Leave blank)	2. REPORT DATE June 1997	3. REPORT TYPE AND DATES COVERED Ph.D. Dissertation		
4. TITLE AND SUBTITLE USE OF SHIP-MOUNTED ACOUSTIC DOPPLER CURRENT PROFILER DATA TO STUDY MESOSCALE OCEANIC CIRCULATION PATTERNS IN THE ARCHIPIELAGO DE COLON (GALAPAGOS ISLANDS) AND THE GULF OF THE FARALLONES		5. FUNDING NUMBERS		
6. AUTHOR(S) Steger, John M.				
7. PERFORMING ORGANIZATION NAME(S) AND ADDRESS(ES) Naval Postgraduate School Monterey CA 93943-5000		8. PERFORMING ORGANIZATION REPORT NUMBER		
9. SPONSORING/MONITORING AGENCY NAME(S) AND ADDRESS(ES)		10. SPONSORING/MONITORING AGENCY REPORT NUMBER		
11. SUPPLEMENTARY NOTES The views expressed in this thesis are those of the author and do not reflect the official policy or position of the Department of Defense or the U.S. Government.				
12a. DISTRIBUTION/AVAILABILITY STATEMENT Approved for public release; distribution is unlimited.		12b. DISTRIBUTION CODE		
13. ABSTRACT (maximum 200 words) Ship-mounted acoustic Doppler current profiler (ADCP) data are used to study regional ocean patterns around the biologically rich regions of the Archipiélago de Colón (Galápagos Islands) and the Gulf of the Farallones to test our assumptions about the circulation derived primarily from hydrographic samples. West of the Galapagos, an equatorial undercurrent transporting ~7 Sv was present in November 1993, which decelerated within 30 km of the archipelago, shoaled, and diverged with a strong deflection to the southwest. A method of removing tidal velocities from ADCP measurements by creating an empirical model of the tides and using it to predict and subtract the tides is described. It is shown that in the Gulf of the Farallones, a large number of observations, typically more than acquired on one cruise, are necessary to reduce tidal model error. Detided ADCP data are used to describe the circulation in the Gulf under various wind conditions. Over the continental slope, surface-to-depth poleward flow is present throughout the year. During wind relaxations, poleward flow strengthens and warmer, fresher water is transported onshore.				
14. SUBJECT TERMS ADCP, Galápagos Islands, South Equatorial Current, Equatorial Undercurrent, Gulf of the Farallones, California Current, California Undercurrent, Upwelling, Relaxation.			15. NUMBER OF PAGES 165	
			16. PRICE CODE	
17. SECURITY CLASSIFICATION OF REPORT Unclassified	18. SECURITY CLASSIFICATION OF THIS PAGE Unclassified	19. SECURITY CLASSIFICATION OF ABSTRACT Unclassified	20. LIMITATION OF ABSTRACT UL	

Approved for public release; distribution is unlimited.

**USE OF SHIP-MOUNTED ACOUSTIC DOPPLER CURRENT PROFILER DATA TO
STUDY MESOSCALE OCEANIC CIRCULATION PATTERNS
IN THE ARCHIPIELAGO DE COLON (GALAPAGOS ISLANDS)
AND THE GULF OF THE FARALLONES**

John M. Steger
Lieutenant Commander, National Oceanic and Atmospheric Administration
B.S., B.A., University of California at Irvine, 1985
M.S., University of Maryland at College Park, 1991

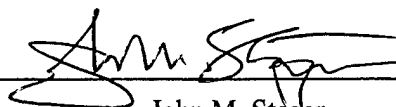
Submitted in partial fulfillment of the requirements for the degree of

DOCTOR OF PHILOSOPHY IN PHYSICAL OCEANOGRAPHY

from the
NAVAL POSTGRADUATE SCHOOL

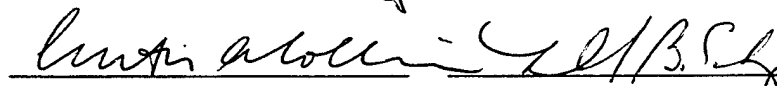
June 1997

Author:



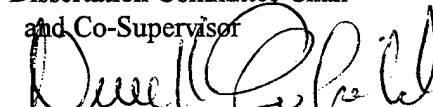
John M. Steger

Approved by:

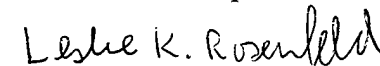


Curtis A. Collins
Professor of Oceanography
Dissertation Committee Chair
and Co-Supervisor

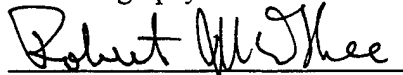
Franklin B. Schwing
Supervisory Oceanographer,
NOAA/NMFS
Dissertation Co-Supervisor



Newell Garfield
Research Assistant Professor of
Oceanography

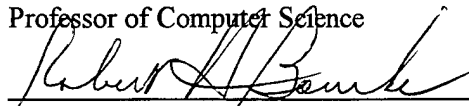


Leslie K. Rosenfeld
Research Assistant Professor of
Oceanography



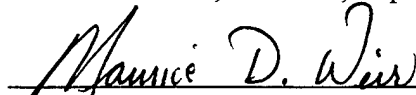
Robert McGhee
Professor of Computer Science

Approved by:



Robert H. Bourke, Chairman, Department of Oceanography

Approved by:



Maurice D. Weir, Associate Provost for Instruction

ABSTRACT

Ship-mounted acoustic Doppler current profiler (ADCP) data are used to study regional ocean patterns around the biologically rich regions of the Archipiélago de Colón (Galápagos Islands) and the Gulf of the Farallones to test our assumptions about the circulation derived primarily from hydrographic samples. West of the Galapagos, an equatorial undercurrent transporting ~ 7 Sv was present in November 1993, which decelerated within 30 km of the archipelago, shoaled, and diverged with a strong deflection to the southwest. A method of removing tidal velocities from ADCP measurements by creating an empirical model of the tides and using it to predict and subtract the tides is described. It is shown that in the Gulf of the Farallones, a large number of observations, typically more than acquired on one cruise, are necessary to reduce tidal model error. Detided ADCP data are used to describe the circulation in the Gulf under various wind conditions. Over the continental slope, surface-to-depth poleward flow is present throughout the year. During wind relaxations, poleward flow strengthens and warmer, fresher water is transported onshore.

TABLE OF CONTENTS

I. INTRODUCTION	1
II. CIRCULATION IN THE ARCHIPIELAGO DE COLON (GALAPAGOS ISLANDS), NOVEMBER, 1993	5
A. INTRODUCTION	5
B. MEASUREMENTS	8
C. EL NIÑO CONDITIONS	11
D. RESULTS	12
1. 89°W	12
2. 91.75°W	21
3. 92°W	21
4. 93°W	23
5. 93.5°W	23
6. 94°W	24
7. 0.25°S	24
E. SPATIAL VARIABILITY	25
1. Surface (15 m)	26
2. EUC (75 m)	26
F. TIDAL VARIABILITY IN BOLIVAR CHANNEL	27
G. DISCUSSION	28
III. AN EMPIRICAL MODEL OF THE TIDAL CURRENTS IN THE GULF OF THE FARALLONES	35
A. INTRODUCTION	35
B. THE GULF OF THE FARALLONES	38
C. DATA	43
D. BUILDING THE EMPIRICAL TIDAL MODEL	46
E. RESULTS	49
1. Case 1	49
2. Cases 2 and 3	52
3. Case 4	56
4. Case 5	56
5. Case 6	59
F. MODEL ACCURACY AND SENSITIVITY	59
G. CONCLUSION	70

IV. SEASONAL VARIABILITY OF THE CIRCULATION AND WATER MASSES IN THE GULF OF THE FARALLONES	71
A. INTRODUCTION	71
B. THE SLOPE/SHELF EXPERIMENT CRUISES	76
C. REGIONAL WIND/SST CLIMATOLOGY AND CONDITIONS IN 1991-92	80
D. VERTICAL SECTIONS OF TEMPERATURES AND SALINITIES IN 1991-92	84
E. ADCP AND CTD FIELDS	92
1. February 13-18, 1991	92
2. May 16-21, 1991	95
3. August 12-18, 1991	98
4. October 29 - November 3, 1991	99
5. 1991 Mean	104
6. February 7-17, 1992	107
F. TRANSPORTS AND RESIDENCE TIMES	109
1. Transports	109
2. Residence Times	119
G. DISCUSSION	119
1. Barotropic Poleward Flow	121
2. Equatorward Winds	124
3. Relaxation	125
4. Event-driven Mixing	129
H. APPLICATIONS TO DISPOSAL OF DREDGE SPOILS	129
I. SUMMARY	129
V. FUTURE WORK	131
APPENDIX A. CURRENT METERS IN THE GULF OF THE FARALLONES ...	133
APPENDIX B. CONSTRUCTING THE TIDAL MODEL	141
LIST OF REFERENCES	145
INITIAL DISTRIBUTION LIST	153

ACKNOWLEDGMENTS

I thank the NOAA Corps and the leadership at the NOAA Pacific Fisheries Environmental Laboratory for the opportunity to pursue this study. The daily guidance of Frank Schwing, the overall direction and encouragement of Curt Collins, and the help I received from all my committee members are *sincerely appreciated*. Marlene Noble, Steve Ramp, and Peter Chu were "extended committee members" who provided significant contributions. Laura Ehret and Mike Cook were very helpful with MATLAB and FORTRAN coding.

The IRONEX program was conceived by John Martin and supported by the Office of Naval Research. ADCP data were collected at sea by Jim Stockel, Vernon Anderson, Tim Stanton, and Curt Collins. Sea level data and associated tidal analyses were supplied by the University of Hawaii Sea Level Center.

Thanks to Julio Candela for early assistance and MATLAB code for running his tidal model. Paul Jessen, Tarry Rago, and Heather Parker processed the ADCP data used in this study. Discussions with John Largier were helpful, and he and Steve Costa supplied the current meter data from CH2M Hill. Kaye Kinoshita processed and furnished the SSE current meter data. Dan Larson and the Scripps Data Zoo were the source for CCCCS current meter data, and Joe Bottero resurrected the SuperCODE mooring data. Barbara Hickey shared her data from the RP3 mooring. Funding for the SSE was provided by the EPA and US Navy. Efforts of the master and crew of the R/V Point Sur and the R/V Iselin and the officers and crew of the NOAA Ship David Starr Jordan are gratefully acknowledged. "Data czar" Kenny Baltz was always available on the other side of the office partition to pawn data from and bounce ideas off of.

As the Beatles sang, I get by with a little help from my friends. Thanks a heap to all of them and to my family. Especially my father, to whom this is dedicated.

I. INTRODUCTION

The vast majority of what we know about ocean structure and circulation is what has been inferred from CTD and ocean bottle samples. However, in recent years a method of directly measuring velocity from a ship while underway has become available. The acoustic Doppler current profiler (ADCP) continuously measures a vertical profile of velocity beneath the ship, giving oceanographers the ability to see much more detail in the spatial and temporal character of currents. A better understanding of currents and their variability is important for a variety of reasons; it may help to answer outstanding questions about how the ocean affects climate, how nutrients and larvae are transported, what happens to pollution in the ocean, how search and rescue operations should be coordinated, and whether hazards exist for marine navigation.

An ADCP measures water velocities by broadcasting sound beams into the water and measuring the Doppler shift of the returning acoustic signals caused by the motion of small objects (air bubbles or plankton) advected by the currents (RD Instruments, 1989). Although an ADCP can be moored, it is now common practice to mount them on the hulls of research vessels so that information on currents can be collected continuously while the ship is underway. The array of transducers is mounted to the hull such that sound beams can be simultaneously transmitted in four directions. About once each second a short burst of sound (a "ping") is transmitted from each transducer and the time, strength, and frequency shift of the return echos are recorded. Echos from shallow depths return sooner than echos from deeper ranges, so that gating the return signal into bins by time-delay provides data for an

entire depth profile from each ping. Measuring the Doppler shift in any three directions allows the geometric calculation of horizontal and vertical velocities relative to the motion of the ship. Failure to remove the relative motion of the ship the greatest source of error, but the advent of continuous GPS coverage in the 1990s has significantly reduced errors to $O(2 \text{ cm/s})$. An ADCP with 150 kHz transducers can usually measure velocities to 400-500 m depth.

This dissertation deals with the use of ADCP data to study regional circulation patterns in two biologically rich regions and explores the potential role of circulation dynamics in controlling the production and distribution of nutrients. Using ADCP data, the conventional circulation models (based on the inferred velocities from dynamic height) are tested. In Chapter II, ADCP data are used to study the currents around the Galápagos Islands where the Equatorial Undercurrent shoals and diverges. The data, collected during the IRONEX II program, are part of a larger effort to address the role of biologically rich oceanic regions in the global carbon cycle and their possible mitigating effects on global warming. In Chapter III, a method to remove tidal velocities from the absolute velocities measured by an ADCP is described. Tidal velocities in ADCP measurements are a nagging frustration to oceanographers trying to study the mean currents in a region. By fitting ADCP and current meter data to a time/spatial function using the method of least squares, an empirical tidal model is developed which can be used to reduce the unwanted tidal “noise”. The method is used to “detide” ADCP observations collected in the Gulf of the Farallones during a project to study the impact of currents on dredge spoils deposited there. In Chapter IV, the subtidal circulation of the Gulf is described for various seasons and wind conditions, and a conceptual

model to explain the relationship between the winds, the flow over the continental slope, and the water mass characteristics is presented. The body of this thesis is written as three self-contained chapters to facilitate the publication of these studies. Accordingly, the final chapter neither reports nor summarizes the results of these individual chapters. Instead, a series of recommendations for future work is made.

II. CIRCULATION IN THE ARCHIPIELAGO DE COLON (GALAPAGOS ISLANDS), NOVEMBER, 1993¹

A. INTRODUCTION

The Archipiélago de Colón (henceforth referred to as the "Archipelago"), also known as the Galápagos Islands, lays athwart the equator in the Eastern Equatorial Pacific between 89°W and 92°W, stemming and diverting the zonal flows found near the equator (Figure 2.1). From the west, the eastward flowing Equatorial Undercurrent shoals, impinging upon Isla Fernandina and Isla Isabela. From the east, the westward-flowing South Equatorial Current sweeps surface waters in and around the Archipelago. The shallow waters of the Archipelago facilitate both the vertical and horizontal mixing of these waters. Satellite data have shown a biologically rich plume adjacent to and northwest of Islas Fernandina and Isabela (Feldman, 1986). The goal of our measurement program was to measure the circulation around the Archipelago and to try to determine the source waters for this biologically rich plume.

Wyrtki and Kilonsky (1984) provide the canonical description of equatorial circulation in the Central Pacific (150°W-153°W). Features include: (1) an eastward flowing Equatorial Undercurrent (EUC) extending from 2°S to 2°N, 50 - 275 m depth, with a transport of 23 Sv and a peak velocity of about 1 ms⁻¹ occurring on the equator at a depth of 125 m; (2) the South Equatorial Current (SEC) flowing westward above and on either side of the EUC; the

¹This chapter has been accepted for publication by Deep-Sea Research.

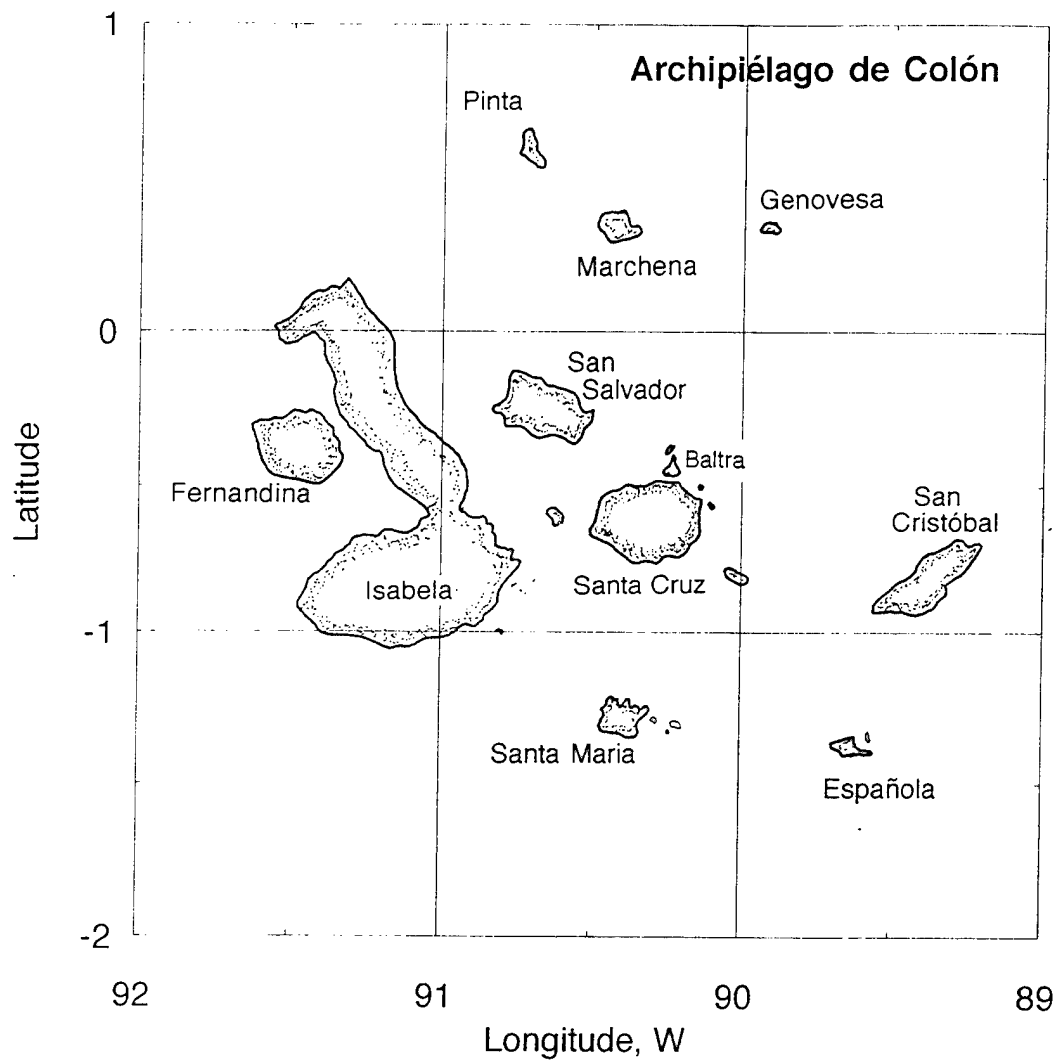


Figure 2.1 Chart of the Archipiélago de Colón. Bolivar Channel separates Isla Fernandina and Isla Isabela. Isla Darwin is located at 2°N, 91°W, north of the area depicted on this chart.

flow of the SEC is strongest at the surface with mean speeds between 0.3 and 0.4 ms^{-1} ; (3) beneath the EUC to about 1000 m , an Equatorial Intermediate Current (EIC) flowing westward intermittently with a maximum mean speed of about 0.1 ms^{-1} (Firing, 1987); (4) Subtropical Subsurface Water penetrating the EUC from the Southern Hemisphere with a salinity maximum at the equator of $S = 35.2$; and (5) isotherms diverging above and below the core of the EUC indicating upwelling and downwelling, respectively.

These features are modified somewhat near the Archipelago. Knauss (1960) first observed the shoaling of the core of the EUC to 40 m at the Archipelago. During a later cruise, Knauss (1966) tracked the flow of the EUC around the north side of Isla Isabela through a wide and deep gap in the Archipelago between Isla Isabela and Isla Darwin. At 89°W , he observed eastward subsurface flow, but at greater depth ($160\text{-}250 \text{ m}$) and reduced velocity ($0.1\text{-}0.25 \text{ ms}^{-1}$). Christensen (1971) observed the EUC flowing to the north around Isla Isabela in February 1966 and found currents to the south to be weak and irregular. In October and December 1971, Pak and Zaneveld (1973) also found that the waters in the EUC to the east of the Archipelago were derived from water flowing around the north side of the islands; they also noted that there was no clear indication of a branch of the EUC to the south of the islands. Wyrski (1967) used water mass analysis to show that some of the EUC waters recirculate both north and south of the Archipelago. Using historical hydrographic data, Lukas (1986) documented the contribution of eastward-flowing EUC waters to the flow of the Peru-Chile Undercurrent. Lukas also showed evidence of a seasonal cycle in which the EUC diminishes in the late fall (October to December) at the Archipelago.

More recent observations and modeling of the flows in this region have refined this picture. Leetmaa (1982) shows that the EUC approaches the Archipelago asymmetrically south of the equator and that, as the current decelerates, most of the transport is lost from the upper part of the current. Leetmaa and Wilson (1985) note that upwelling associated with the divergence of Ekman transport due to northward wind stress occurs south of the equator, between 1°S and 2°S along 85°W , and is confined to the upper 40-50 m. Surface flow is westward at about 0.5 ms^{-1} and, beneath the surface upwelling region, traces of eastward flow occur in and below the pycnocline. Near surface currents are northward and, to the south of the equator, flow in the pycnocline was southward.

B. MEASUREMENTS

ADCP and CTD data were collected as part of the Office of Naval Research (ONR) funded 1993 IRONEX2 experiment designed to test the hypothesis that iron might limit phytoplankton growth in the ocean. The data were collected aboard the **R/V Columbus Iselin** between 8-19 November. The strategy for the measurement program was to first collect data in the relatively unproductive waters east of the Archipelago along 89°W and then to move to the west of Islas Isabela and Fernandina and locate the plume of high productivity and characterize its horizontal and vertical structure. Sampling was limited by the constraints of available shiptime and chemical reagents.

Hydrographic data were acquired at 20 stations around the Archipelago as shown in Figure 2.2. CTD casts were made to 1500 m or to near the bottom if the water was shallower than 1500 m. Winds, sea surface temperature and sea surface salinity were also monitored continuously using shipboard systems. The processing of the CTD, wind, sea surface

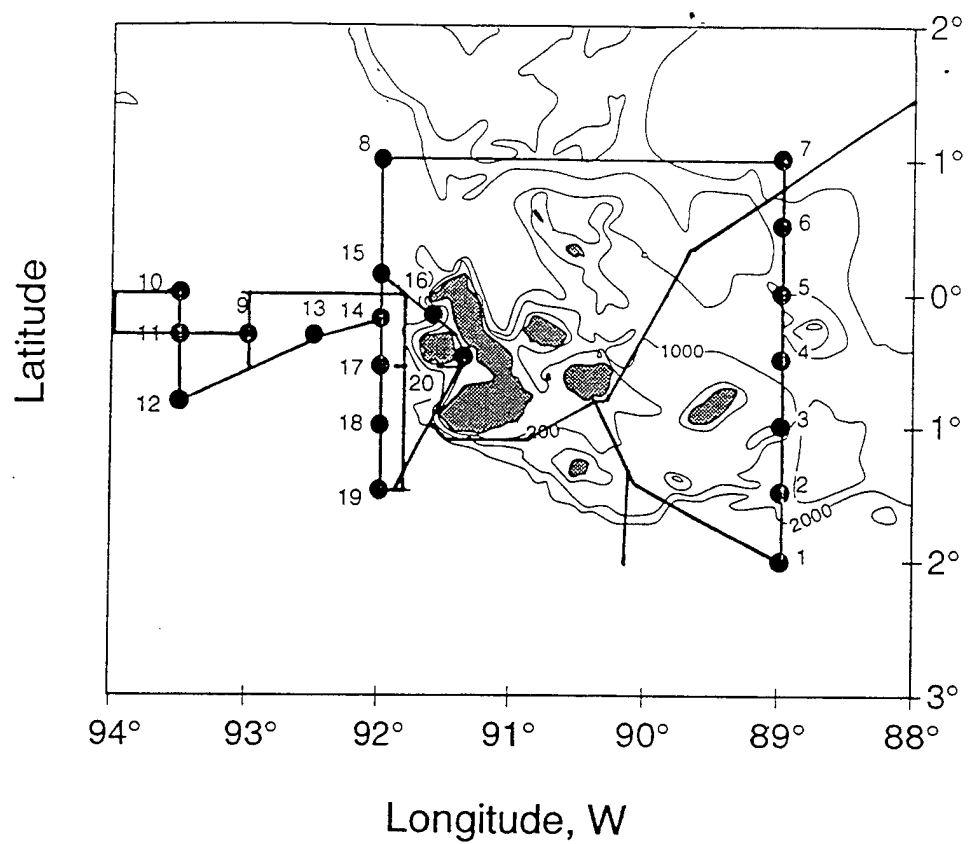


Figure 2.2 Cruise Track and location of hydrographic stations. 200 m, 1000 m, and 2000 m isobaths are shown.

temperature, and salinity data are described in Miller, et al. (1994). Miller, et al. also included descriptions of sea surface conditions.

Currents were observed continuously using a hull-mounted 150 kHz RDI ADCP. East (u) and north (v) velocity components were averaged in three-minute ensembles in 4-m thick depth bins between 9 and 405 m depth. Data were collected using TRANSECT software (R D Instruments, 1992), and were navigated using GPS data. Several periods of bottom tracking and one course reversal were used to estimate alignment and sensitivity errors following the method of Joyce (1989). Alignment error was $0.31^\circ \pm 0.23^\circ$ and sensitivity error was -0.026 ± 0.005 . The velocity bin centered on 201 m was used as a reference layer to correct for short-term errors due to GPS and gyro errors (Pollard and Read, 1989). The ADCP data were then manually edited to remove periods when the ship was hove-to (on-station) for extended periods. Finally, gridded fields of 0.01° longitude/latitude were created for each 4-m velocity bin.

Eastward or westward transports were calculated for each bin by multiplying the velocity component by the area of the bin (4423 m^2). Because the north-south sections did not always cover the entire extent of a current regime, total transports could not be estimated. Instead, transport for each current was calculated in 0.25° latitude blocks by summing the bin transports within each current.

Richardson numbers, a measure of the effect of vertically sheared flow on stability, were calculated using CTD and ADCP data. ADCP measurements within 1 km of the CTD station were averaged within each 4-m depth bin. CTD data were used to compute depth and density at 2 dbar intervals. The CTD data were then interpolated to match the depths of the

ADCP measurements. At each depth between 9 m and 301 m, the Richardson number, Ri , was calculated using the standard formula:

$$Ri = -\frac{g}{\rho} \frac{\frac{\delta \rho}{\delta z}}{\left[\left(\frac{\delta u}{\delta z}\right)^2 + \left(\frac{\delta v}{\delta z}\right)^2\right]}$$

Empirical evidence has shown that $Ri < 0.25$ indicates maintenance or increase of turbulence while larger numbers indicates suppression of turbulence (Pond and Pickard, 1983).

C. EL NIÑO CONDITIONS

Because interannual variability plays an important role in determining environmental conditions in the Archipelago, the status of El Niño affects the interpretation of data from this region. In November, 1993, an extended three-year El Niño was coming to a close and, although positive sea surface temperatures anomalies greater than 0.5°C dominated the tropics, temperatures in the Archipelago were normal, convection over the central equatorial Pacific was also near normal, and the Southern Oscillation Index was near zero (Climate Analysis Center, 1993). Winds measured during the cruise were also consistent with climatology. After removing wind observations which were collected while the **R/V Columbus Iselin** was in port, in Bolivar channel, or in the lee of islands, the vector mean wind speed for the shipboard measurements was 6 ms^{-1} , 166°T . This compares favorably with the November mean winds for the same area from the Hellerman and Rosenstein (1983) climatology of 5 ms^{-1} , 179°T .

Transient equatorial phenomena on time scales shorter than El Niño could also affect our interpretation of the hydrography and currents. Figure 2.3a shows that eastward-propagating depressions in the 20°C isotherm (associated with Kelvin waves) originating near 160°W reached the Archipelago (90°W) in May/June 1993 and again in October 1993 and January/February 1994. Hourly detided sea level at Baltra on Santa Cruz Island (Figure 2.3b) corroborates this interpretation. Sea levels were elevated April through June and again in October. However, by the period of the cruise (Figure 2.3c), sea levels were near-normal (within one standard error of a multi-year biharmonic fit), suggesting that our measurements were minimally affected by transients.

D. RESULTS

Hydrographic results are presented as vertical sections of hydrographic properties along 89°W, 92°W, and 0.25°S (Figure 2.4), ADCP (Figure 2.5), Richardson Number (Figure 2.6), as sea surface conditions (Figure 2.7), and as current vectors on horizontal surfaces (Figure 2.8). As most of the ocean variability is located in the upper 300 m, only observations to that depth are shown.

1. 89°W

The section along 89°W extended from 2°S to 1°N, passing through the easternmost waters of the Archipelago. Stations were occupied sequentially from south to north, taking almost 3 days to complete the section. Water depths exceeded 1000 m at all stations except at 1°S where our station was 60 km east of Isla San Cristóbal in water 370 m deep. Also note an unnamed subsurface bank lies just to the east of 89°W at 1.8°S where depth shoals to 200 m.

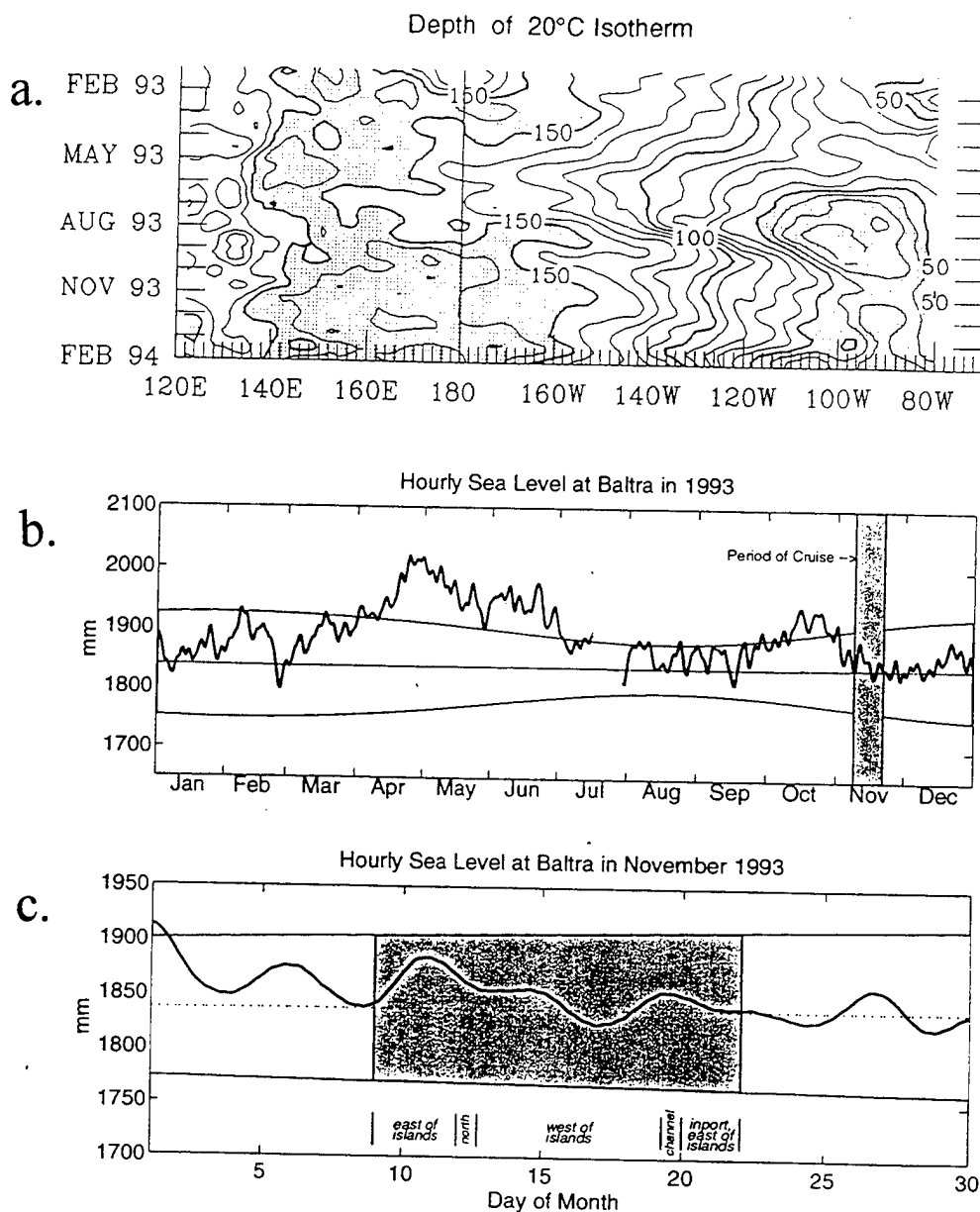


Figure 2.3 Variability along the equator in 1993. (a) Depth of the 20°C isotherm. The contour interval is 10 m with shading for values < 50 m and > 150 m (from figure T16, Climate Analysis Center, 1994). (b) Hourly sea level at Baltra (Santa Cruz Island) in 1993. The bold line indicates sea level (mm), which has been detided and then low-passed through a 73-hr cosine filter. There were data missing in July. The fine line is a biharmonic least squares fit for annual and semi-annual frequencies using hourly (detided) sea level observed at Baltra between 1985 and 1996. The lightly shaded area is within one standard error of the fit. The area of darker shading corresponds to the period of the **R/V Iselin** cruise. (c) Same as middle except for November 1993. The annotation describes the position of the **R/V Iselin** with respect to the Archipelago.

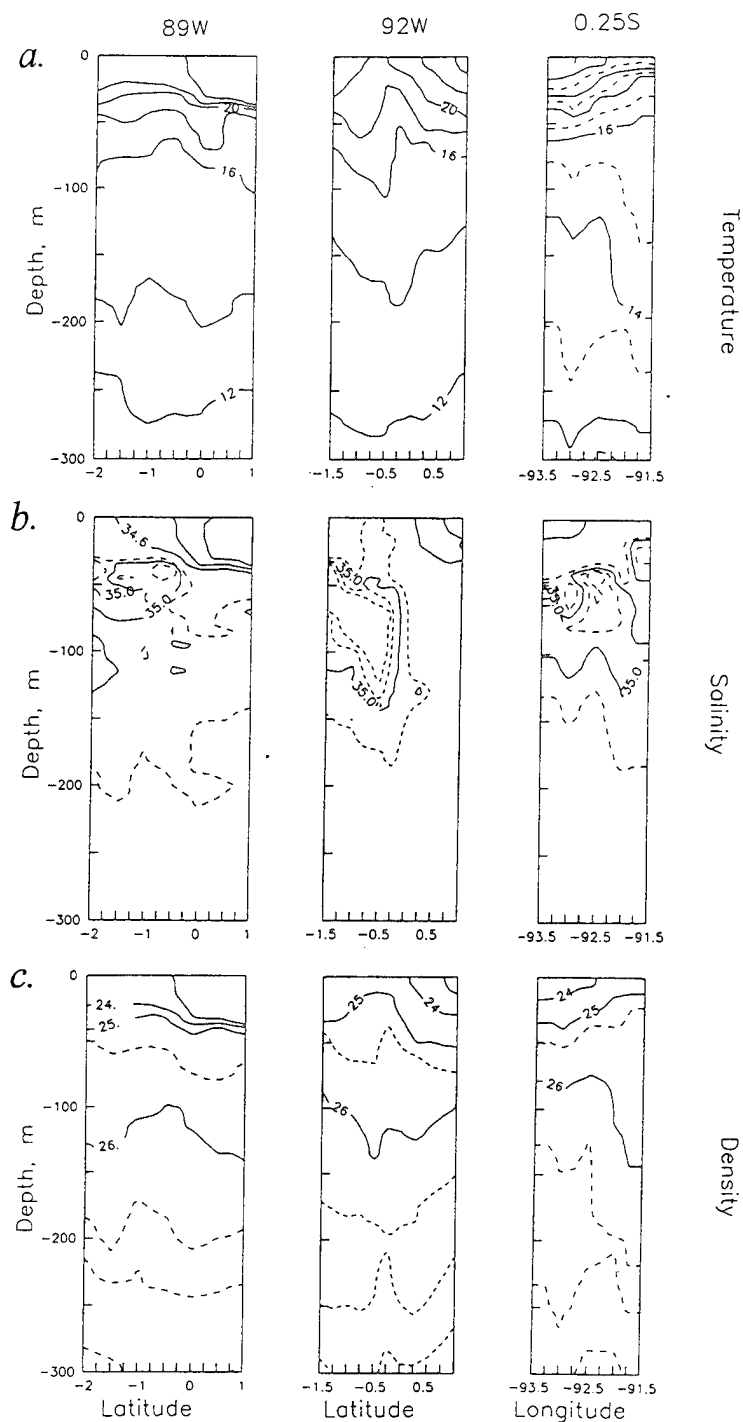


Figure 2.4 Hydrography vertical sections at 89°W, 92°W, and 0.25°S. (a) Temperature. The contour interval is 2°C for solid lines and 1°C for dashed lines. (b) Salinity. The contour interval is 0.4 S for solid lines and dashed lines indicate $S = 34.95$, 35.05 and 34.10 . (c) Density anomaly. The contour interval is 1 kg m⁻³ for solid lines and dashed lines indicate 25.5, 26.2, 26.4, and 26.6 kg m⁻³.

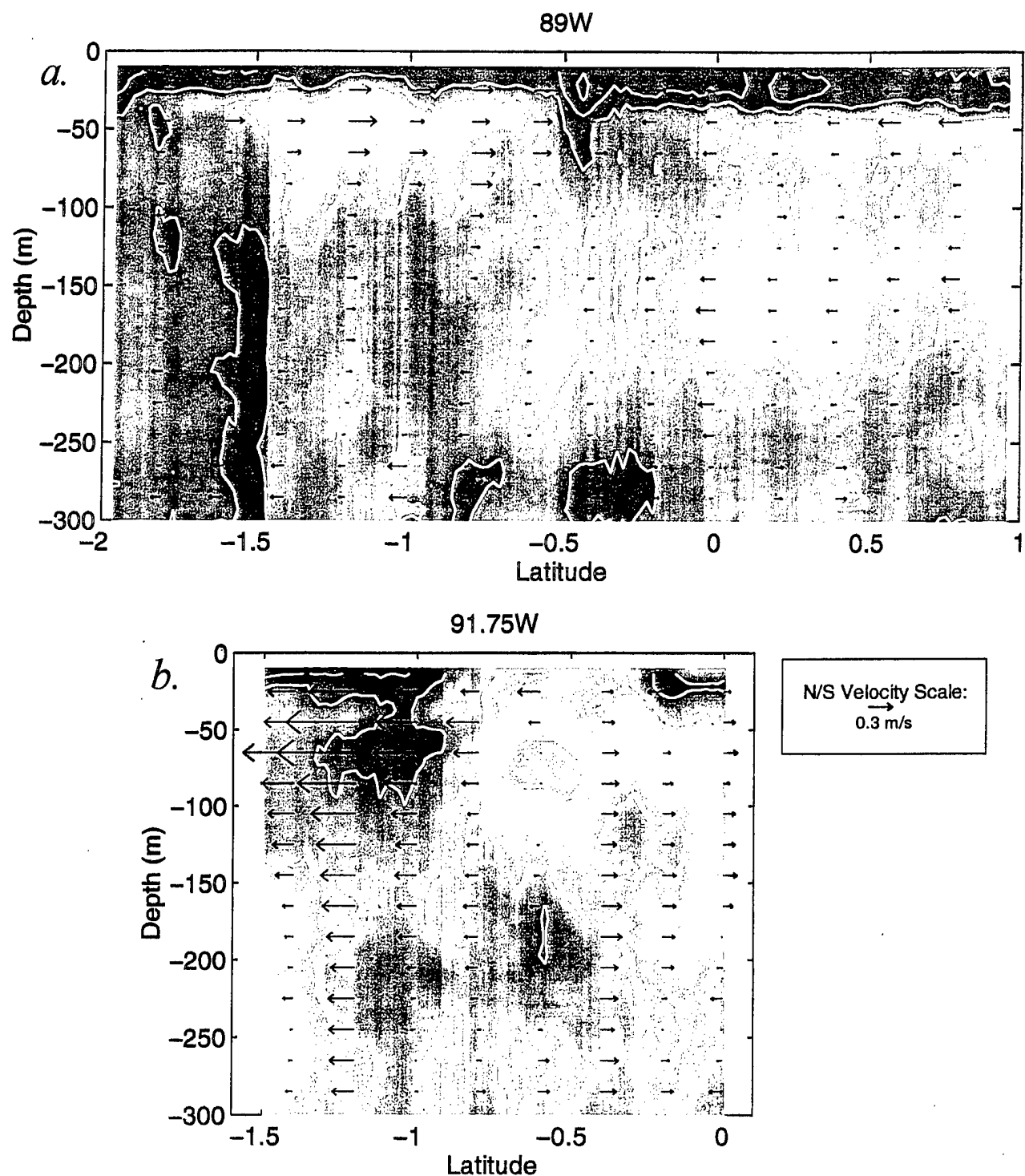


Figure 2.5 ADCP sections at (a) 89°W , (b) 91.75°W , (c) 92°W , (d) 93°W , (e) 93.5°W , (f) 94°W . Zonal velocities are contoured and meridional velocities are indicated by the black arrows. The color bar indicates the magnitude and direction (east or west) for the zonal velocity. The contour interval is 0.2 ms^{-1} . The magnitude of the meridional velocity is given by the arrow in the lower right hand corner of the figure.

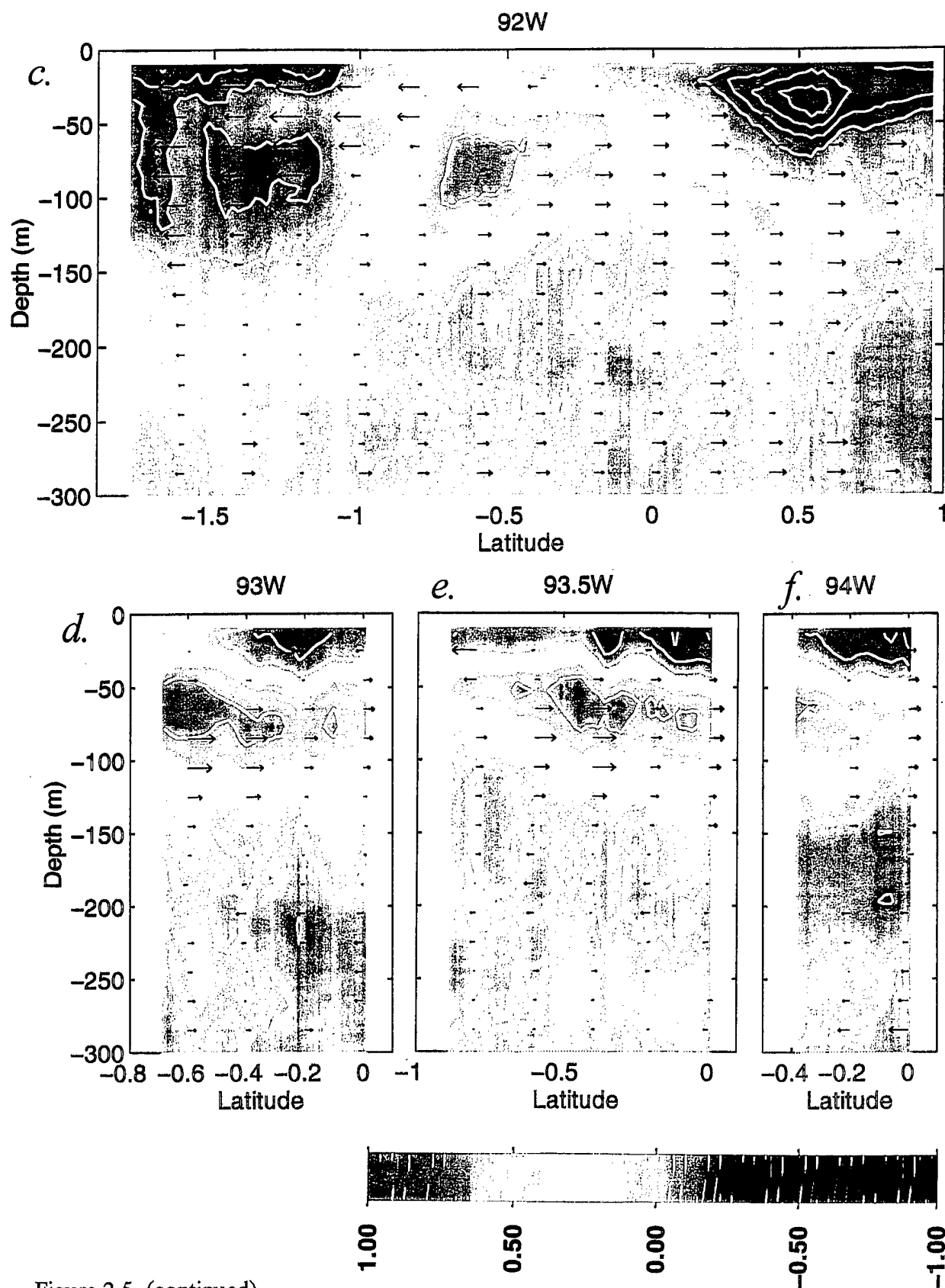


Figure 2.5 (continued)

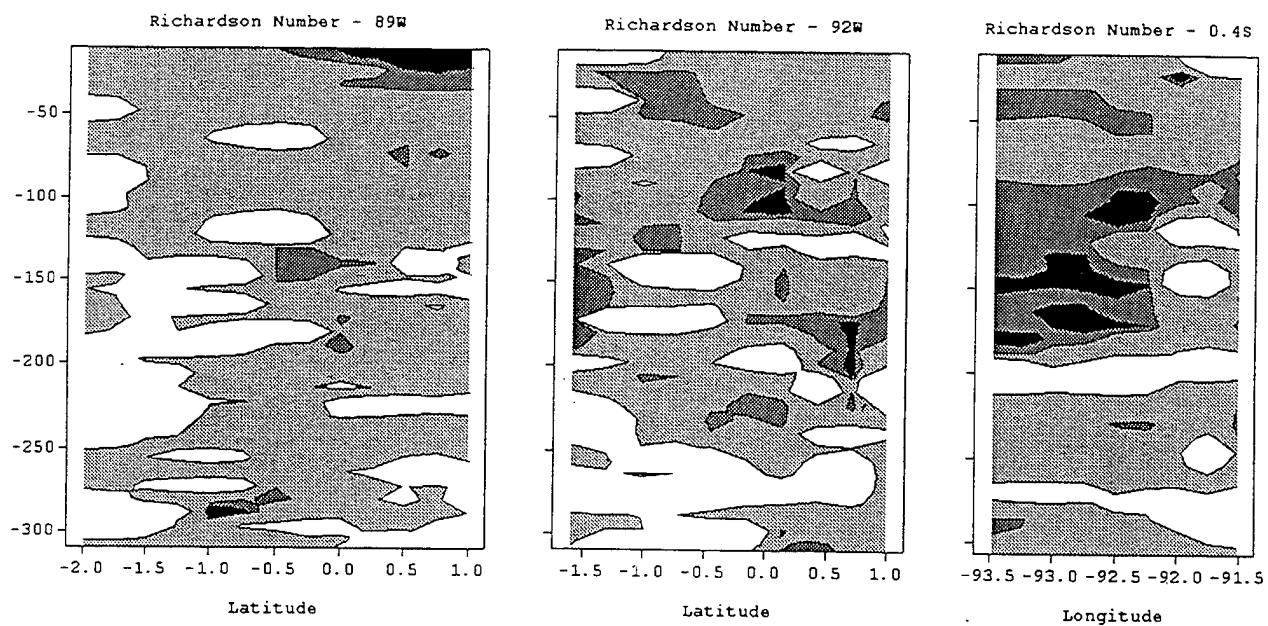


Figure 2.6 Vertical sections of Richardson number, Ri . $Ri > 10$ is white, $10 \leq Ri < 1$ is light grey, $1 \leq Ri < 0.25$ is dark grey, and $Ri \leq 0.25$ is black.

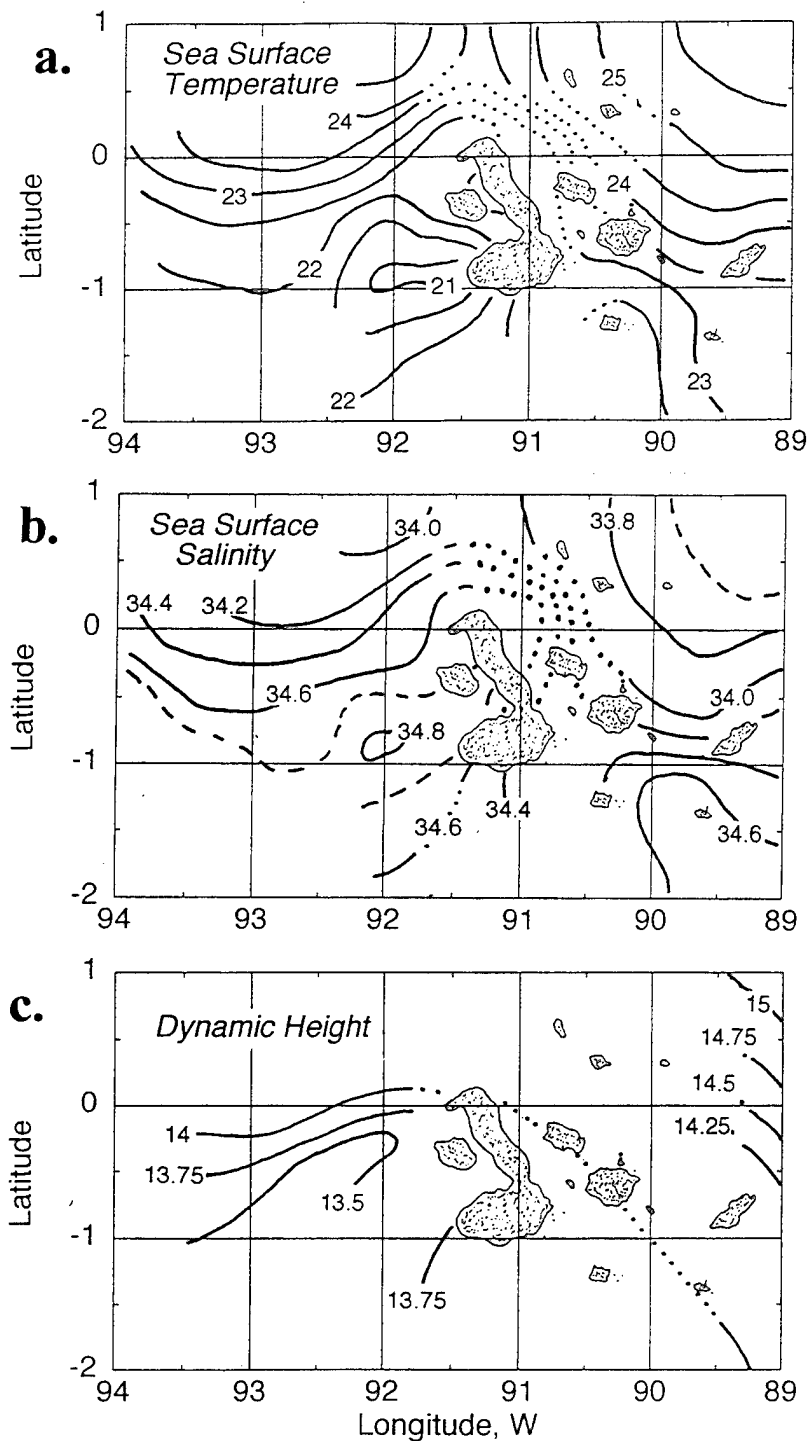


Figure 2.7 Sea surface conditions. (a) Temperature, $^{\circ}\text{C}$. Contour interval is 0.5°C . Waters in Bolivar Channel to the east of Fernandina are warmer than 22.5°C . (b) Salinity. Contour interval is $S = 0.2$ except $S = 34.7$ is shown by a dashed line to the west of Isabela and $S = 33.7$ is shown by a dashed line in the northeast corner of the chart. (c) Dynamic Height (ΔD^0_{1000}), m^2s^{-2} . Contour interval is $0.25 \text{ m}^2\text{s}^{-2}$. Dots are used to connect isopleths in regions with no observations.

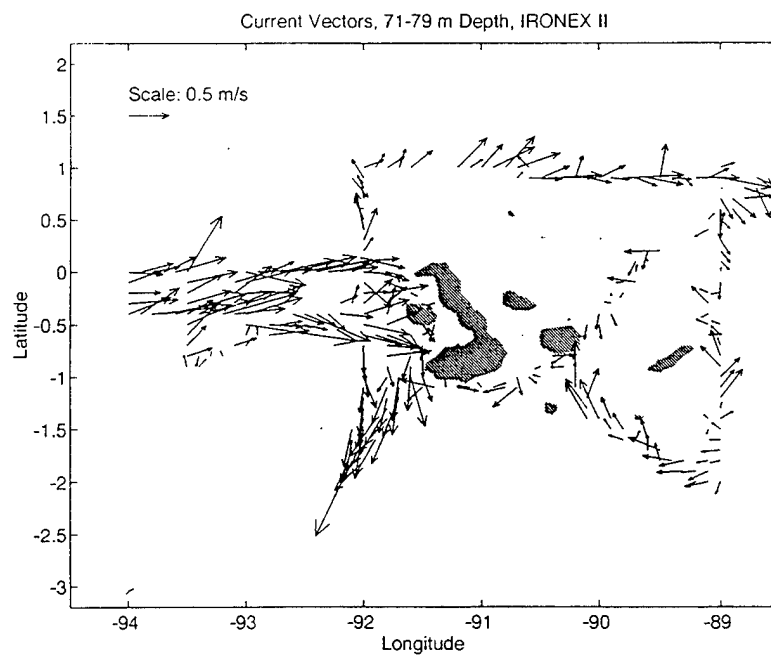
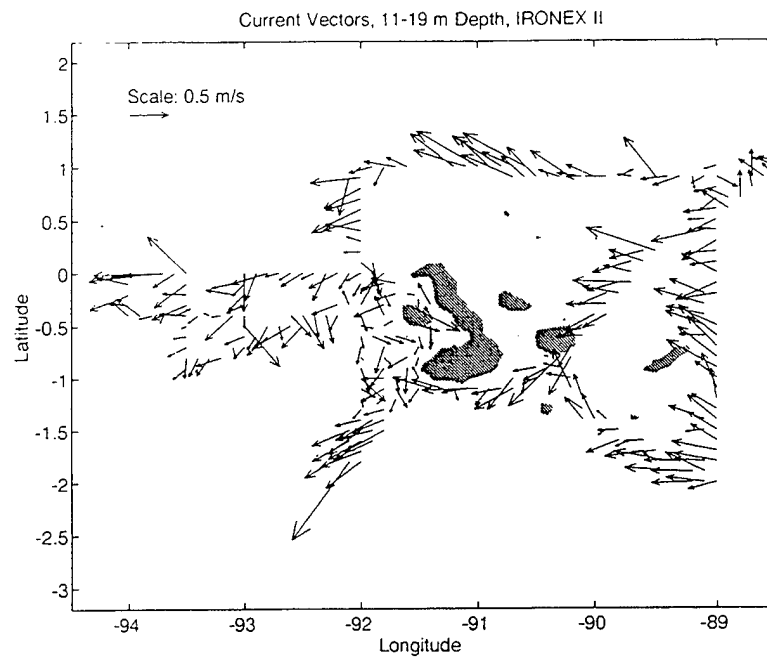


Figure 2.8 ADCP velocity vector charts at (a) 15 m, (b) 75 m. Data have been averaged into 0.1° latitude

Surface waters overlay a sharp pycnocline (Figure 2.4c, left), located at a depth of about 30 m, which deepened and intensified to the north. Surface salinity at 1°N was about 1 S fresher (Figure 2.4b, left) and temperature was 3°C warmer (Figure 2.4a, left) than those observed at 2°S , marking the southern edge of the equatorial front. The subsurface salinity maximum (Figure 2.4b, left) was greater than $S=34.95$. Between 1.5°S and 0.5°S , the maximum salinity exceeded $S=35$ and was at about 50 m, contrasting with somewhat warmer and fresher water at this depth between the equator and 0.5°N . Elsewhere, the salinity maximum was 100 m or deeper, except at 1°N where it was at a depth of 70 m.

The zonal velocity field along 89°W (Figure 2.5a) was westward everywhere in the surface layer above the pycnocline. The strongest westward flow, 0.6 ms^{-1} , occurred along the frontal zone at 0.4°S where $S = 34.2\text{--}33.8$ and $24\text{--}25^{\circ}\text{C}$ surfaced, and which also marked a convergence of the meridional velocity field (Figure 2.5a). Two shallow eastward jets were observed: a southern one associated with the shallow (50 m) salinity maximum at 1.4°S and a northern one at 1°N . The latter was also associated with the subsurface salinity maximum, but at 150 m, and was somewhat deeper and broader. Both of these eastward flows were marked by a divergence of isotherms associated with eastward flow in the EUC and had maximum speeds of $0.2\text{--}0.3\text{ ms}^{-1}$. Meridional flow below the pycnocline appeared weak (Figure 2.5a). For the subsurface eastward jet to the north of the equator, meridional flow was southward. But for the eastward jet to the south of the equator, meridional flow was northward.

Richardson numbers (Figure 2.6) were > 0.25 over most of this section. An active mixing region ($\text{Ri} < 0.25$) existed north of the equator near surface ($z < 20\text{ m}$).

Nutrients were measured sparsely in the upper ocean waters along 89°W. In surface waters, lowest nutrients were associated with the warmer, fresh waters at the north of the section: nitrates less than 2 $\mu\text{mol kg}^{-1}$, phosphate less than 0.4 $\mu\text{mol kg}^{-1}$, and silicate less than 1 $\mu\text{mol kg}^{-1}$. These increased to the south and at 2°S were 8 $\mu\text{mol kg}^{-1}$ nitrate, 0.8 $\mu\text{mol kg}^{-1}$ phosphate and 4 $\mu\text{mol kg}^{-1}$ silicate. Concentrations also increased markedly below the pycnocline.

2. 91.75°W

The core of the EUC was centered at 0.5°S (Figure 2.5b), with maximum eastward velocities of 0.4 ms^{-1} observed between 50 and 100 m depth, 0.4°S and 0.6°S. At the surface, weak eastward flow was observed over the core of the EUC. To the north and south of the EUC, the flow was westward. South of the EUC, the westward flow extended from the surface to a depth of 100 m. The meridional flow (Figure 2.5b) was weakly sheared and divergent: to the north of 0.5°S the flow was northward, and to the south of 0.5°S the flow was southward, exceeding 1 ms^{-1} at 1.2°S. This maximum southward flow was centered in the pycnocline (not shown), weakening above and below.

3. 92°W

Our sampling sequence along 92°W was not continuous. After reaching the equator, we turned west, surveying the plume area, before returning to occupy hydrographic stations at 0.25°S and 0.25°N on the section. We then occupied a station at the northern end of Bolivar Channel before returning and completing the 92°W section. The southernmost station was completed almost one week after the northernmost station was started.

Along 92°W, the zonal velocity field (Figure 2.5c) indicated a much stronger and better developed EUC than the eastward flows observed at either 91.75°W or 89°W. The core of the EUC was marked by velocities exceeding 0.6 ms^{-1} centered at 0.5°S, 80 m deep. Although the subsurface eastward flow extended northward to 1°N, it was neither as thick nor as strong as it was to the south of the equator, possibly due to temporal variability. Strong westward flow was observed in the surface layer, except in the region over the core of the EUC where flow was to the east. The westward flow was best developed to the north of the EUC where a strong jet with velocities exceeding 1 ms^{-1} was observed at 0.5°N, 35 m depth. Beneath the EUC, between 150 and 200 m, weak westward flow was observed.

To the north of the equator above 50 m, the meridional velocity field along 92°W was southward (Figure 2.5c). There was a narrow region of northward flow near the equator in this depth zone. To the south, the flow became southward again, with the zero isotach deepening to at least 300 m at 1.5°S. Therefore, with the exception of its southward boundary, most of the EUC appeared to be directed northeastward.

Richardson numbers along 92°W (Figure 2.6) were lowest along the base of the EUC between 0.5°S and 0.25°N.

Surface waters were warmest and freshest at 1°N, $S=33.8$ and 25.2°C (Figure 2.4a and 4b, center panels). A density front occurred in the upper layer in the northern hemisphere corresponding to a density change of 2 kg m^{-3} , along which strong westward flow was found (Figure 2.4c, center panel). This front marked the southern boundary of the Equatorial front (Knauss, 1966). Near-surface upwelling was centered over the EUC between 1°S and 0.5°S, which corresponded to the surface temperature minimum (19.5°C) and salinity maximum

($S=34.9$) observed along this section. The shallow pycnocline was weaker than that observed at 89°W , especially to the south of the equator. Within and just beneath this shallow pycnocline, a salinity maximum ($S=35$) extended from the south to 0.25°S , the northern boundary of the strong core of the EUC. At 0.25°S , the isotherm spreading associated with the lower portion of the EUC occurred between 16°C and 14°C , while to the north and south the 13°C thermostat dominated.

The nutrient fields all reflect the surface upwelling pattern seen in the temperature, salinity, and density fields. Subsurface, the maximum nutrient concentration at a given level seemed to shift somewhat to the north.

4. 93°W

The core of the EUC was found between 50 and 80 m at 0.5°S . It was marked by eastward velocities exceeding 0.6 ms^{-1} and a northward component of about 0.2 ms^{-1} (Figure 2.5d). In and above the pycnocline, the meridional component of flow appeared convergent at 0.4°S (Figure 2.5d), and to the north of this region lay strong westward flow.

A single CTD station was occupied in the middle of this section at 0.4°S (station 9). Salinity maxima ($S=35.05$) were at 45 m and 85 m.

5. 93.5°W

The core of the EUC deepened from 50 m at 1°S to 75 m at the equator (Figure 2.5e), with the strongest eastward flow between 0.3°S and 0.5°S . This core had a northward component. Above the EUC, flow was westward, most strongly north of 0.4°S , which corresponded to the convergence of the meridional currents (Figure 2.5e). Just to the south of 0.4°S , the meridional components diverged in association with upwelling of isopycnals and

isohalines at station 12 (not shown). The $S=35$ isohaline outlined the eastward flow of the EUC, and salinity greater than $S=35.2$ was found at the core of the EUC at 1°S .

6. 94°W

The core of the EUC is only partially resolved in this section, and appeared to lie to the south of 0.4°S at a depth of 70 m with maximum velocities exceeding 0.6 ms^{-1} (Figure 2.5f). Surface flow between the equator and 0.4°S was westward. No hydrographic data were collected along this meridian.

7. 0.25°S

A section was constructed just south of the equator (Figure 2.4, right panels). This section consists of stations at 93.5°W , 93°W , 92.5°W , 92°W , and 91.58°W . The latitude along this section varies somewhat: the first three stations were between 0.35°S and 0.4°S , while the station at 92°W was located at 0.25°S ; the easternmost station was located at 0.17°S in water 1700 m deep at the entrance to Bolivar Channel, with Isla Isabela to the north and east and Isla Fernandina to the south. About one week elapsed between the first (station 9) and last (station 16) station along this section.

Hydrographic properties indicated upwelling of isotherms, isohalines and isopycnals in the upper 70 m toward the coast of Isla Isabella. A near surface salinity maximum was observed at the coast (Figure 2.4b, right), and upper waters were stratified below the shallow mixed layer. Beneath the shallow pycnocline (Figure 2.4c, right), strong isopycnal downsloping toward the coast was observed to the east of 92.5°W in the depth interval between 70 and 200 m. The 70 m-thick 13°C thermostad observed to the west of 92.5°W , shrank to 20–40 m to the east, with corresponding increases in the thickness of the 15°C

thermostat, and to a lesser extent, 14°C. The eastward increase in thickness of these waters was also seen in the salinity and density sections.

In the upper waters, nutrients also showed a sharp gradient between 93°W and 93.5°W. Increases were toward the west, consistent with upwelling of these waters. Above 30 m, nitrates increased by 4 $\mu\text{mol kg}^{-1}$, phosphate by 0.2 $\mu\text{mol kg}^{-1}$, and silicate by 3 $\mu\text{mol kg}^{-1}$. Phosphate and nitrate showed no evidence of subsurface deepening toward the coast, although silicate did.

Richardson numbers along this section showed a region of active mixing along the base of the EUC (Figure 2.6). The depth of active mixing appeared to shoal from 150 m to 75 m at 92°W and thence remained at 75 m at 91.58°W.

E. SPATIAL VARIABILITY

Winds were northward over much of the study area with speeds of about 6 ms^{-1} except in the area of Bolivar Channel where winds northward curved around Isla Fernandina (see Miller et al., 1994, Figure 2). Surface isotherms and isohalines (Figure 2.7) were oriented in a northwest-southeast direction east of the Archipelago, with temperatures decreasing and salinities increasing toward the southwest. Surface waters warmer than 25°C and fresher than $S=33.7$ lay to the northeast of the Archipelago. To the west, isotherms and isohalines were zonal north of 0.5°S with temperature increasing and salinity decreasing to the north. Minimum surface temperatures, $< 21^\circ\text{C}$, and maximum salinities, $S > 34.8$, occurred to the west of the southern portion of Isla Isabela.

Dynamic height (ΔD^0_{1000}) had a similar pattern (Figure 2.7), with the largest value, 15.1 m^2s^{-2} , observed at the northeastern extreme of our grid, station 7. The lowest value,

$13.3 \text{ m}^2\text{s}^{-2}$, occurred just to the west of Isla Fernandina at station 14. A trough of low dynamic height, $\Delta D^0_{1000} < 13.6 \text{ m}^2\text{s}^{-2}$, extended from the west-southwest and included stations 12, 13 and 14. Dynamic heights were greater at 89°W than 92°W ($0.5 \text{ m}^2\text{s}^{-2}$ on average), and this difference was three times greater north of 0.5°S than to the south.

Current charts were constructed by binning ADCP observations into boxes 0.1° square and averaging. Current charts are shown for surface currents (15 m) and for the EUC (75 m).

1. Surface (15 m)

Surface currents (Figure 2.8a) were westward at most locations with typical speeds of 0.5 ms^{-1} . South of the Archipelago, currents were directed strongly to the west, but appeared to be deflected southward and southwestward when they reached 92°W . Surface currents east of the islands were directed to the northwest along the 1000 m isobath and through a channel between Isla Genovesa (located at 0.3°N , 89.9°W) and a subsurface bank, although currents observed along 1°N also had a northward component, possibly due to southerly winds. Surface currents west of the Archipelago were typically weaker and to the southwest. Some eastward flow was observed to the south and west of Isla Fernandina. The region of strongest flow was located southwest of Isla Isabela where currents flowed to the southwest.

2. EUC (75 m)

Flow at this depth was dominated by the EUC (Figure 2.8a). West of the Archipelago, speeds typically exceeded 0.5 ms^{-1} to the east. These eastward flows had a northward component north of 0.5°S , but to the south of this latitude they were directed

southward. Southwest of Isla Fernandina, the strong and coherent flow was somewhat more to the south than that observed at the surface. At this depth, a weaker eastward flow was observed along 1°N . Flow at this depth does not represent the core of the EUC to the east of the Archipelago because the core of the EUC lay above 75 m to the south of 0.5°S and at 150 m to the north of the equator (Figure 2.5a).

A strong meridional divergence occurred in the southwest corner of the Archipelago in both the surface currents (Figure 2.8a) and EUC (Figure 2.8b). This must be due to the zonal convergence as the EUC impacts the Galapagos.

F. TIDAL VARIABILITY IN BOLIVAR CHANNEL

Upper ocean waters within the Archipelago tend to be better mixed than those in the open ocean due to their interaction with topography. A variety of processes, including tides and island wakes, contribute to this mixing. Feldman (1986) suggests that the large area of high productivity that is occasionally seen to the west of the Archipelago occurs during periods when mixing processes within the Archipelago supply nutrients to the larger plume via enhanced westward transport by the SEC.

To get an estimate of the degree of mixing associated with tidal currents, ADCP data collected at a single station in water 1.7 km deep at the entrance to Bolivar Channel (station 16, Figure 2.2) were examined. This station was located in an area of maximum surface productivity in October 1983 (Figure 1a, Martin et al., 1994). These ADCP data were processed as described above, then averaged every six minutes.

The tidal regime in the Archipelago is "semidiurnal," and the amplitude of the semidiurnal principal lunar (M_2) tide is 65 cm at Santa Cruz Island. The M_2 amphidrome is

located about 1000 km west of the Archipelago, with a cotidal line extending eastward to the coast of South America through the islands (Schwiderski, 1983). The M_2 tide moves clockwise about this amphidrome, with amplitude increasing into the Gulf of Panama.

The flow at station 16 had a semidiurnal character (Figure 2.9). Flows were strongest, 0.3 ms^{-1} , at 0445 and 1645; the former was clearly resolved as a subsurface maximum at 125 m while the latter appeared at the surface and was increasing at the end of the record. The stratification was similar at each of the two CTD casts made at this location, with a maximum gradient of 0.25 kg m^{-4} at a depth of 10 m. Velocity data obtained during passage through Bolivar Channel and at Station 20 were similar to the flow patterns seen at station 16. The stratification at Station 20 was also similar to that at station 16, 0.25 kg m^{-4} at depths of 10- 20 m.

Simpson and Hunter (1974) show that the water column becomes homogeneous when the ratio of the bottom depth (in meters) to the cube of the amplitude of the tidal flow (in meters per second) is near a critical value of 55 (s^3m^{-2}). Using this relationship, the tidal currents we observed in and near the Bolivar Channel would effectively mix the entire water column only where the water is a few meters deep. This suggests that tidal mixing of the sort that may bring nutrients to the surface is constrained to the nearshore of the Archipelago.

G. DISCUSSION

The surface circulation was dominated by westward flow associated with the SEC. To the east and north of the Archipelago, this westward flow had a northward component that appeared to be strongest along the edge of the equatorial front (which marked the boundary of waters of $\gamma < 23 \text{ kg m}^{-3}$, temperature $> 24^\circ\text{C}$, and salinity $S < 34.4$ which lay to

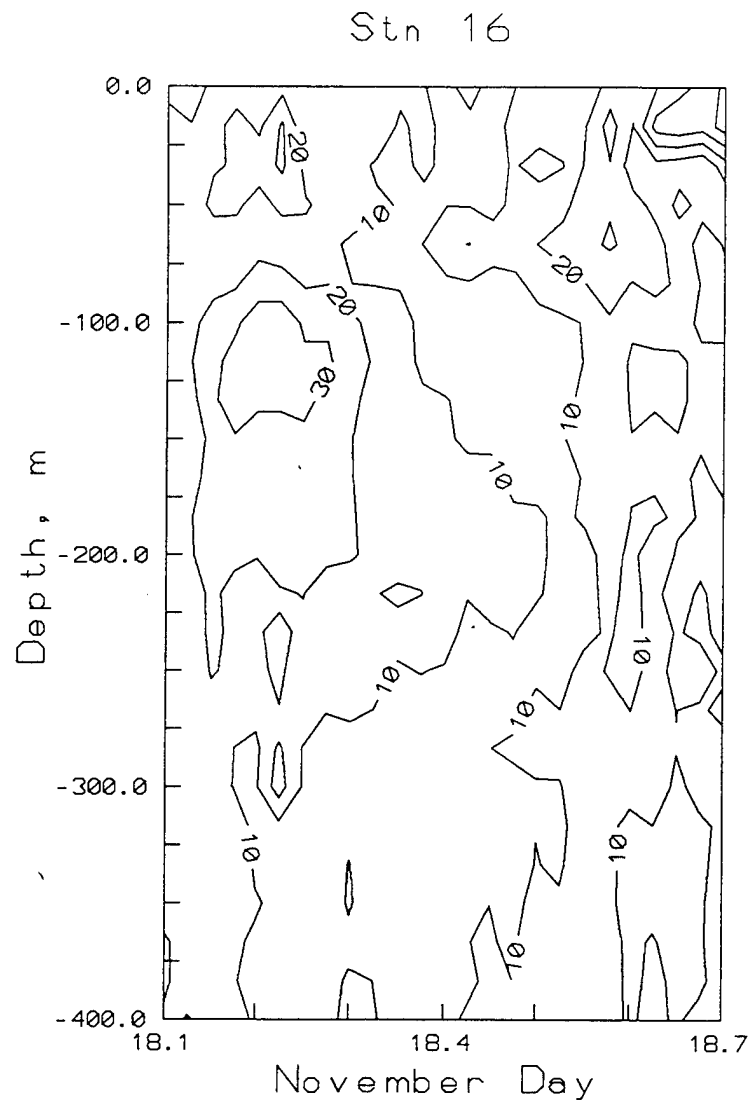


Figure 2.9 ADCP speed at the northern entrance to Bolivar Channel (Station 16, Figure 2.2). The contour interval is 0.1 ms^{-1} .

the northeast). The surface flow was westward south of the Archipelago. West of the Archipelago, the westward flow had a southward component. Eastward flow associated with the surfacing of the EUC can be seen in the region immediately to the west of Isla Fernandina. Finally, to the southwest of Isla Isabela, the surface flow is directed to the southwest with speeds $\sim 1 \text{ ms}^{-1}$.

Although historical hydrographic data suggest that the Undercurrent is not present immediately to the west of the Galapagos in November (Lukas, 1986), we observed a region of strong, well-developed eastward flow. Highest velocities in the EUC were observed at 70 m, and the core appeared to be centered at 0.5°S in the sections to the west of the Archipelago. This eastward transport was centered just below the 16°C isotherm and its southern half was marked by salinity $S > 35$. Immediately to the west of the Archipelago, the EUC transport south of 0.5°S becomes southward. The southward flow at the southern boundary of the Archipelago intensified and deflected to the southwest. The eastward transport of the EUC was 6.6 Sv at 92°W , but decreased to only 2 Sv at 91.75°W . At 89°W , the character of eastward flow changed dramatically, and two weak cores were observed: at 50 m, between 1.5°S and 1°S and at 150 m between the equator and 1°N . The transport of the former was 0.7 Sv while the latter was 2 Sv, with probably more eastward flow to the north of our section (on November 21 while returning to the Canal Zone, we observed this branch of the EUC to be located between 0.36°N , 89.5°W and 1°N , 88.7°W at 100 m depth and transport of 0.8 Sv). The southern core of eastward flow was connected with the EUC west of the Archipelago but at depths intermediate between those depicted in Figures 2.5(a) and 5(b); the salinity and temperature of these waters was similar to that of

the EUC. It is also interesting that at 89°W the eastward flow in the southern hemisphere had a northward component while in the northern hemisphere it had a southward component, indicating the possibility that the two eastward flows join further to the east.

The blocking of eastward transport of 16°C water by the Archipelago builds a deep thermostad of these waters at 91.5°W . The 13°C thermostad appeared to be of normal thickness (75 m) and depth (200 m) (see Lukas, 1986, Figure 6) at 93°W , but was greatly reduced in thickness at 91.5°W where the 16°C thermostad was increased. Above 70 m, temperature, salinity, and density gradients are sloped sharply toward the surface as the Archipelago is approached along 0.25°S . Along 92°W , this upwelling appeared to occur to the north of 0.7°S at the surface, and the upwelling zone shifted north to 0.25°S at 75-100 m depth.

Despite this upwelling, the temperature of the upper ocean appeared to be unseasonally warm on the equator at 92°W compared with historical hydrographic data (Lukas, 1986) even though El Niño conditions appeared near normal (Climate Analysis Center, 1993). At 50 m, observed temperatures were 17.3°C and salinity was 34.94 vice 14.3°C and 34.96 for historical data (Lukas, 1986, Figure 12).

As noted in the introduction, the westward flow beneath the EUC is called the EIC. This flow was best resolved by our sections at 91.75°W and 92°W . At both meridians, the EIC appeared centered at a depth of 200 m at 0.5°S with a speed of $0.1 - 0.2 \text{ ms}^{-1}$. Corresponding transports were 0.3 and 0.4 Sv. At 93°W , the EIC was somewhat deeper, 220 m, and displaced northward to 0.3°S . At 93.5°W , the eastward flow associated with the EIC was disorganized while at 94°W it appeared between 150 and 250 m across the short section. Along 89°W , flow was westward beneath both the southern and northern EUC.

The deceleration of the eastward flow in the EUC took place within 30 km of the coast of Isla Fernandina. Flow at 92°W was qualitatively similar to that observed along meridians at 93°W, 93.5°W, and 94°W but at 91.75°W the eastward transport was less than a third of that observed at 92°W. The westward pressure gradients (calculated with respect to 1500 db) west of station 14 reversed between stations 14 and 16. This eastward pressure gradient was zero at 750 m, and increased linearly with decreasing pressure to a maximum of 10^{-6} ms^{-2} at a depth of 50 m. For these two stations, we evaluated three terms of the zonal momentum balance: the zonal advection of zonal momentum, $\bar{u}(\delta u/\delta z)$; the vertical advection of eastward momentum, $\bar{w}(\delta u/\delta z)$ (\bar{w} was estimated as the product of u and the isopycnal slopes between the stations); and the zonal pressure gradient, $(1/\rho)(\delta \bar{p}/\delta x)$. The momentum advection terms fail to balance the pressure gradient by a factor of five, but errors in the estimate of the advection terms (due to the fact that the measurements were not made at the same time) were of the same order of magnitude as the zonal pressure gradient. Therefore, it is not possible to make any conclusions regarding the importance of turbulent fluxes and local acceleration in this regime.

As pointed out by Hayes (1985), the sea level difference across the Archipelago should increase as the strength of the EUC increases. Using sea level differences between Isla Isabela and Isla San Cristobal and current measurements from the equator, 95°W, he showed $u|u| \approx \Delta p/\rho$. If we use the maximum isotach from Figure 2.5c at 0.5°S, (0.6 ms^{-1}), then $u|u|$ is $0.36 \text{ m}^2\text{s}^{-2}$ and the mean difference of dynamic height between 89°W and 92°W across this latitude zone was $0.42 \text{ m}^2\text{s}^{-2}$. This agrees well with Hayes' result.

The strong southward flow just southwest of the Archipelago has not been previously reported. We have looked at sea level variability, and see no evidence of Kelvin wave activity or rapid change in sea level during the period of our observations (Figure 2.3). Lukas (1986, Figure 14) reported an oxygen maximum at 100 m (associated with Undercurrent waters) extending from the equator toward the south in this region. This pattern is consistent with the velocity field that we observed.

We also saw clear differences in the EUC to the north and the south of the Archipelago. Although the velocities were reduced to $\sim 0.2 \text{ ms}^{-1}$ to the south, the EUC was shallow (above 50 m), while to the north it was at a depth of 150 m. (The latter feature was also clearly documented by Knauss, 1966). This might be caused by the horizontal divergence (convergence) to the south (north) of the Archipelago.

Finally, we address the question of the source of the biologically rich plume. It is clear that the near-surface waters which lay to the west of the Archipelago during November 1993 were largely derived from the EUC, and as a consequence were cooler and saltier with higher concentrations of nutrients and iron than waters found to the east of the Archipelago. The areal extent of the plume shown by Feldman (1986) and observed during our cruise was too great to be sustained by tidal mixing processes given the observed speeds of surface currents and the rate of consumption of nutrients and iron by phytoplankton. We predict that this will be confirmed by SeaWIFS observations, i.e. that when there is no EUC in the region of the Archipelago, the biological activity will be absent.

III. AN EMPIRICAL MODEL OF THE TIDAL CURRENTS IN THE GULF OF THE FARALLONES

A. INTRODUCTION

This chapter describes a model of the tidal currents in the Gulf of the Farallones that uses observations of ocean currents from moored current meters and ship-mounted acoustic Doppler current profilers (ADCPs) to predict tidal velocities that can be effectively subtracted from the raw ADCP data to reduce variance at tidal frequencies. The purpose of "detiding" the ADCP data is to study the subtidal seasonal circulation of the continental shelf and upper continental slope of the Gulf, a relatively little studied region of the central California coast, where initial analysis of ADCP data from five cruises in 1991-92 suggested that tidal velocities would complicate study of the lower frequency current signal (Ramp et al., 1995). However, in addition to detiding ADCP data, the model may be useful for other applications, such as evaluating the effect of tides on pollution transport, local fisheries, and marine navigation.

If measurements of currents in a region are available, empirical tidal models are quickly implemented since they require no prior knowledge of the currents or their physics. Unlike theoretical tidal models, complicated bathymetries or coastlines are not a problem and there is no need to predetermine boundary conditions. This portability of the empirical method is attractive in situations where the tides need to be rapidly modeled such as search and rescue, military operations, or environmental disasters.

Unlike velocity data from moored current meters, the tidal signal cannot be removed from ship-mounted ADCP data by low-pass filtering or simple harmonic analysis such as the methods of Foreman (1978). This is because, in most cases, the amplitude and phase of the tidal currents vary with position and depth as well as time and the tides are confounded with the varying non-tidal mesoscale circulations. These methods cannot distinguish between temporal and spatial variability and, in general, assume the variance in a current record is due to tidal variance.

There are several methods for removing tidal velocities from ship-mounted ADCP measurements. A high-resolution numerical tidal model was used by Foreman and Freeland (1991) to detide ADCP data off Vancouver Island. However, a predictive tidal model would be relatively difficult to develop and apply to the Farallones region because of the probable nonlinear structure of the tidal flow. Dowd and Thompson (1996) estimated tidal velocities by creating a simple barotropic tidal model of the Scotian Shelf and solving for the boundary conditions by fitting the model to ADCP observations, but it is uncertain whether this method would capture the complexity of the tidal circulation in the Farallones. Tidal constituents can be estimated directly from ADCP data if the ship is stationary through at least one diurnal tidal cycle, repeatedly sails over the same tracks until a pseudo-stationary time series can be constructed (Geyer and Signell, 1990), or repeats its tracks four times in a diurnal period and the “diurnally averaged flow” is calculated (Kato et al., 1996). However, this may be an inefficient use of shiptime. Another method would be to calculate the tidal constituent values at several concurrently deployed or historical current meter mooring sites and interpolate the tidal values throughout the region. This simplistic approach was used in the Gulf of the

Farallones by Gezgin (1991), but probably does not adequately model the tidal fields given the spatial and temporal variability implied by the historical current meter records deployed in the Gulf. A final method of removing tidal data is to create a spatially dependent empirical tidal model using the ADCP data and all available current meter data. This method, first used by Candela et al. (1990, 1992) to remove tides from ADCP data collected in the Yellow Sea, extends the stationary time-series techniques of Foreman (1978) to solve for tides by fitting observations of currents to spatially dependant functions of tidal frequency and solving using the method of least squares. The Candela method was later applied by Allen (1995) to the Iceland-Faeroes Front.

The Candela method is used here to detide the Gulf of the Farallones data set. The technique has been extended to include a vastly larger data set (over 700,000 current meter and ADCP observations compared to Candela et al.'s (1990, 1992) use of 129 ADCP observations) and to include depth as a variable in the tidal model to incorporate the effects of baroclinic tides. These extensions are necessary because an inherent characteristic of the method is that in fitting the data to the specified tidal frequencies using least squares the strongest signals in the data are emphasized. Since the mean flow in the Gulf of the Farallones is much stronger than the tidal currents, relatively few observations are necessary in the Gulf to resolve the mean currents, but a large number of observations is required to discriminate the tidal fields from the mean.

An advantage of having a large data set is that as longer time series are used to create the model, the Rayleigh criterion (Godin, 1972) is met for more closely spaced tidal frequencies. For instance, Foreman and Freeland (1991) applied the Candela method to only

three days of data and could only determine a "lump M_2 and K_1 ," i.e., a single semi-diurnal and a single diurnal frequency that included all the energy in those bands. Although additional semi-diurnal and diurnal frequencies could be estimated by inference using standard ratios or ratios determined from local sea level stations, a more accurate method is to use longer periods of observations if available. This is particularly important in areas such as the Gulf of the Farallones where local sea level ratios may not reflect local tidal current ratios. We have used our model to examine the M_2 (12.4 hr), S_2 (12.0 hr), K_1 (23.9 hr), and O_1 (25.8 hr) tidal constituents that sea level data show account for most of the tidal variability in the Gulf (Noble and Gelfenbaum, 1990).

In section B, the unique bathymetric and topographic characteristics of the Gulf are described and the historical tidal observations there are reviewed. In section C, the ADCP and current meter data used in the model are detailed. In section D, the Candela model and its extensions are explained. In section E, several tidal models for the Gulf applying the empirical method to observational data sets of varying sizes and sources are described. In section F, the limitations of the method and a means of determining the associated errors are discussed.

B. THE GULF OF THE FARALLONES

The Gulf of the Farallones (Figure 3.1) generally refers to the continental shelf area (<200 m depth) off San Francisco between Pt. Reyes (38.0°N) and Pt. Montara (37.5°N). The area of this study is somewhat larger, extending south to Pt. Año Nuevo (37.1°N) and offshore to the 2000 m isobath. The coastline and bathymetry are generally oriented in a northwest/southeast direction. San Francisco Bay lies inside of the narrow entrance of the

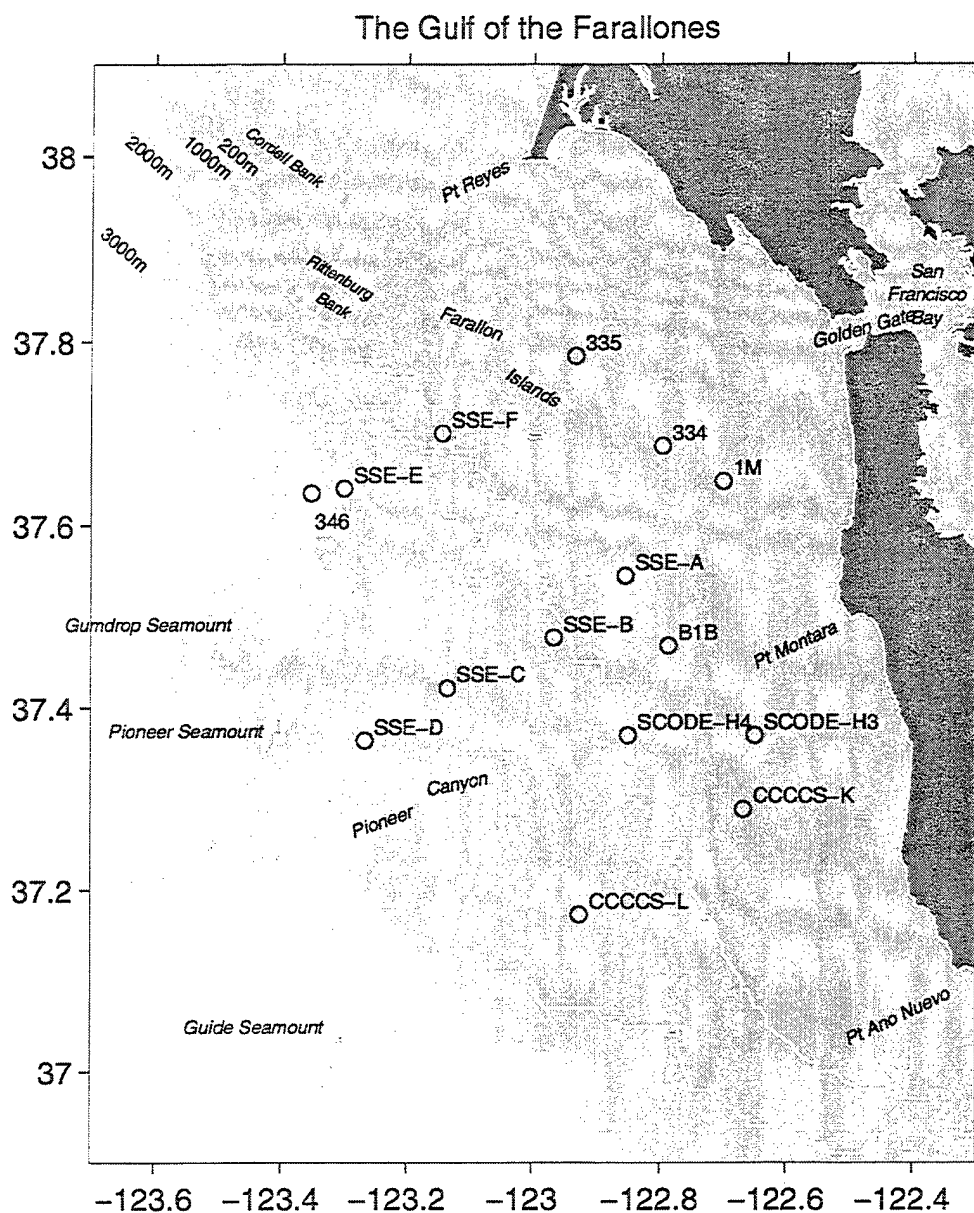


Figure 3.1 The Gulf of the Farallones. The study area extends from Point Reyes to Point Año Nuevo and seaward from the coast to about the 2000 m isobath. Bathymetry zones 0-200 m, -1000 m, -2000 m, -3000 m, and >3000 m have gradually decreasing shading. Locations of current meter moorings used in the model are indicated by large open circles.

Golden Gate. Hook-shaped Pt. Reyes is one of the most prominent points along the coast of California, extending seaward about 15 km and somewhat sheltering the inshore portion of the Gulf of the Farallones from the frequent northwesterly winds.

The bathymetry of the region is complex. The continental shelf of California is generally very narrow (in many places 6-8 km), but off the Golden Gate it widens to almost 50 km. Near the shelf break between 37.7°N and Pt. Reyes lie the Farallon Islands and Rittenburg and Cordell Banks. The continental slope varies in steepness, from 1:7 between 37.7°N and 38.0°N to 1:35 at 37.25°N. The continental slope is broken by several small, narrow canyons in the north and by the relatively large Pioneer Canyon near 37.3°N. A chain of seamounts lies offshore of the 1800 m isobath. Pioneer Seamount, rising to 950 m at 37.35°N, is the most prominent.

Coastal sea level and current meter analyses have shown that the tides off the west coast of North America are predominantly semi-diurnal. Large-scale numerical tidal models (Hendershott, 1973) indicate that the semi-diurnal tides are primarily composed of a barotropic Kelvin wave moving counterclockwise around an amphidrome located in the NE Pacific. Recent tidal models incorporating satellite altimeter data (Cartwright and Ray, 1991; Egbert et al., 1994) and observations from current meters and bottom pressure meters (Rosenfeld and Beardsley, 1987; Mofjeld et al., 1995) support this view. The pattern of the diurnal tides is similar, with a south-to-north progression up the coast (Mofjeld et al., 1995), possibly coupled with baroclinic continental shelf waves (Noble et al., 1987). In the vicinity of the Gulf, the complicated bathymetry probably causes substantial spatial variation in the tides and may possibly induce other complex internal motions (Petruncio, 1996). This spatial

complexity has been found in the Gulf in moored current meter studies (Noble and Gelfenbaum, 1990; Kinoshita et al., 1992). The complicated and seasonally variable density structure of the water (Chapter IV) may add a baroclinic component to the tides. In addition, there is a strong tidal jet into the Gulf through the Golden Gate (Largier, 1996; Petzrick et al., 1996). The tidal jet is dominated by the M_2 constituent whose amplitude is more than 1 m/s. Although the jet is strongest within the tidal excursion distance from the Gate (approximately 9 km as evident from the boundary of an ebb tidal delta), it will be shown that the influence of the jet extends seaward as far as 50 km (section E). Fluctuations in the temperature and salinity fields associated with this jet can further complicate the density patterns and perhaps increase the complexity of the tidal structure. Tidal ellipses for the M_2 , S_2 , K_1 , and O_1 constituents calculated from all available current meter moorings in the Gulf are shown in Figure 3.2. The offshore tides generally show an alongshore orientation consistent with the notion of alongshore propagating waves. The strongest tides are seen near the Golden Gate, and especially strong M_2 tides are found there. The M_2 tide is influenced by the Golden Gate tidal jet many kilometers seaward. The K_1 tide is apparently amplified over the shelf, as previously noted by Noble and Gelfenbaum (1990). At each tidal frequency, there appears to be considerable variance in the orientation, magnitude, and phases at the different current meters and moorings, even over depth on a single mooring. However, there is no obvious systematic pattern on the moorings to imply a strongly baroclinic tidal structure.

Tidal Ellipses Computed from Current Meters Near 75 m

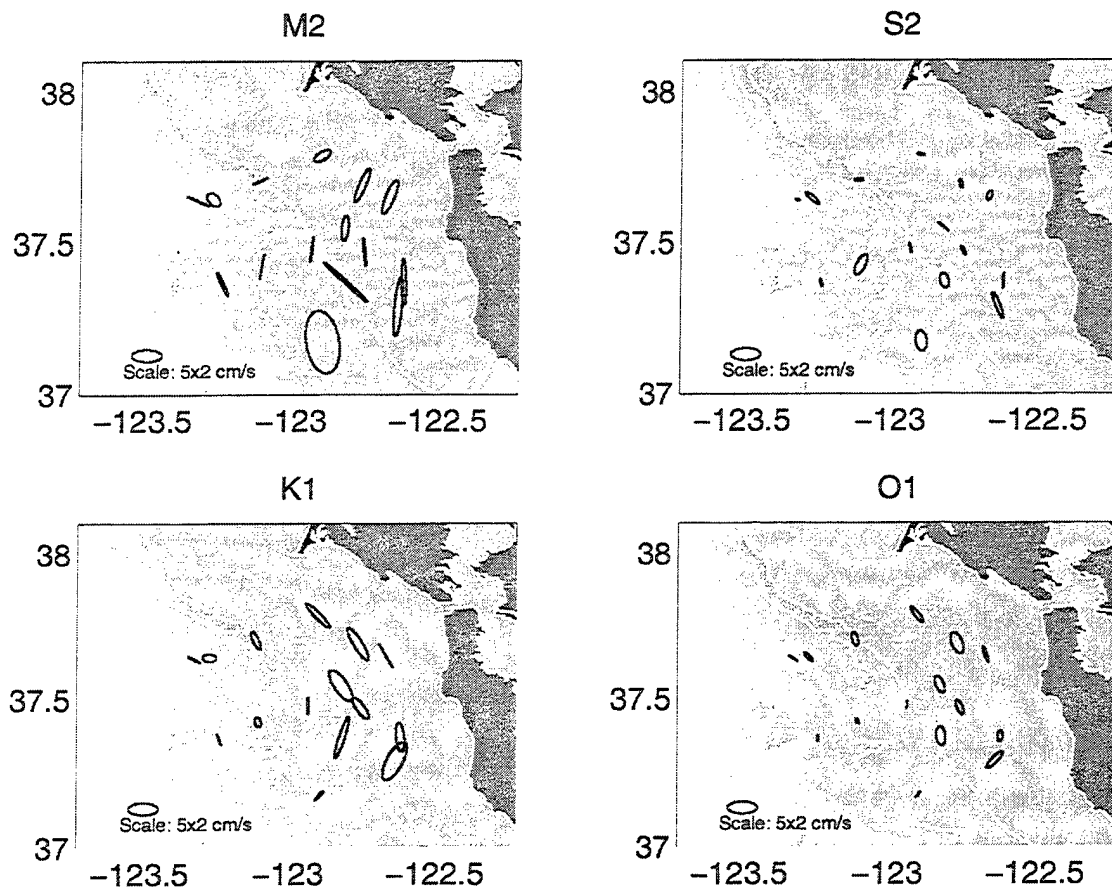


Figure 3.2 M_2 , S_2 , K_1 , and O_1 tidal ellipses calculated for the current meter on each mooring deployed in the Gulf of the Farallones since 1981 nearest 75 m depth. Values of the ellipse parameters for each meter are listed in Tables A2-A5.

C. DATA

ADCP vessel and moored current meter data were combined to form the database for the tidal model. Twenty-seven moorings with 69 instruments deployed in the Gulf of the Farallones since 1975 have been identified (Appendix A). Of these, hourly averaged measurements from 15 moorings, shown in Figure 3.1, with a total of 42 meters were used in this analysis. The observations were well distributed in time and space (Figure 3.3). Data from instruments deployed at depths greater than 500 m were not used in this study, since 350-400 m is the general limit of the ADCP. Instruments located very close to shore are presumably affected by dynamics not of interest to the general tidal circulation in the main part of the Gulf, so were excluded as well. Current meter moorings provide dense coverage at single locations (cf. Figures 3.1 and 3). The earliest moored observations are from 1981 (the SuperCODE experiment).

ADCP vessel data began in 1991. These data provide good spatial coverage within the region of the model (37.2°N - 37.8°N and 123.3°W - 122.7°W). Seven cruises with 150 kHz ADCP units provided the spatial data within the geographic boundaries of the Gulf. In general, ADCP ensembles were averaged over 15 minutes. Velocity measurements were collected in 4 or 8 m depth bins.

ADCP data were collected by the Tiburon Laboratory of the National Marine Fisheries Service aboard the NOAA Ship David Starr Jordan during springtime surveys of juvenile rockfish in 1993, 1994, and 1995. The surveys and processing of the ADCP data are described in Parker (1996). Each May-June, the survey would run three consecutive south-to-north series of east-west transects from Point Pinos to Bodega Bay, each taking 7-10 days.

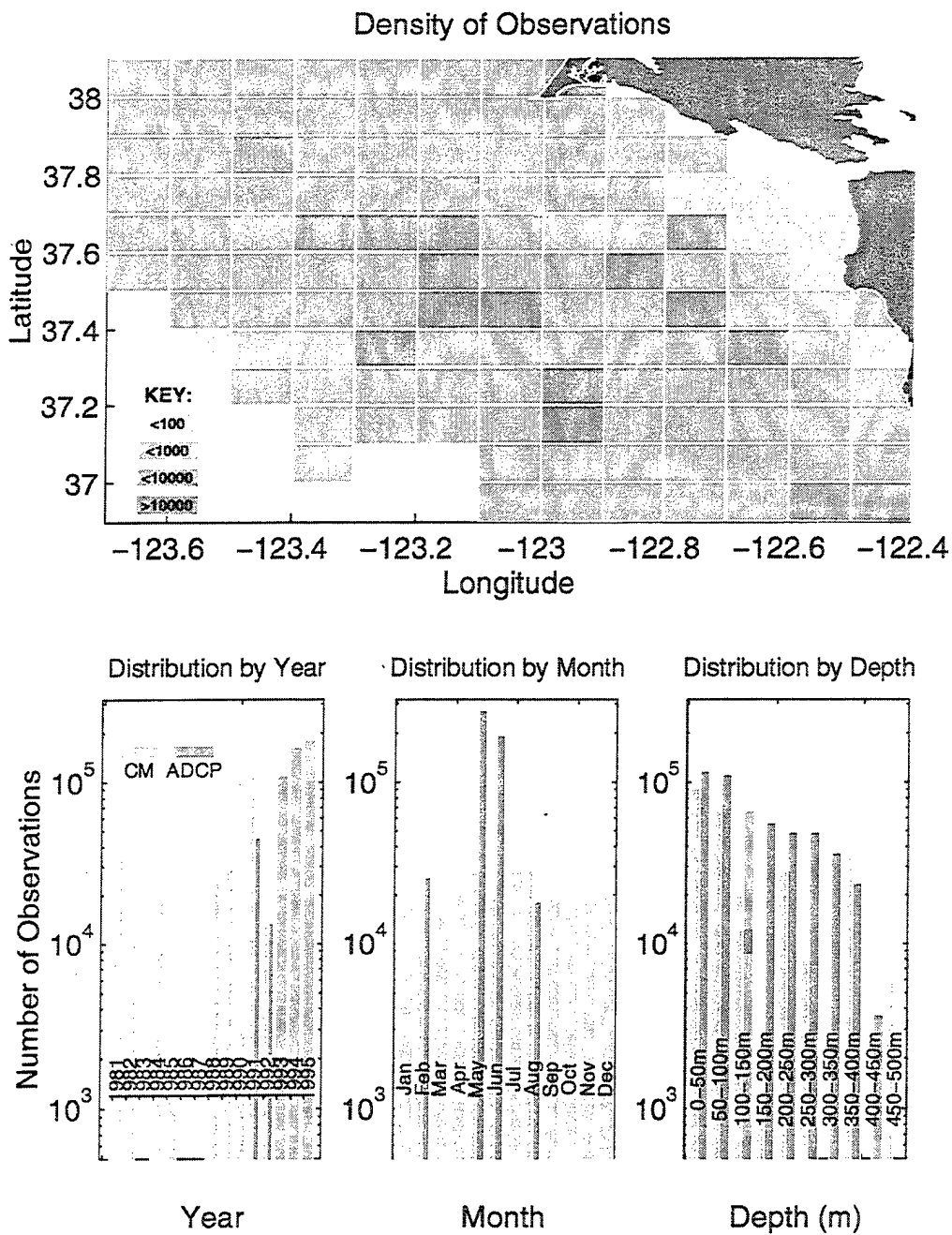


Figure 3.3 Distribution of current meter and ADCP observations used to create the tidal model. a) Spatial distribution. Number of observations in each $1/10^\circ \times 1/10^\circ$ square is indicated by shading per the legend. The highest density areas correspond to locations of current meter moorings. b,c,d) Distribution of observations by year, month, and depth. Number of observations are broken into ADCP and current meter (CM) per legend in (b). The y-axes have logarithmic scales. All ADCP data were collected since 1991. The NMFS Tiburon cruises account for the large number of ADCP observations in May-June, 1993-95.

The three years represent a total of approximately 80 days of ADCP data collected within the Gulf. Because the springtime NMFS Tiburon cruises collected the largest data sets, the years 1993-95 and the months of May and June have by far the greatest temporal density of observations.

ADCP and current meter data were also collected in 1991 and 1992 during the Slope/Shelf Experiment (SSE). The primary purpose of the year-long SSE, funded by the Environmental Protection Agency and Naval Facilities Engineering Command, Western Division, was to determine the subtidal circulation in the region and how it may affect dredge spoils deposited on the shelf and slope. The study included five ADCP and CTD cruises (February, May, August, and October 1991; and February 1992) of 6-7 days length. Six current meter moorings were deployed from February 1991 thru February 1992, spanning the cruise dates (SSE-A to F in Figure 3.1). The collection and processing of the ADCP data is described by Jessen et al. (1992a,b,c,d) and Rago et al. (1992). The October 1991 ADCP data were not used because they were not processed correctly until after the tidal model was run. Kinoshita et al. (1992) describe the collection and processing of the current meter data. Data from 22 instruments deployed during this study were included in the model.

The US Geological Survey and Corps of Engineers sponsored a series of moorings in 1989 and 1990 to study sediment transport patterns in the Gulf. The hourly data from these moorings (346, 334, 335, 1M, and B1B in Figure 3.1), which total 12 meters, were included in the study. Mooring 346 was deployed for 1½ months; 334, 335, and 1M for five months; and B1B for thirteen months. The moorings are described in detail in Noble and Gelfenbaum (1990) and Sherwood et al. (1989).

Two current meter moorings containing two instruments each (CCCCS-K and -L in Figure 3.1) were deployed in the Gulf of the Farallones for twelve months in 1984 as part of the Central California Coastal Circulation Study (CCCCS), a study of the slope and shelf currents between Pt. Conception and San Francisco Bay (Bratkovich et al., 1991; Chelton et al., 1987; Chelton et al., 1988). Two moorings (H3 and H4 in Figure 3.1) were also deployed in the Gulf in 1981 and 1982 as part of SuperCODE (Coastal Ocean Dynamics Experiment) (Denbo et al., 1984; Strub et al., 1987). H4, the deeper mooring, was repeatedly hit by fishermen so that the records from its three meters are fairly short and broken. The entire record (fifteen months) from the single meter on H3 was used in the tidal model.

D. BUILDING THE EMPIRICAL TIDAL MODEL

This tidal model extends the tidal analysis methods of Foreman (1978), where the observed velocity is decomposed into a mean steady current and tidal currents that vary in time at a finite number (n) of frequencies. An amplitude and phase for each tidal frequency are estimated by expressing the linear current meter record in the form:

$$u(t) = u_0 + \sum_{k=1}^n a_k \cos(2\pi\omega_k t) + b_k \sin(2\pi\omega_k t)$$

$$v(t) = v_0 + \sum_{k=1}^n c_k \cos(2\pi\omega_k t) + d_k \sin(2\pi\omega_k t)$$

where ω_k is the tidal frequency for the k^{th} constituent and u and v are the observed total velocity components at each time t . The coefficients a_k , b_k , c_k , and d_k are solved for using the method of least squares, which subsequently can be used to predict u and v for any time t . Candela et al. (1990, 1992) incorporated spatial variation into the method:

$$u(\lambda, \phi, t) = u_0(\lambda, \phi) + \sum_{k=1}^n [(a_k + b_k \lambda + c_k \phi) \cos(2\pi \omega_k t) + (d_k + e_k \lambda + f_k \phi) \sin(2\pi \omega_k t)]$$

$$v(\lambda, \phi, t) = v_0(\lambda, \phi) + \sum_{k=1}^n [(g_k + h_k \lambda + i_k \phi) \cos(2\pi \omega_k t) + (j_k + k_k \lambda + l_k \phi) \sin(2\pi \omega_k t)]$$

where λ and ϕ are longitude and latitude.

Candela et al. vertically integrated the ADCP observations for input to their model. However, current meter observations in the Gulf of the Farallones show marked variations in tidal amplitude and phase at different depths on the same mooring (Figure 3.2, Tables A2-A5). We therefore included depth (z) in the spatially varying model:

$$u(\lambda, \phi, z, t) = u_0(\lambda, \phi, z) + \sum_{k=1}^n [(a_k + b_k \lambda + c_k \phi + d_k z) \cos(2\pi \omega_k t) + (e_k + f_k \lambda + g_k \phi + h_k z) \sin(2\pi \omega_k t)]$$

$$v(\lambda, \phi, z, t) = v_0(\lambda, \phi, z) + \sum_{k=1}^n [(i_k + j_k \lambda + k_k \phi + l_k z) \cos(2\pi \omega_k t) + (m_k + n_k \lambda + o_k \phi + p_k z) \sin(2\pi \omega_k t)]$$

Coefficients for the mean current and each tidal frequency are combined into a single matrix and fitted simultaneously to the observed velocities using the method of least squares.

The form of the coefficients can be chosen to best interpolate across the model region. For reasons explained below, we have chosen linear coefficients ($a_k + b_k \lambda + c_k \phi + d_k z$). If the tides are believed to be affected by frictional forces, a higher-order function could be added for depth (e.g., $a_k + b_k \lambda + c_k \phi + d_k z + e_k z^2$). If baroclinicity varies with latitude, a coefficient to deal with that could be added: ($a_k + b_k \lambda + c_k \phi + d_k z + e_k \phi z$). Higher-order polynomial forms provide a better fit to the data within the domain of the observed data. The advantage of

lower-order polynomial coefficients (linear being the lowest) is that, as noted by Candela et al. (1990, 1992), the model is better behaved near the boundaries of the data coverage. This is especially important if the model is used to predict tides beyond the boundaries of the region where data are available or into data gaps. The coefficients can also be expressed using transcendental forms such as the multi-dimensional biharmonic Green's function (Candela et al., 1990, 1992) in place of polynomials.

The slope/shelf bathymetry in the Gulf of the Farallones seem to call for a second-order polynomial (to best fit the slope and shelf regimes) or a third-order (to fit rise, slope, and shelf regimes). However, Steiner (1994) created several synthetic data sets of mixed steady and tidal currents, then tried to reconstruct the signals using the Candela method. He determined that higher orders of fit could actually cause serious misrepresentations of the tidal flows due to overfitting of the spatial structure and incorrect energy allocation. He recommended that, unless the tidal structure is already well understood, linear polynomials for the tides were the safest form. Allen (1995) also experimented using linear vs. second-order polynomials to detide ADCP data in the Iceland-Faeroes Strait and concluded that arbitrarily increasing the order did not significantly improve the tidal fit.

Another advantage of using linear polynomials is that less computer resources are needed. This can be significant considering the size of the data set used here, where the least squares calculation involved inverting a 700,000 by 36 element matrix.

Computing the coefficients of the linear 3-D tidal model and using them to predict tides or determine tidal ellipse characteristics is straightforward and presented in Appendix B.

E. RESULTS

The tidal model was run with several combinations of current data sets (Figures 3.4-9). Tidal ellipses were estimated for the M_2 , S_2 , K_1 , and O_1 constituents for all available data (Case 1), data from all the current meters (Case 2), ADCP data from the NMFS Tiburon surveys (Case 3), ADCP data from the May 1991 SSE cruise (Case 4), ADCP data from four SSE cruises (Case 5), and data from the NMFS Tiburon surveys divided into northern and southern fields (Case 6). The modeled mean flow and positions of the observations are also shown in each figure. Table 1 summarizes the model runs and the size and seasonality of the input data sets. The results varied, sometimes dramatically, depending on the quantity, type, seasonality, and coverage of the input data.

1. Case 1

When all available current meter and ADCP data are used to create the tidal model (Figure 3.4), the constituent fields show the characteristics expected from the tides calculated from current meter series.

The M_2 tide follows the bathymetry through the Gulf except near the Golden Gate, where its orientation adjusts to tidal flow through the Gate. Maximum velocities are fairly consistent, ranging from 3-5 cm/s. The highest velocities are on the shelf near the Gate. Tidal ellipses are mostly rectilinear. The S_2 tide also follows the bathymetry and does not appear to be affected by the tidal jet through the Gate. Maximum velocities vary considerably. Velocities approach 3 cm/s in deep water and near the Gate, but diminish near the shelf break. There appears to be a point near 37.5°N, 123.0°W where the tidal velocities

Characteristics of Data used in Model Runs				
Case	Figure	Data used to create the tidal model	Number of observations	Seasonality
1	4	All available ADCP and current meter data	704,780	All seasons
2	5	All available current meter data	254,651	All seasons
3	6	ADCP data from the three Tiburon Rockfish survey cruises	455,090	May-June
4	7	ADCP data from the May 1991 SSE cruise	14,554	May
5	8	ADCP data from four SSE cruises	58,359	Feb/May/Aug
6	9	ADCP data from the three Tiburon Rockfish survey cruises divided into northern and southern fields	455,090 (north) 435,512 (south)	May-June

Table 3.1 Characteristics of data used in model runs. Six models of the tides in the Gulf were created, each using different empirical data sets, to show the dependence of the model on the type and quantity of input observations.

Tidal Ellipses at 75m from all Data in the Gulf of the Farallones 1981-95

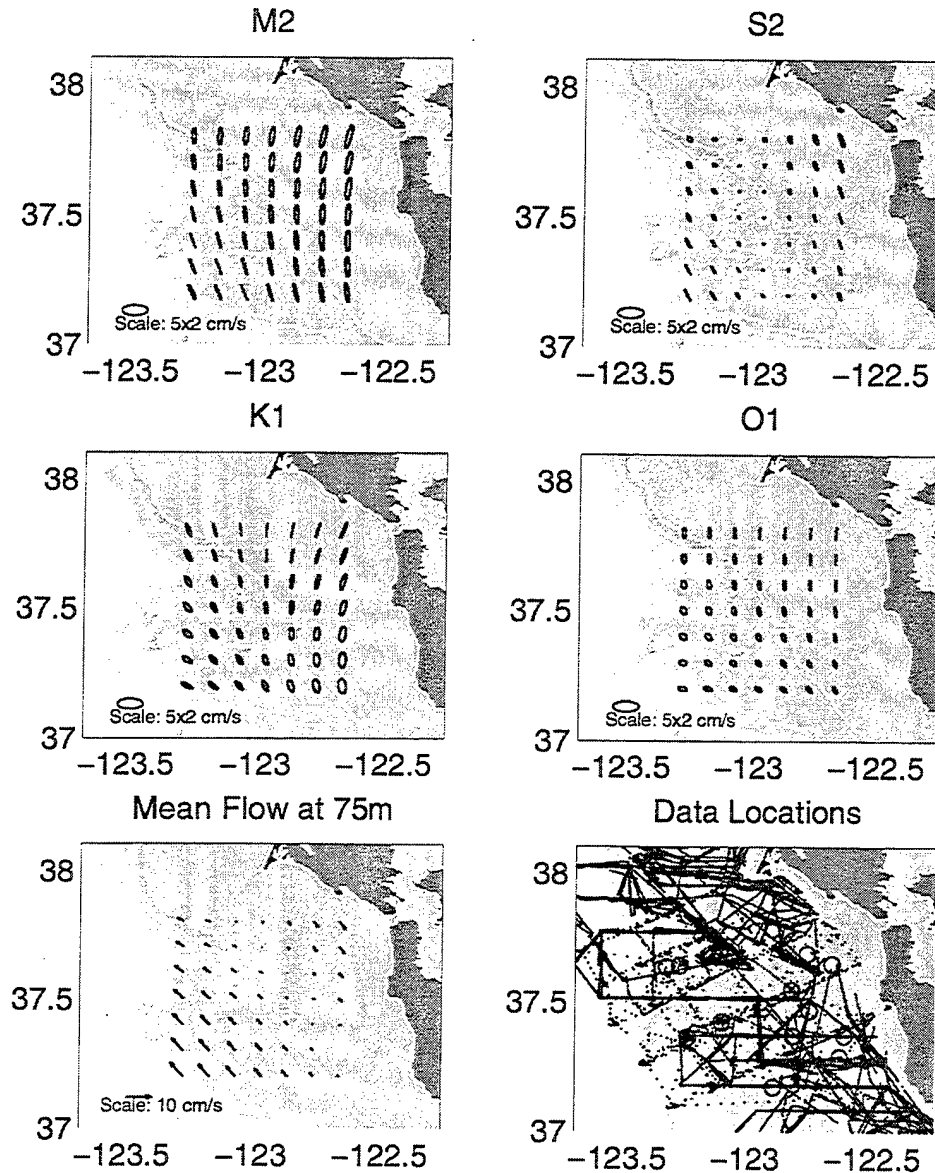


Figure 3.4 Model results using all available ADCP and current meter observations. Model tidal ellipses at 75 m depth on a $1/10^\circ \times 1/10^\circ$ grid between 37.2°N - 37.8°N and between 123.3°W - 122.8°W are plotted for the a) M₂, b) S₂, c) K₁, and d) O₁ tidal frequencies. Scale ellipses with a 5 cm/s semi-major axis and 2 cm/s semi-minor axis are shown. e) Model mean flow at 75 m depth. Scale vector of 10 cm/s is shown. f) Locations of data observations. Locations of ADCP ensembles are shown as a dots. Locations of current meter moorings are indicated by larger open circles.

are near zero. The tidal ellipses are mostly rectilinear but the ellipses become more circular as velocities decrease, especially in the northern part of the Gulf.

The K_1 tide follows the bathymetry throughout most of the Gulf, but near the Gate it is oriented perpendicular to the bathymetry. Since it is not seen in either the Tiburon- or current meter-only models (Cases 2,3), this may be a model artifact. Maximum velocities are in the 2-4 cm/s range, with the highest velocities on the shelf and the lowest velocities near the shelf break. Tidal ellipses are nearly circular in the southeast corner but mostly rectilinear elsewhere. The O_1 tidal field looks similar to that of the K_1 but with lower maximum velocities, in the 1-3 cm/s range.

In the mean flow, poleward flow is seen offshore of the shelf break. Highest velocities are in the southwest corner, over 5 cm/s. Equatorward flow, mostly in the 1-3 cm/s range, is seen on the shelf.

2. Cases 2 and 3

When using all the current meter data (Case 2, Figure 3.5) or all of the ADCP data from the Tiburon cruises (Case 3, Figure 3.6), the tidal fields are comparable to those estimated from the complete data set. Velocity amplitudes fall in the 1-6 cm/s range and orientations of the tidal ellipses, especially offshore, more or less follow the bathymetry. More importantly, results from these two cases look comparable even though they are created using independent data, leading us to believe the empirical method is converging on a consistent solution. There are some differences between Figures 3.5 and 3.6 in the size of the semi-minor axes and small differences in tidal velocities and orientation, especially in the

Tidal Ellipses at 75m from DSJ Cruises in June 93,94,95

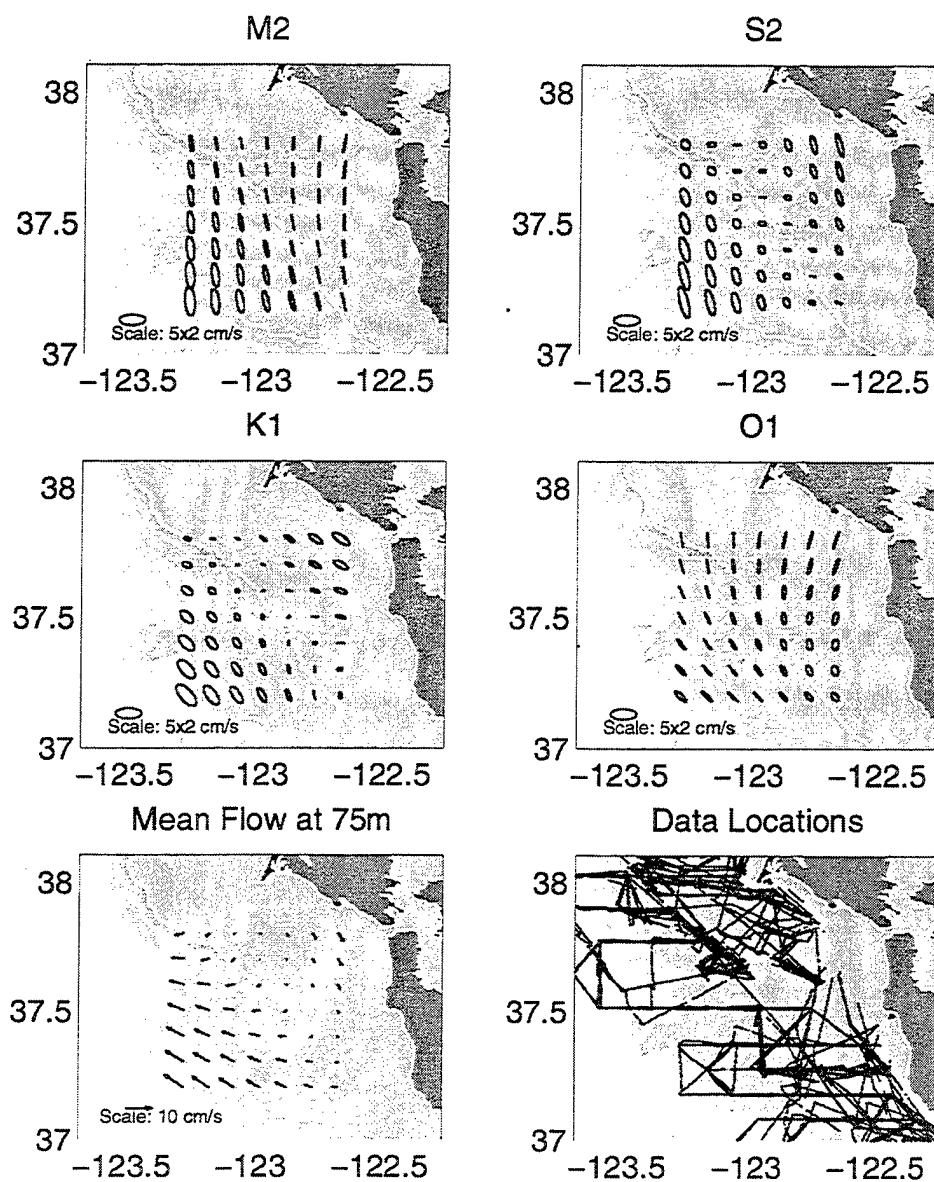


Figure 3.5 Model results using all available ADCP observations from the NMFS Tiburon cruises in May-June, 1993-95. Otherwise, same as Figure 3.4.

Tidal Ellipses at 75m from all Current Meter Moorings

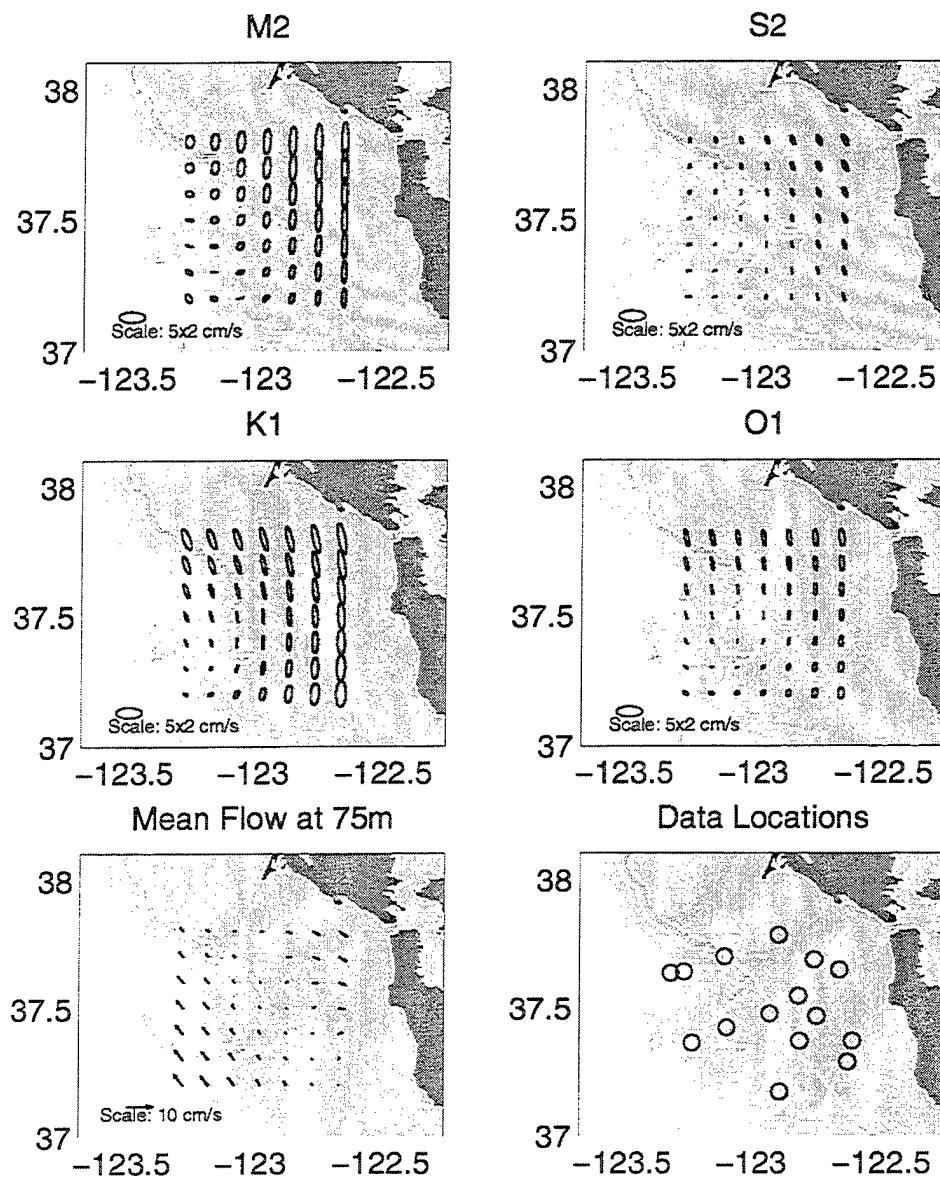


Figure 3.6 Model results using all available current meter observations. Otherwise, same as Figure 3.4.

corners of the model domain where data observations were sparse. But on the whole the tidal fields are comparable and the similarity in the mean flow fields is striking.

An interesting feature of the model run with the current meter data alone (Figure 3.5) is the apparent amplification of tides over the shelf. This effect was previously noted in the diurnal tides by Noble and Gelfenbaum (1990). Amplification of this sort has also been seen over the Yermak Plateau (Prazuck, 1991). A somewhat different picture is seen in the Tiburon ADCP data model fields (Figure 3.6). Instead of amplification over the shelf, there appears to be a minimum along the shelf break, especially in the K_1 and S_2 . From the data in hand, it is impossible to say whether the minimum is real (perhaps a seasonal effect since the Tiburon data were collected in May/June) or an artifact of the model (perhaps caused by the linear form of the model, a few noisy data points, a relative dearth of ADCP data in the southwest corner of the field, or other problems). However, the shelf break minimum is also seen in the model run with data south of the Farallones region (Case 6, Figure 3.9). To test if the linear polynomial fit causes the "saddle" shape at the shelf break, the Tiburon data were split into two distinct data sets, one over the shelf and one over the slope and deep water. There was a slight ($1/10^\circ$ latitude) overlap in the data sets. Each nearly independent set produced model fields that had velocities that gradually diminished towards the shelf break. This convinced us the choice of polynomials was not the cause of the minimum at the shelf break.

The mean flow fields in the Tiburon and current meter tidal models show similar features to the mean flows in Case 1. Poleward flow, stronger in the springtime Tiburon

fields, is seen offshore over the slope. Weaker, equatorward currents are prevalent over the shelf.

3. Case 4

To test the effectiveness of using ADCP data from a single cruise to characterize the regional tidal fields, the model was run using only data from the May 1991 SSE cruise (Figure 3.7). Model tidal amplitudes are far too high and the tidal fields exhibit areas of extreme convergence and divergence. Ellipse orientations differ wildly from ellipses calculated from current meters (Tables 2-5, Figure 3.2) or from using all data (Figure 3.4). During the SSE cruises, the ship crossed the strongly sheared alongshelf current twice a day, or roughly at the same frequency as the semi-diurnal tidal constituents. Considering the relatively short duration of the cruise, this may bias the model results. Models created using the other individual SSE cruises (not shown) had similar unreasonable characteristics. *In areas of complex tidal patterns or relatively weak tides and strong subtidal currents, data from a single short cruise are insufficient to create realistic empirical tidal estimates.*

4. Case 5

Increasing the data set to four ADCP cruises (Figure 3.8) helps dramatically, but tidal velocities are still too high in some areas and the orientations often appear unrealistic compared to that expected from current meter observations. For example, the M_2 rotation near the Gate is absent, and anomalously strong K_1 currents are seen in the northeast corner of the region. This four-cruise model could be applied to detide the SSE data set, and the overall tidal variance would be reduced, but probably at a cost of inducing abnormal velocities in some areas. The mean flow field features a reasonable poleward flow over the slope and

Tidal Ellipses at 75m from Four SSE Cruises (Feb, May, Aug 91; Feb 92)

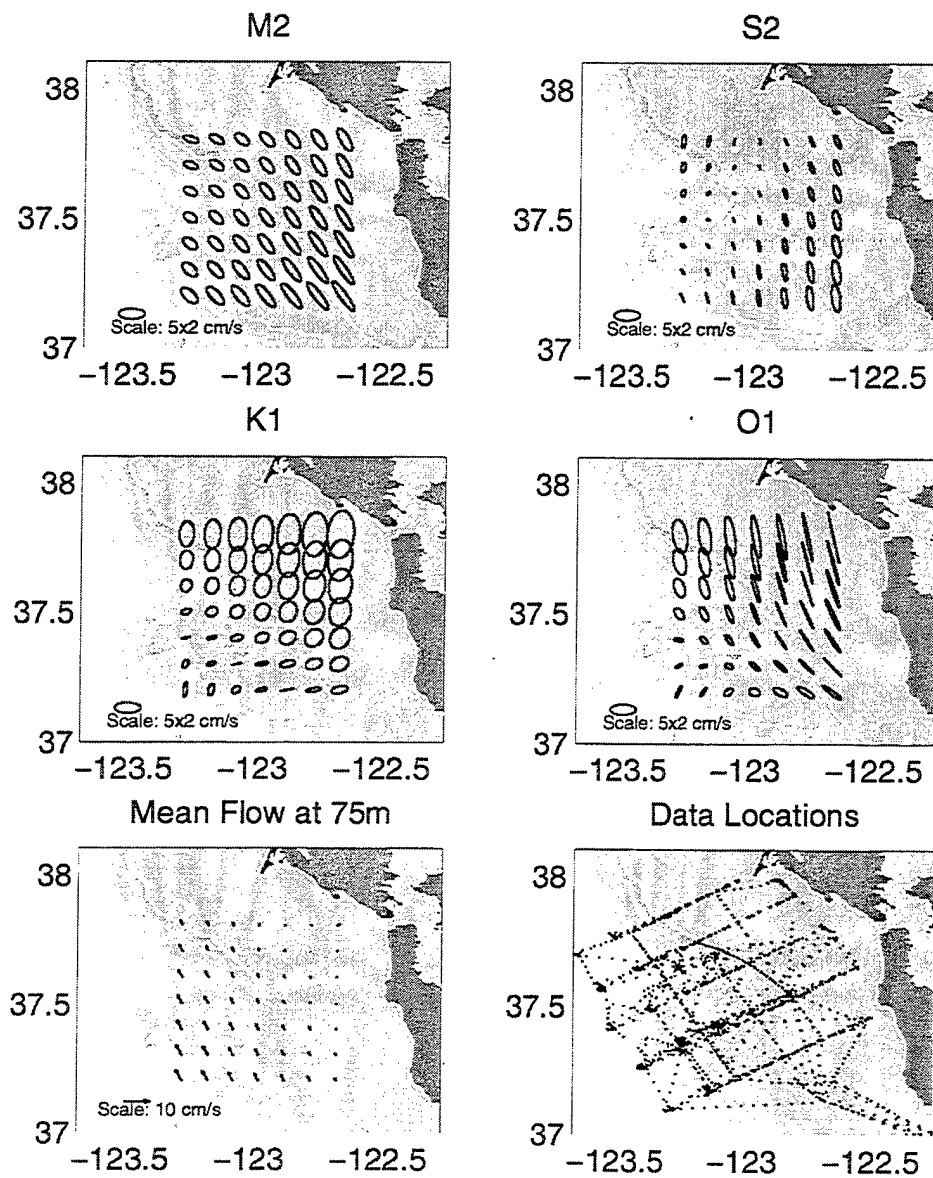


Figure 3.7 Model results using ADCP observations from the February, May, and August 1991 and February 1992 cruises of the Slope/Shelf Experiment (SSE). Otherwise, same as Figure 3.4.

Tidal Ellipses at 75m from ADCP Data in May 91

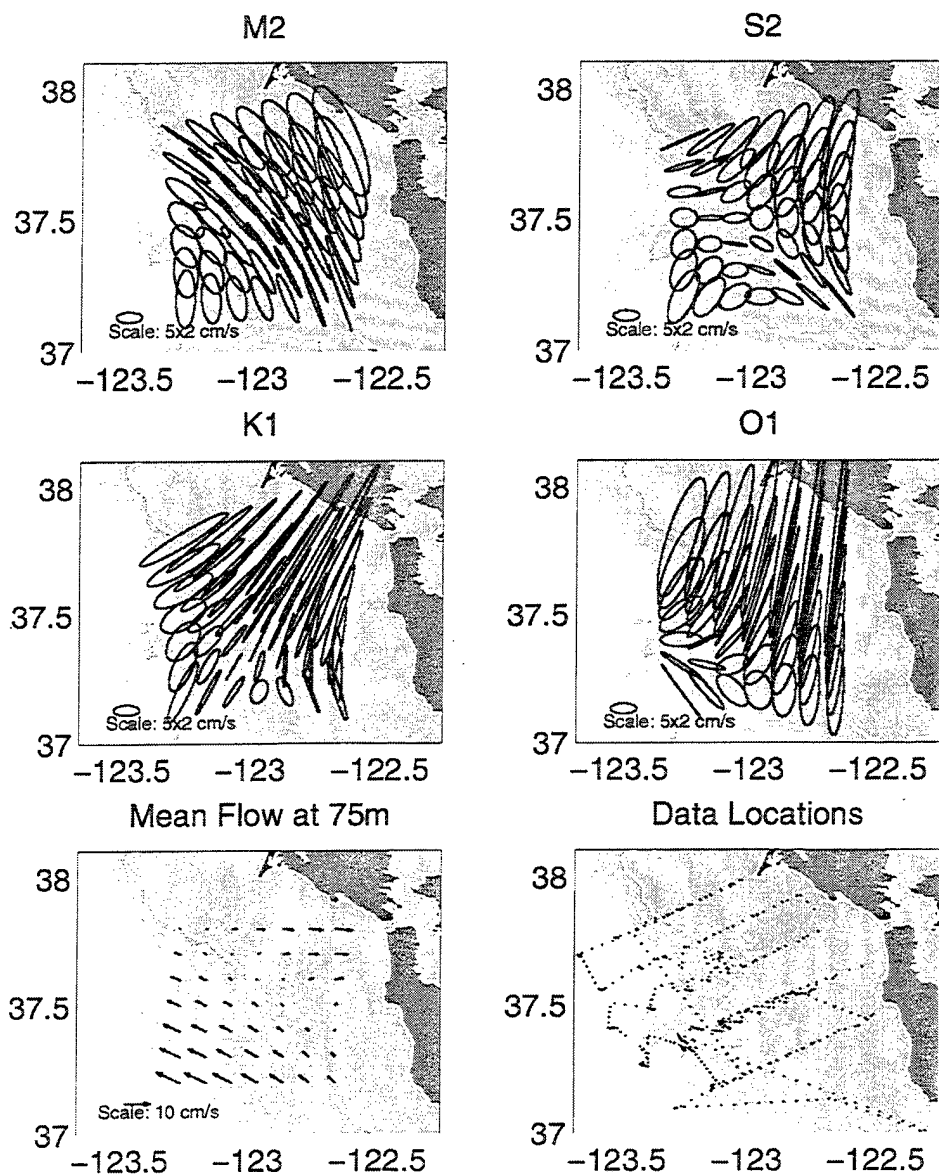


Figure 3.8 Model results using ADCP observations from May 1991 cruise of the Slope/Shelf Experiment (SSE). Otherwise, same as Figure 3.4.

weak and variable currents over the shelf. The mean flow using only the May 1991 cruise data (Figure 3.7) shows greater poleward (equatorward) flow over the slope (shelf) than the total solution which spans all seasons. The seasonal intensification of the countercurrent over the slope in the spring agrees with the findings of Collins et al. (1996) who examined 5½ years (May 1989-February 1995) of current meter data collected off Point Sur (~170 km south of the Farallones) and found an annual signal in alongshore velocity that peaks in June and is weakest in October. The equatorward shelf currents, however, are probably a response to increased equatorward winds. Alongshore surface stress off central California is highest in April-June (Nelson, 1977; Schwing et al., 1996).

5. Case 6

To see how models of two regions would overlap, the model was run with data from the region south of the Gulf (off Monterey Bay). This southern region slightly overlapped the Gulf region (Figure 3.9). Where the models overlap, velocities and orientations are similar, again giving assurance that with sufficient data the model captures the essential characteristics of the tidal fields.

F. MODEL ACCURACY AND SENSITIVITY

From our analysis of the tidal model results using different input data sets, three immediate conclusions are drawn. First, the greater the number of observations used to create the model, the more the tides resemble what we expect to see from tidal analyses of the current meters and our understanding of the tides as poleward propagating Kelvin waves along the eastern boundary of the North Pacific. The second is that models created with

Tidal Ellipses at 75m with Overlapping Models

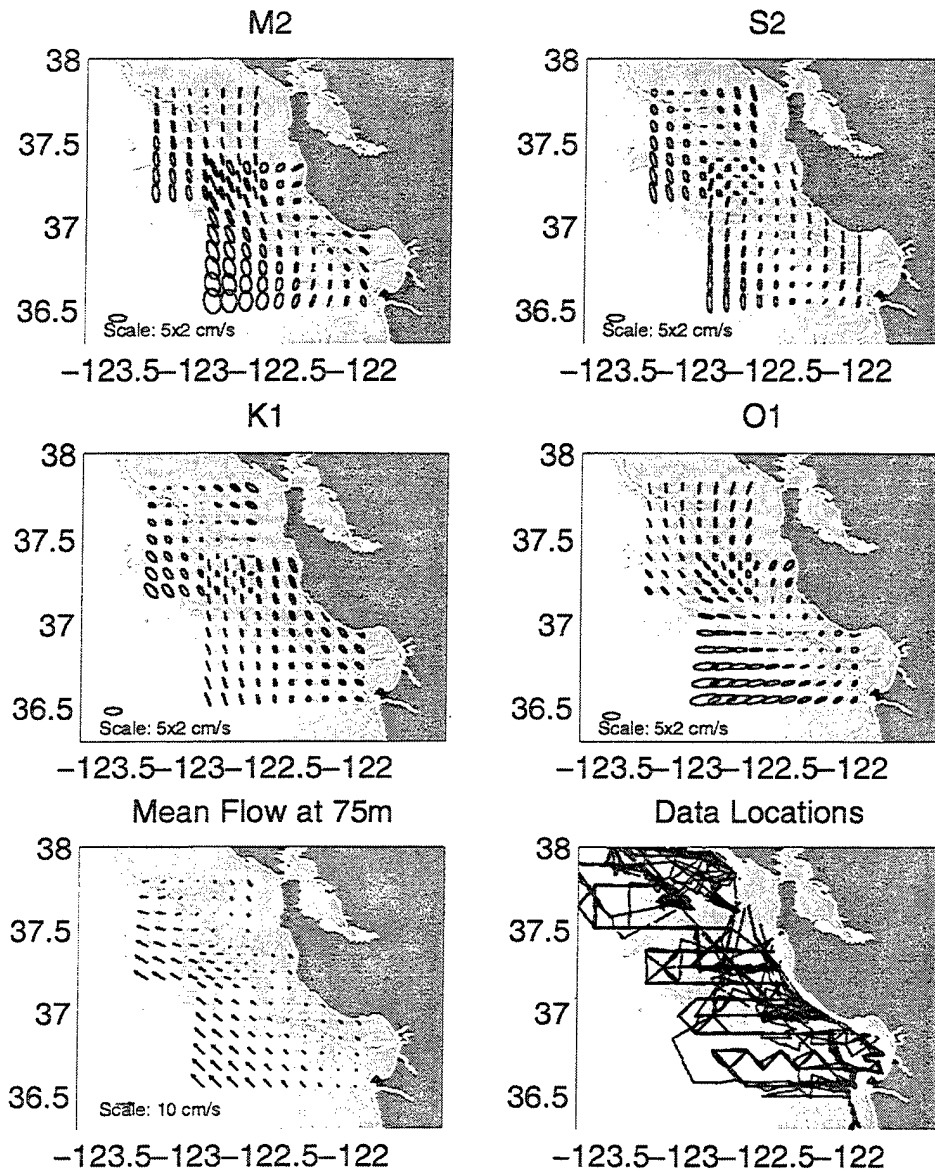


Figure 3.9 Results from two tidal models: one using ADCP data from the northern legs of the NMFS Tiburon cruises and another using data from the southern legs. Model tidal ellipses at 75 m depth for the northern model are shown for a $1/10^\circ \times 1/10^\circ$ grid between 37.2°N - 37.8°N and between 123.3°W - 122.8°W ; for the southern model ellipses are shown for a $1/10^\circ \times 1/10^\circ$ grid between 36.55°N - 37.35°N and between 122.95°W - 122.05°W . f) Locations of ADCP ensembles for the northern model are indicated by small black dots and locations of the ensembles for the southern model are indicated using small circles. Otherwise, same as Figure 3.4.

completely independent (but large) data sets produce tidal constituent fields that show similar structures and patterns. Third, the amount of data used as input to the model is critical.

In general, when larger data sets are input, the model reproduces most of the features of the expected mean and tidal fields. The tides mostly follow bathymetry. The diurnal tides are amplified over the shelf. The influence of tidal flow through the Golden Gate is evident. Tidal velocity amplitudes are in the range seen by fixed current meters. Mean poleward flow offshore and equatorward flow on the shelf is indicated. The model is not sophisticated enough, however, for us to say with confidence that other features, such as the velocity minimum near the shelf break, are real.

Although capable of solving for all tidal constituents, the model applied here determines only four constituents. Tidal analysis of the region's current meter records shows there is considerable energy at other frequencies, especially the P_1 ($P_1/K_1 \sim .4$), N_2 ($N_2/M_2 \sim .25$), and K_2 ($K_2/M_2 \sim .25$). Some of the features we see may be artifacts caused by "beating" between adjacent analyzed and non-analyzed frequencies.

Spectral analysis of the current meter records also shows considerable energy at the local inertial frequency (19.6 hours). In addition, the tidal jet and interactions of the current with the steep continental slope may be constant sources of inertial energy. Internal tides and inertial motions are not addressed in the model since they are usually intermittent. It is also assumed that the tides are stationary on seasonal and longer time scales. Tidal analyses on 18-day segments from several current meters supported this assumption.

The size of the input data set needed to adequately resolve the currents is probably a function of the complexity of the mean and tidal circulations in a region, as well as their

relative magnitude. To estimate the statistical accuracy of our tidal models using the various input data sets (Table 1), a variant of the bootstrap method (Kinsella, 1986) is applied. The bootstrap method measures the sensitivity of the empirical method to the distribution and quantity of input data.

The bootstrap is run as follows: a sample set of n observations is built from the original n -length data set by randomly selecting an observation and “replacing it” before making the next random selection. Because of replacement, the sample set may have duplicates of or lack some observations from the original set. The model is run using the sample set and model output values recorded. This was repeated 128 times, after which histograms of the model output values were normally distributed (Figure 3.10) and statistical properties could be derived. Standard errors were calculated for the 75 m output values in a $1/10^\circ \times 1/10^\circ$ grid and contoured (Figure 3.11). The standard errors of the mean flow and ellipse characteristics of the M_2 and K_1 tides are shown for the models using only the ADCP observations from the May 1991 SSE cruise (Case 4), all ADCP data from four SSE cruises (Case 5), ADCP data from the Tiburon cruises (Case 3), all current meter observation (Case 2), and all observations (Case 1). The S_2 and O_1 model errors (not shown) are similar to the M_2 and K_1 , respectively.

Areas of high error in the orientation and phase are associated with regions of almost circular tidal ellipses (Figures 3.4 -8). Because small changes in the length of the axes of nearly circular ellipses can produce large changes in phase and orientation, statistics in these cases become ambiguous. For large data sets, generally, standard errors are less than 0.2 cm/s and 2° for tidal amplitude and phase, respectively, and less than 0.1 cm/s for mean flow.

Histograms for K1 -- SSEADCP Bootstrap w/ 128 Replications

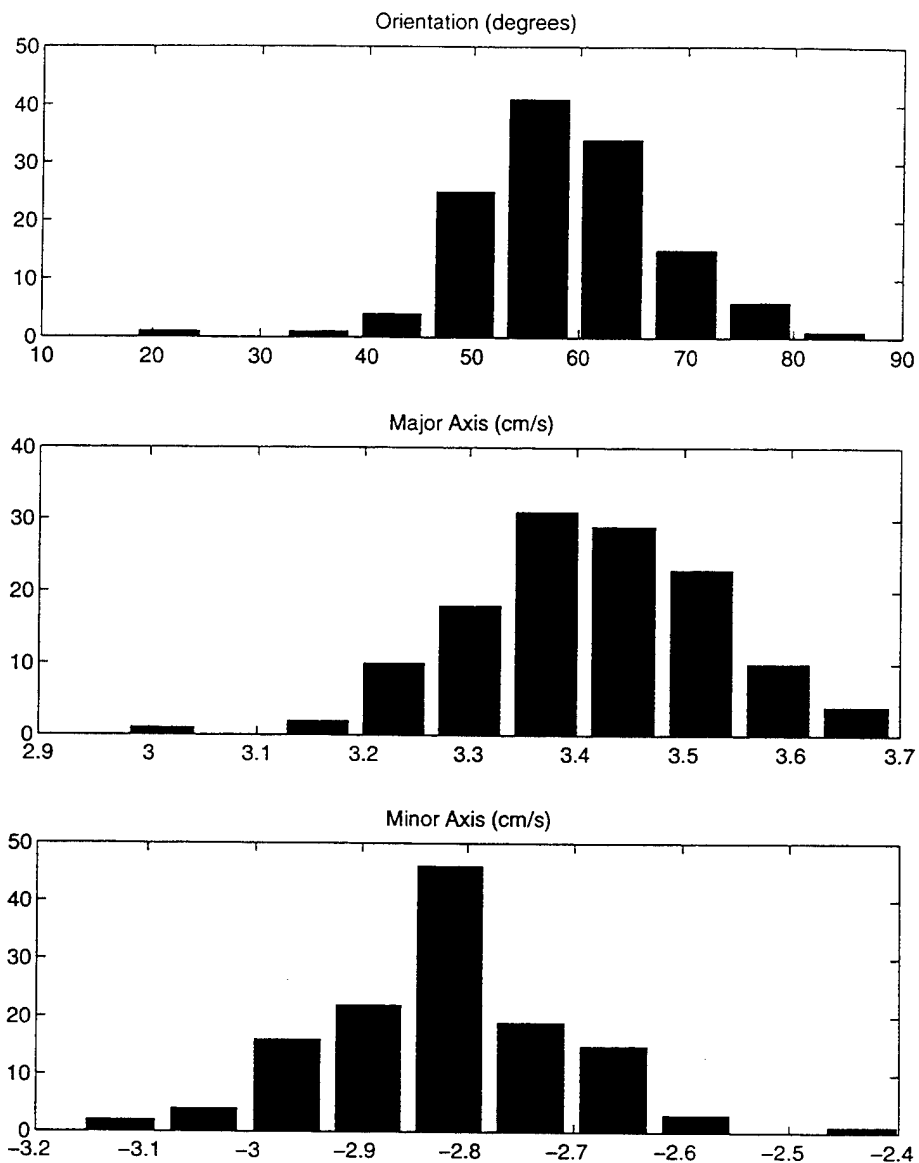


Figure 3.10 Histograms of values of a) orientation (deg), b) semi-major axis (cm/s), and c) semi-minor axis (cm/s) of the K_1 tidal ellipse at the center of the model domain ($37.5^\circ\text{N}/123.0^\circ\text{W}$) after 128 repetitions of the bootstrap using only the ADCP data from four Slope/Shelf Experiment (SSE) cruises.

Standard Errors of Model for Various Input Data Sets

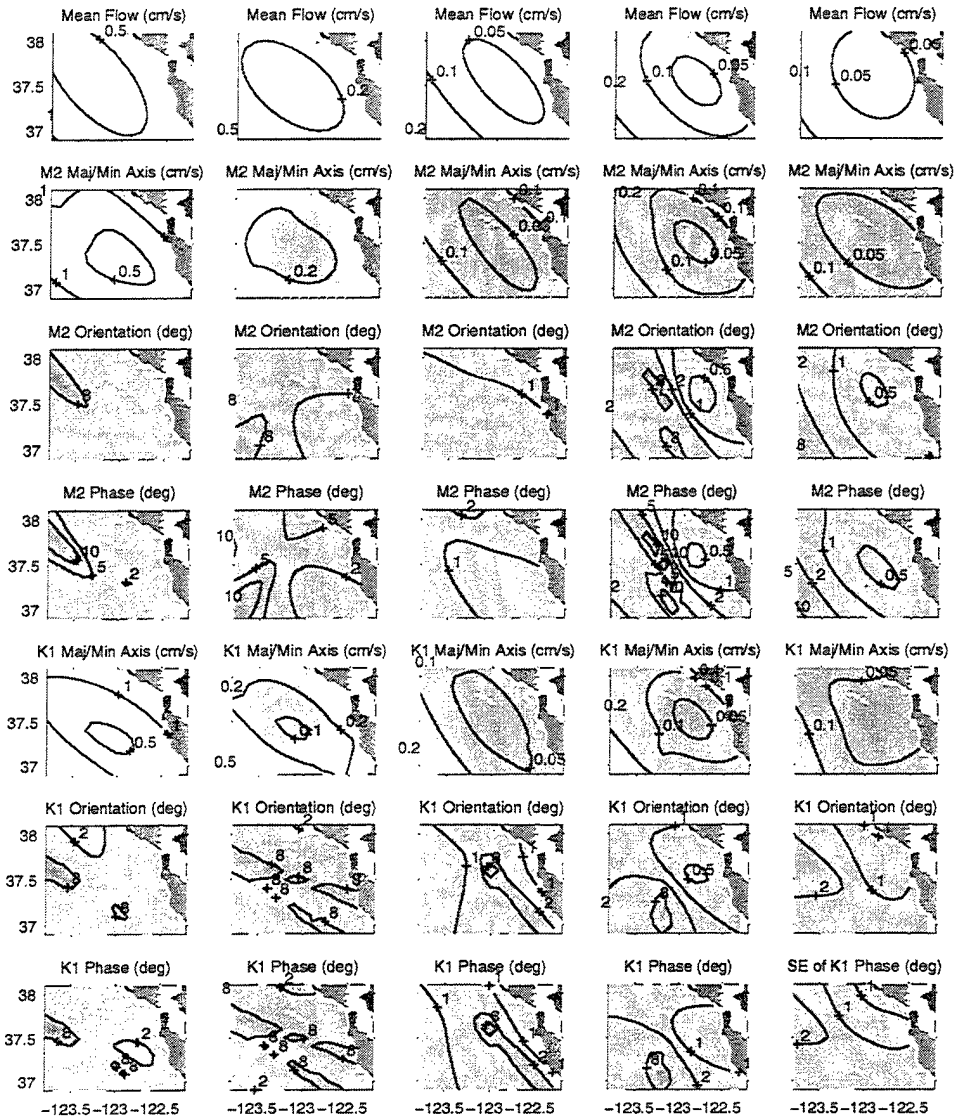


Figure 3.11 Contours of standard errors of the mean flow and M_2 and K_1 tidal ellipse parameters for the tidal models created with a) (left column) only ADCP data from the May 1991 Slope/Shelf Experiment cruise, b) (2nd column) ADCP from four Slope/Shelf experiment cruises, c) (3rd column) ADCP data from the three NMFS Tiburon cruises, d) (4th column) all available current meter data, and e) (right column) all available ADCP and current meter data. Standard errors were calculated using the bootstrap method for locations on a $1/10^\circ \times 1/10^\circ$ grid throughout the model region. Down each column are i) (top) contours of standard error of the mean flow, ii) contours of standard error of the semi-major axis of the M_2 tidal ellipse with background shading where darker shades indicate regions of smaller standard errors of the M_2 semi-minor ellipse, iii) contours of standard error of the orientation of the M_2 tide with background shading indicating regions where the tidal ellipse is less (lighter shades) or more (darker shades) eccentric, iv) contours of standard error of the phase of the M_2 tide with background shading also indicating less (lighter shade) or more (darker shade) tidal ellipse eccentricity, v,vi,vii) same as subfigures ii, iii, and iv except calculated for the K_1 tidal constituent.

The larger the input data set, the smaller the standard errors of the model outputs (Figure 3.12). For example, at the center of our model domain (123°W , 37.5°N) the standard error for the M_2 amplitude drops from 0.4 cm/s for our May 91-only model (14,554 observations) to less than 0.03 cm/s for a model using all the data (704,780 observations) (Figure 3.11). The standard errors drop by an order of magnitude as the number of input data increases from 14,000 to 200,000 observations, after which additional observations add little to the statistical accuracy. The bootstrap method thus provides a means of estimating how many observations are necessary in a region to produce a reasonable model. For $O(200,000)$ observations, the standard errors of the model are small, less than 0.05 cm/s ($\pm 2\%$) for both the mean flow and the tidal ellipse axes.

Another test of the model is to compare the values of the tidal ellipse parameters calculated from current meter time series to the values estimated by the model for the same location and depth. Comparisons are shown in Figure 3.13 for the length and orientation of the M_2 semi-major axes for the current meters closest to 75 m depth on each mooring used in the model. The model (Case 1 using all available data) does not capture the high M_2 velocities found at a few of the moorings, leading to a correlation coefficient of $r=0.41$. The mean of the length of the semi-major axes at the 75 m-depth current meters is 5.5 cm/s while the mean of the values at the same location and depth produced by the model is 3.5 cm/s. There was somewhat less variability in the orientation of the M_2 ellipses calculated from the mooring data so the model has an improved $r=0.66$. The mean current meter M_2 orientation is 90.6° (relative to east) while the mean model orientation is 94.3° . Correlations would probably be higher if the model were run to fit the tides to higher degree polynomials than the

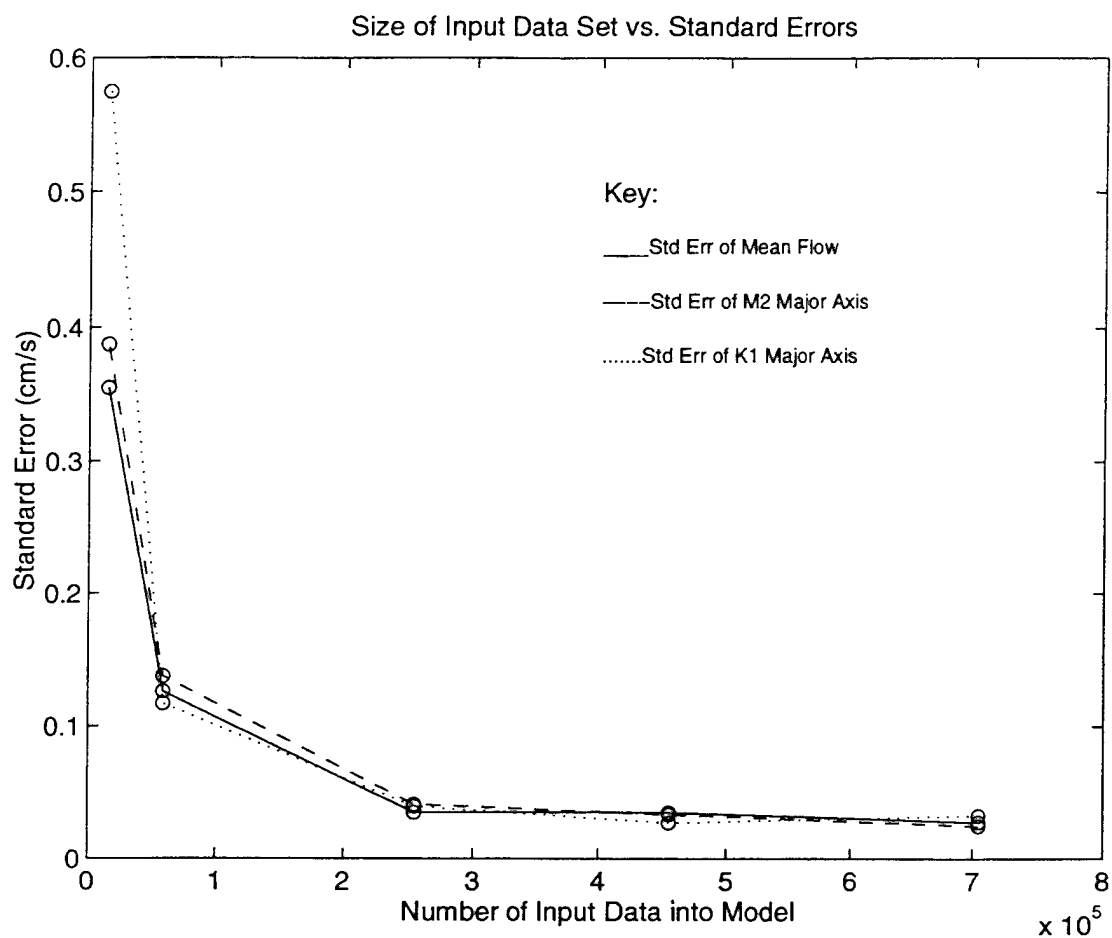


Figure 3.12 Relationship between the number of observations input into the tidal model and the standard errors of the mean flow and the semi-major axes of the tidal ellipses of the M2 and K1 tides.

Comparison between Model and Current Meter Values near 75 m

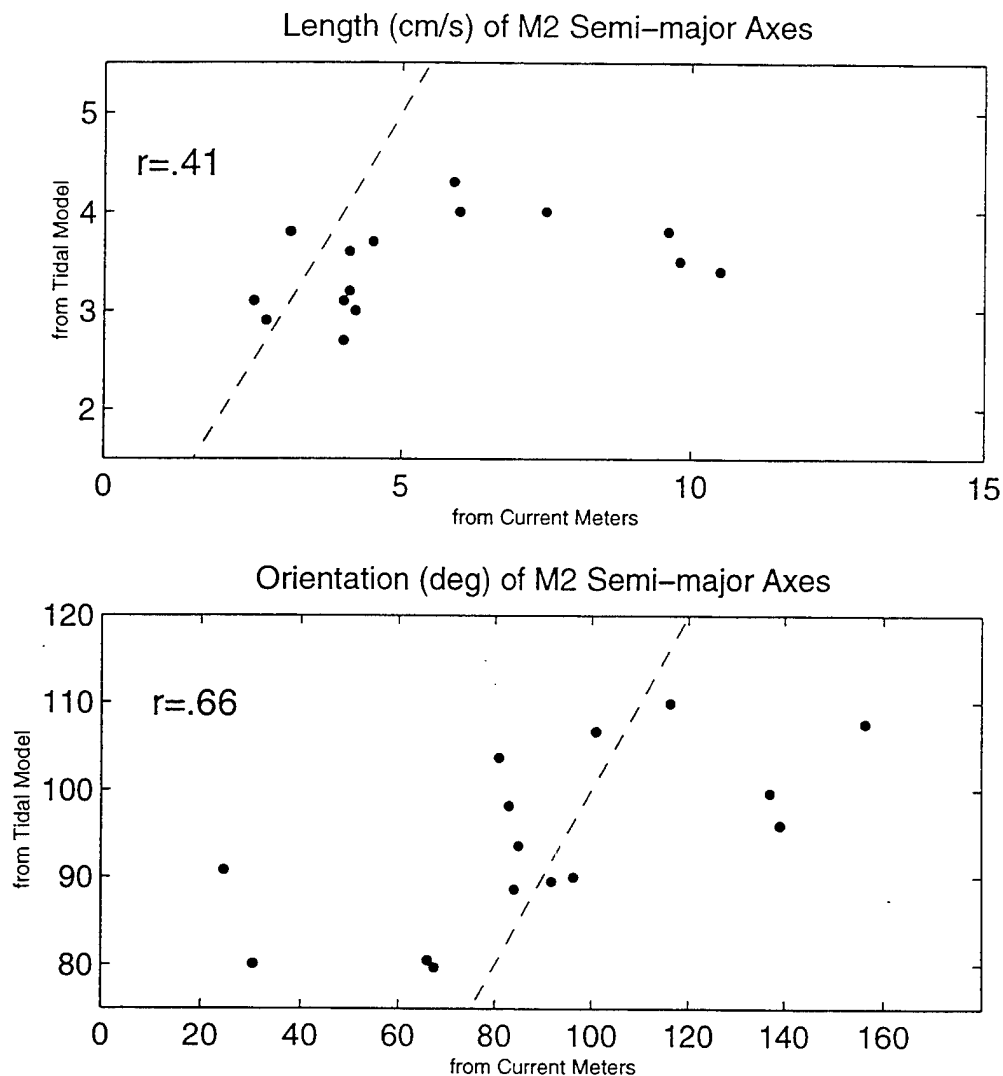


Figure 3.13 Comparison between M2 semi-major axes length and orientation calculated at current meter instruments near 75 m depth and estimated by the tidal model (Case 1) for the same positions and depths as the current meters. The dashed lines have slope=1 and pass through the origin. "r" is the value of the correlation coefficient which relates how much of the variance in the current meter data is explained by the tidal model.

linear fit used here, but current meter data are notoriously noisy and the model might merely fit non-tidal signals.

Models run with smaller-sized data sets are also subject to problems meeting the Rayleigh criterion. Godin (1972) points out that to resolve two tidal frequencies, the length of observations must exceed one cycle of the difference between the frequencies, i.e., $n\Delta t \geq |\omega_1 - \omega_2|^{-1}$, where $n\Delta t$ is the measuring period. This is inadequate for spatial tidal analysis, so we define a multi-dimensional Rayleigh criterion:

$$n\Delta t d^{-1} \geq |\omega_1 - \omega_2|^{-1}$$

where d is the number of dimensions in the model. Since our model uses linear coefficients ($c_1 + c_2\lambda + c_3\phi + c_4z$), $d=4$. The multi-dimensional criterion assumes that observations are evenly distributed in space and time. An ADCP record, consisting of an ensemble of velocity observations at depth intervals beneath the ship, could be used to resolve linear tides in two dimensions (t and z) so can be counted as two observations. Thus, the $\sim 500,000$ unique observations in t , λ , ϕ , and z with the ADCP count as $\sim 30,000$ observations (using 30 as the average number of depths per ensemble). Also, 15-minute averaged ADCP data were used. With this number, our model meets the criterion for $[(15,000 \text{ ADCP records})(2 \text{ obs/record})(\frac{1}{4} \text{ hr})(4)^{-1} + (200,000 \text{ current meter obs})(1 \text{ hr})(4)^{-1}]^{-1} = 2 \times 10^{-5} \text{ hr}^{-1}$, which is sufficient to resolve all standard tidal frequencies. In general, a $d=3$ model would need 39 hourly ADCP records to discriminate between the diurnal K_1 and semi-diurnal M_2 , 532 hourly ADCP records to discriminate between the M_2 and S_2 tides. For $d=4$, 52 and 709 hours would be needed, respectively.

In the Case 1 (using all available data) baroclinic model, the M_2 , S_2 , K_1 , and O_1 tides account for 10.3% of the variance in u (east-west flow) and 17.8% of the variance in v (north-south flow), less than the tidal variance typically found in current meter records in the Gulf, 29-50% in u and 45-58% in v (Noble and Gelfenbaum, 1990). The linear model incorporating many separately collected data sets over a large region cannot separate the tides quite as well as conventional analysis techniques performed on a stationary data set.

We expected from the historical current meter analyses that the tidal model would find significant variation with depth. In fact the model output, especially when large data sets are used as input, show very little variation with depth. When the model is run using all available data but without a z (depth) dependence, the tidal fields are nearly identical and almost the same amount of tidal variance is accounted for: 10.1% in u and 17.6% in v . It turns out that fitting many seasons and years of observations into linear time, latitude, longitude, and depth functions averages out any depth variations in what is seasonally a barotropic system. Tidal ellipses estimated from the model for 75 m depth (Figures 3.4 -9) are in some places plotted where the depth of water is too shallow for this to be realistic, but as the model varies little with depth and does not incorporate near-bottom friction, the results can be interpreted to represent a mid-layer depth.

Further improvements on the method used here are possible. The creation of the model is currently unconstrained except by the observational data. The model would presumably be improved if bathymetric or astronomical constraints could be incorporated. Although tidal sea levels may have different phasing and in some places different amplitudes than tidal currents, it may be possible to include sea level and bottom pressure observations

into the model. This would be a useful addition since in most areas sea level observations are more plentiful and easier to obtain than current observations.

G. CONCLUSION

This work initially addressed whether, in an area such as the Gulf of the Farallones with complex tidal currents, large mean currents, and probably large internal tides and inertial oscillations, the tidal energy can be reasonably removed from ADCP and current meter observations using the technique of Candela et al. (1990,1992). We have shown that, with enough data, 4-D velocity data can be “detided” and that, in addition, a realistic estimate of tides model is possible. The sensitivity of the model to the amount of input data is critical. Confidence is gained when models run with independent data sets reveal similar features and characteristics. The error of the method can be determined using a bootstrap-type error analysis. It can be dangerous to model tides with small data sets in complex regions, although if the technique is used solely to estimate the mean flow fields smaller data sets may be acceptable.

IV. SEASONAL VARIABILITY OF THE CIRCULATION AND WATER MASSES IN THE GULF OF THE FARALLONES

A. INTRODUCTION

It is surprising that a region as well traversed as the Gulf of the Farallones (Figure 4.1), gateway to San Francisco, has been studied so little. South of the Gulf, Monterey Bay has received a great deal of scientific attention. Similarly, the waters north of the Gulf have been the focus of a number of large experiments in the last two decades, including the Coastal Ocean Dynamics Experiment (CODE), Northern California Coastal Circulation Study (NCCCS), and Coastal Transition Zone (CTZ) programs. The few details we know about the circulation in the Gulf are from a handful of cruises and current meters deployments or have been extrapolated from our understanding of the adjacent regions.

A line of hydrographic stations through the Gulf of the Farallones was occupied frequently during the heyday of the CalCOFI (California Cooperative Oceanic Fisheries Investigations) program. Using hydrographic data from Nansen bottle measurements collected during forty-five CalCOFI cruises between 1952 and 1984, Bray and Greengrove (1993) constructed a mean picture of the geostrophic currents through a southwesterly line off Pt. Reyes (Figure 4.2). They found equatorward flow (up to 5 cm/s) in the upper 100 m and throughout the water column beyond 150 km from the coast. Below 100 m depth they found weak poleward flow (<1 cm/s) within 150 km of the coast. They calculated that the equatorward flow transports 1.3 Sv (1 Sv= 10^6 m³/s) and the poleward flow carries 0.1 Sv. However, their results are based on hydrographic stations spaced 30-75 km apart which begin

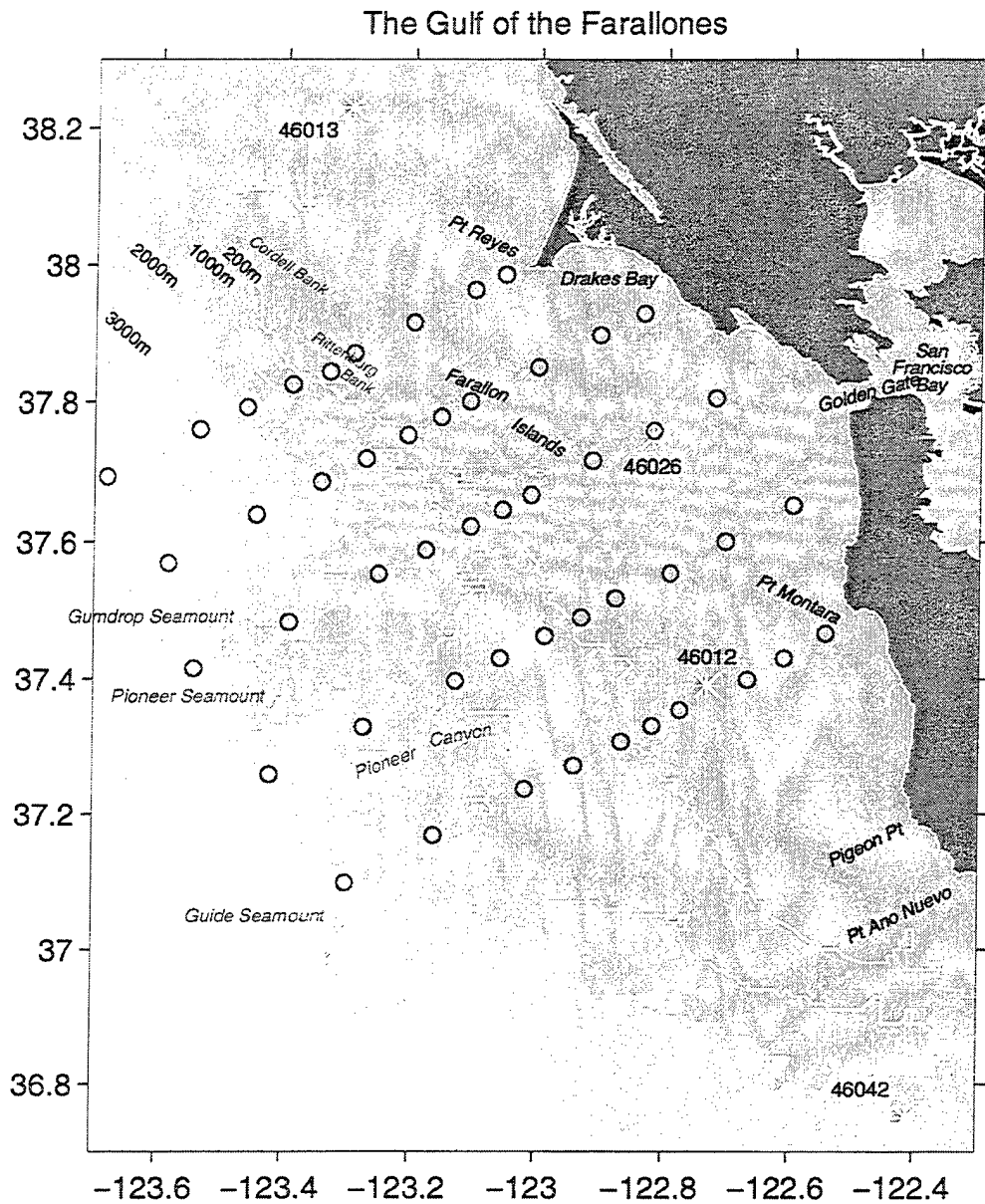


Figure 4.1 The Gulf of the Farallones. Locations of CTD stations for the Slope/Shelf Experiment are marked with open circles. National Data Buoy Center buoy mooring locations are indicated with asterisks. Bathymetry zones 0-200 m, -1000 m, -2000 m, -3000 m and >3000 m have gradually decreasing shading.

Average Velocity Relative to 500m

(a) CalCOFI Line 60 Average Velocity (relative to 500m)

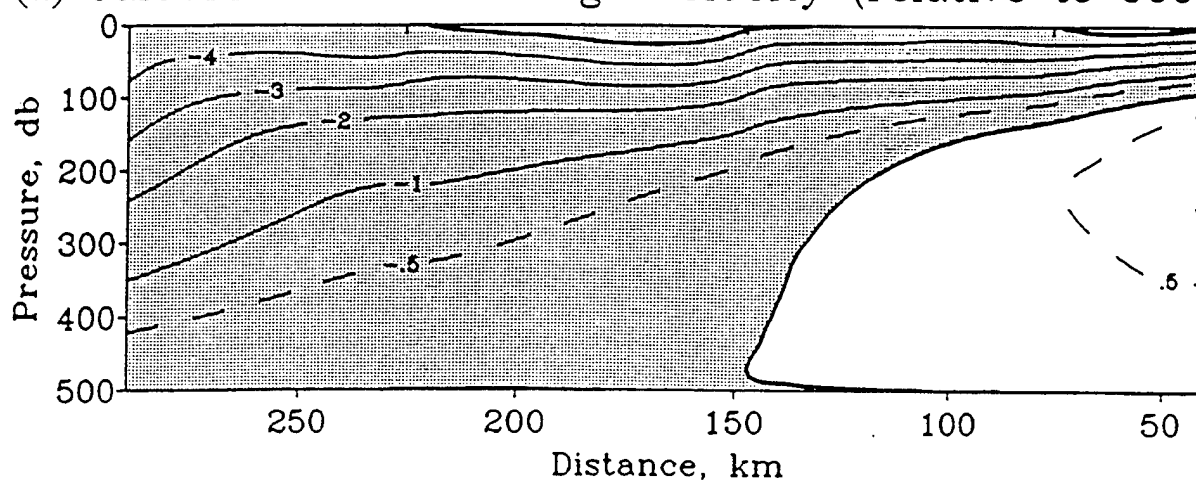


Figure 4.2 Geostrophic velocities relative to 500 m off Point Reyes. (From Bray and Greengrove, 1993.)

40 km from the coast, leaving the details of the shelf and upper slope flow and any mesoscale ($O(10\text{ km})$) features undefined. Additionally, their velocities only represent the geostrophic component of the flow and assume that 500 m depth (or the bottom if shallower) represents a level of no motion. Recent current meter observations over the slope have shown significant mean poleward flow ($>4\text{ cm/s}$) at 800 m depth and mean poleward flow of 1 cm/s at 1400 m depth (Kinoshita et al, 1992).

The continental shelf area of the Gulf has received even less attention, although it may have a more complex circulation pattern. Along most of the coast from Oregon to Point Conception, the continental shelf break is located within six to eight kilometers of shore; however, in the Gulf it widens to almost 50 km. The orientation of the coastline and the partial protection from northwesterly winds created by the seaward projection of Point Reyes may add to the complexity of the shelf circulation. Also, the Gulf is connected via the narrow channel of the Golden Gate with San Francisco Bay, and exchanges of waters with different temperatures and salinity occur (Largier, 1996) which add complexity to the density structure and circulation patterns. The continental slope is fairly steep and, although broken by several canyons and seamounts, reaches 3000 m depth within 20 to 50 km of the shelf break.

Schwing et al. (1991) examined hydrographic data collected from south of Monterey Bay to north of Point Reyes in May-June 1989 and found that equatorward currents were predominant in the upper 200 m, upon which numerous eddylike features ($O(10\text{ km})$) were superimposed. Upwelling-favorable winds strengthened and relaxed at 3-10 day intervals and upwelling occurred at discrete sites; somewhere north of Pt. Reyes, near Pt. Año Nuevo, and at Pt. Sur (south of Monterey Bay), producing alongshore and cross-shelf fronts. Identical

studies in subsequent years (cf. Sakuma et al., 1996) show this pattern is an annual occurrence.

Rosenfeld et al. (1994) expanded on the work of Schwing et al. (1991), concentrating on upwelling around Monterey Bay. They suggested the region oscillated between two states, an active upwelling state during equatorward winds and a relaxed state during periods of weak or poleward winds. During relaxation, a rapid onshore advection of warm offshore water was observed; when the prevailing upwelling-favorable winds returned, waters of the coastal region rapidly became cooler and more saline (though not necessarily in Monterey Bay where the orientation of the coast is not conducive to upwelling).

A synoptic ADCP and CTD survey of the Gulf and inner continental slope took place in August 1990 (Gezgin, 1991). The winds were anomalously poleward during the cruise. The currents over the shelf were poleward, with water entering the Gulf in the southwest and exiting near Point Reyes. Areas of stronger velocity ("jets") were found offshore of Point Reyes and between the Farallon Islands and Point Montara. The currents over the slope were offshore with a northward component.

Parker (1996) also examined springtime conditions in the region from Monterey Bay to north of Point Reyes, focusing on 10 m depth and along the $26.2 \sigma_\theta$ isopycnal. At 10 m depth, the mean velocity field calculated using ADCP data from May-June cruises in 1993, 1994, and 1995 had poleward velocities 20-30 cm/s over the slope about 60 km from the coast and mixed but generally equatorward flow over the shelf. A 50-km wide band of equatorward flow diverts offshore north of Point Reyes. Persistent filaments of upwelled water extending offshore and equatorward were found to be anchored to Point Reyes and

Point Año Nuevo (Pigeon Point). Several wind relaxations were observed, and each time the surface waters in the Gulf of the Farallones became fresher and warmer.

The mean currents found in time series representing all seasons (Appendix A, Table A1) from current meter moorings in the Gulf present a picture where mean currents are generally *equatorward* or onshore over the shelf and poleward over the slope (Figure 4.3). Moreover, the variability between moorings and even between different meters on the same mooring suggest mesoscale variability, both temporal or spatial. Also, the mean circulation from a linear least squares fit to observations from current meters and ADCPs in the Gulf is poleward over the slope and equatorward over the shelf (Figure 4.4).

Are the poleward currents found by Gezgin over the shelf in August a seasonal phenomena? Interestingly, Lynn and Simpson (1987) studied the seasonal variability of California Current System using the nearshore-poor CalCOFI hydrography to estimate geostrophic flow and found that the direction of the inshore flow off the Gulf of the Farallones *is* seasonal, but *poleward in winter* and *equatorward in summer*. It seems the flow near the coast inshore of the CalCOFI data either has characteristics different from the flow further offshore or there is a substantial ageostrophic component to the flow that is captured by the ADCP data but not dynamic height.

B. THE SLOPE/SHELF EXPERIMENT CRUISES

In 1991 and 1992, the Environmental Protection Agency and the Naval Facilities Engineering Command, Western Division, sponsored five cruises to study the general circulation of the shelf and slope region of the Gulf of the Farallones. The objective was to determine the likely dispersal of dredge spoils proposed to be deposited periodically in the

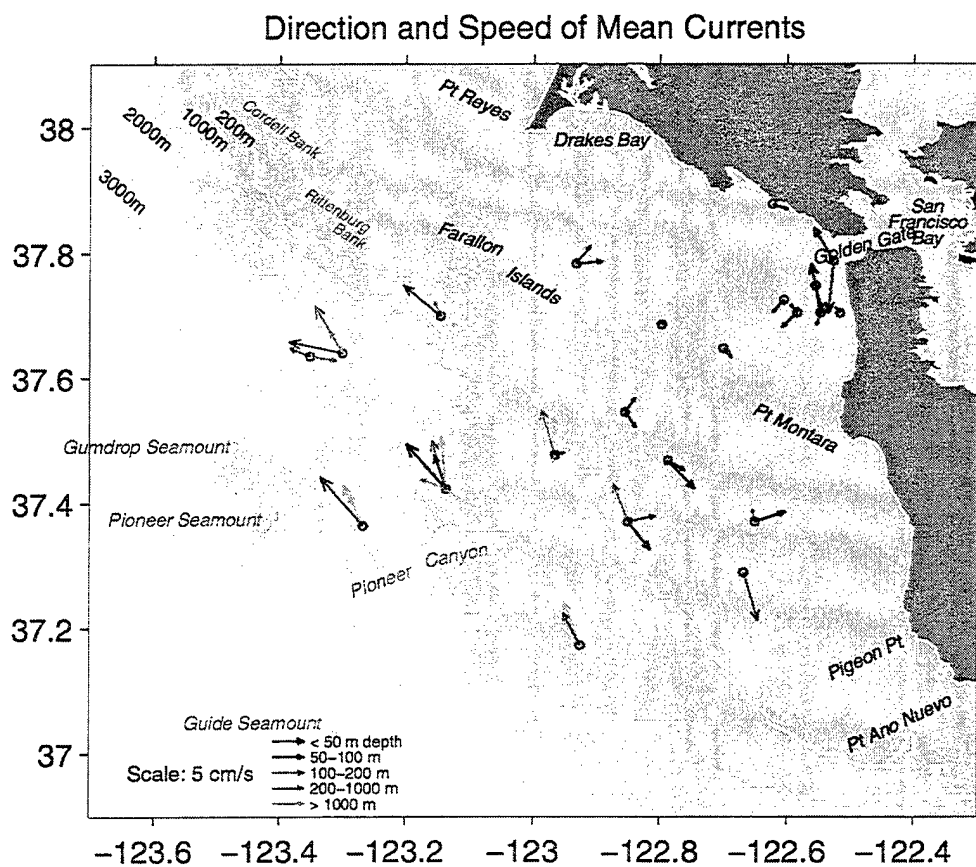


Figure 4.3 Direction and speed of mean currents calculated from all available current meter time series from the Gulf. Shade of vector indicates depth range of meter per the key in the lower left corner.

Mean Flow at 75m

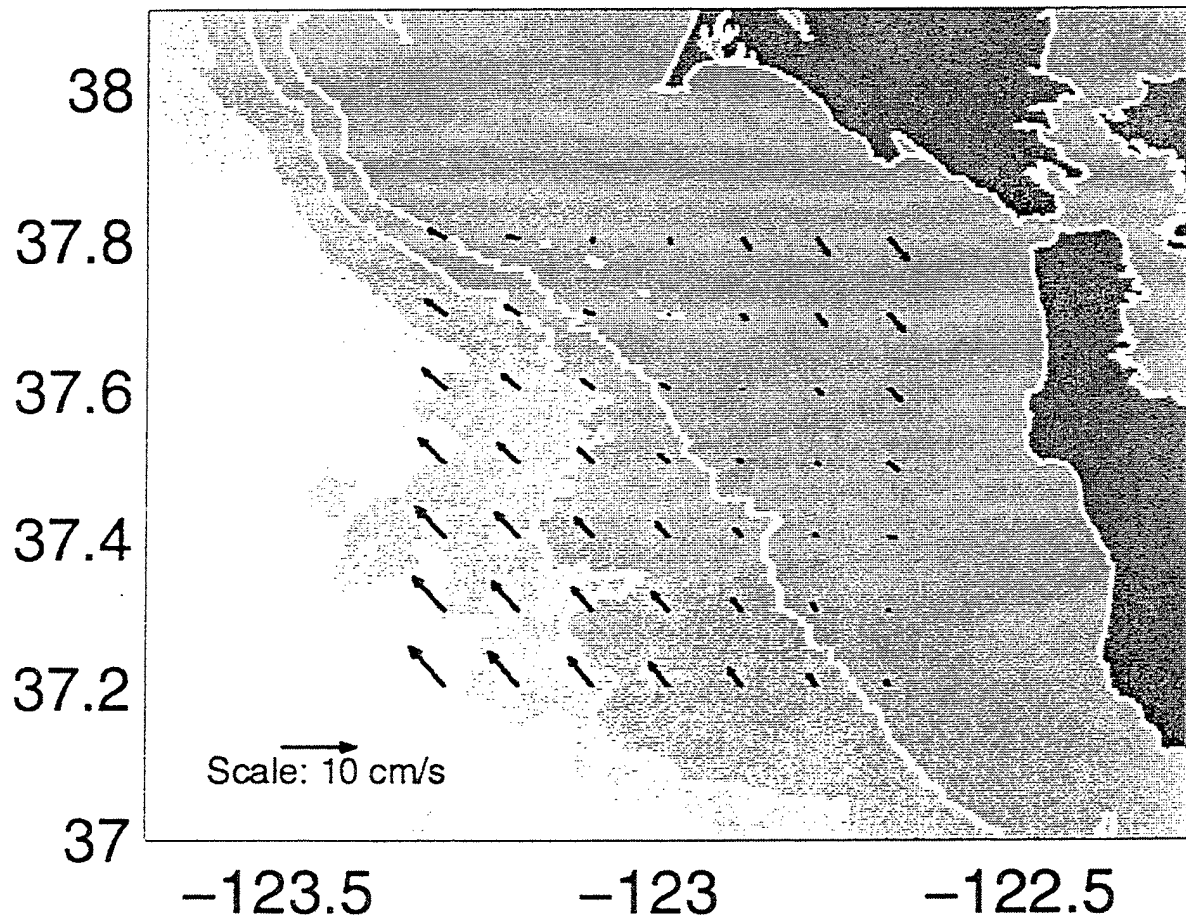


Figure 4.4 Mean flow at 75 m from an empirical model of the Gulf (Chapter III).

area. Cruises took place in February, May, August, and October/November 1991 and in February 1992.

CTD casts were made in a grid pattern that covered the Gulf from Pigeon Point to Point Reyes and seaward to the 3000 m isobath (Figure 4.1). The grid was occupied once each cruise, except that the northerly line was missed in the February 1992 cruise. Each CTD cast extended to within 25 m of the bottom. Details on the processing and summaries of CTD and ADCP data are available in a series of data reports (Jessen et al., 1992a-d; Rago et al., 1992). Spiciness was calculated for CTD data using the methods of Flament (1986). Density anomalies were computed using the Matlab SEAWATER package (Morgan, 1994). Geostrophic velocities were calculated using the method described in Pond and Pickard (1983). Geostrophic calculations in depths less than 500m were made by extending the deeper isopycnals inshore horizontally, per Reid and Mantyla (1976).

Acoustic Doppler Current Profiler (ADCP) observations were collected continuously while underway during each cruise. Data were saved in 8-meter depth bins from 15 meters to generally 400+ meters (depending on sea conditions and bottom depth). Post-processing, described in Jessen et al. (1992a-d) and Rago et al. (1992), yielded 15-minute averaged data. An empirical tidal model of the Gulf (Chapter III) was used to estimate the M_2 , S_2 , K_1 , and O_1 tidal velocities for the time, location, and depth of each ADCP data bin, which were then subtracted from the ADCP data.

ADCP and CTD data were gridded horizontally and vertically for contouring and transport calculations. Gridpoints were calculated by finding all data within a radial horizontal distance of the gridpoint ($1/10^\circ$ for horizontal grids, 8 km for vertical transections)

and calculating a distance-weighted average. Alongshore-averaged vertical transects using the distance of each ADCP ensemble from the 200-m isobath and depth as the coordinate system for gridding. The 200-m isobath is approximately the location of the "shelf break" where the isobathic gradient sharpens as the continental slope begins.

Satellite imagery during four of the five cruises was sufficiently cloud-free to estimate sea surface temperature (SST) for the Gulf region. SST was calculated using a two-infrared-channel algorithm as described in the cruise data reports.

C. REGIONAL WIND/SST CLIMATOLOGY AND CONDITIONS IN 1991-92

Daily alongshore winds and SST at four NOAA National Data Buoy Center buoys in or near the Gulf from January 1991 to March 1992 are shown in Figures 4.5 and 4.6 respectively (buoy locations are shown in Figure 4.1). Also shown are the annual cycles at each site, determined from biharmonic fits to the daily data between 1991 and 1996, the envelope within one standard error to the biharmonic fit, and the periods of each cruise. All the buoys are located 20-30 km offshore and all are located mid-shelf except buoy 46042, which is located in 500 m depth (Figure 4.1). It is evident that off central California buoy-to-buoy winds and SSTs are highly correlated.

The biharmonic fits to the winds in Figure 4.5 show an annual pattern of weak winds in December-February and strong equatorward winds in April-June. Nelson's (1977) monthly climatologies do not show poleward wind stresses at these latitudes, but the climatologies were calculated from observations collected primarily further offshore. The maximum winds in the harmonic fits occur in May, but are weaker in the Gulf (4 m/s) than north (7 m/s) and south (6 m/s) of the Gulf, possibly due to the partial lee created by Point Reyes. The standard

Alongshore Winds January 1991 – March 1992

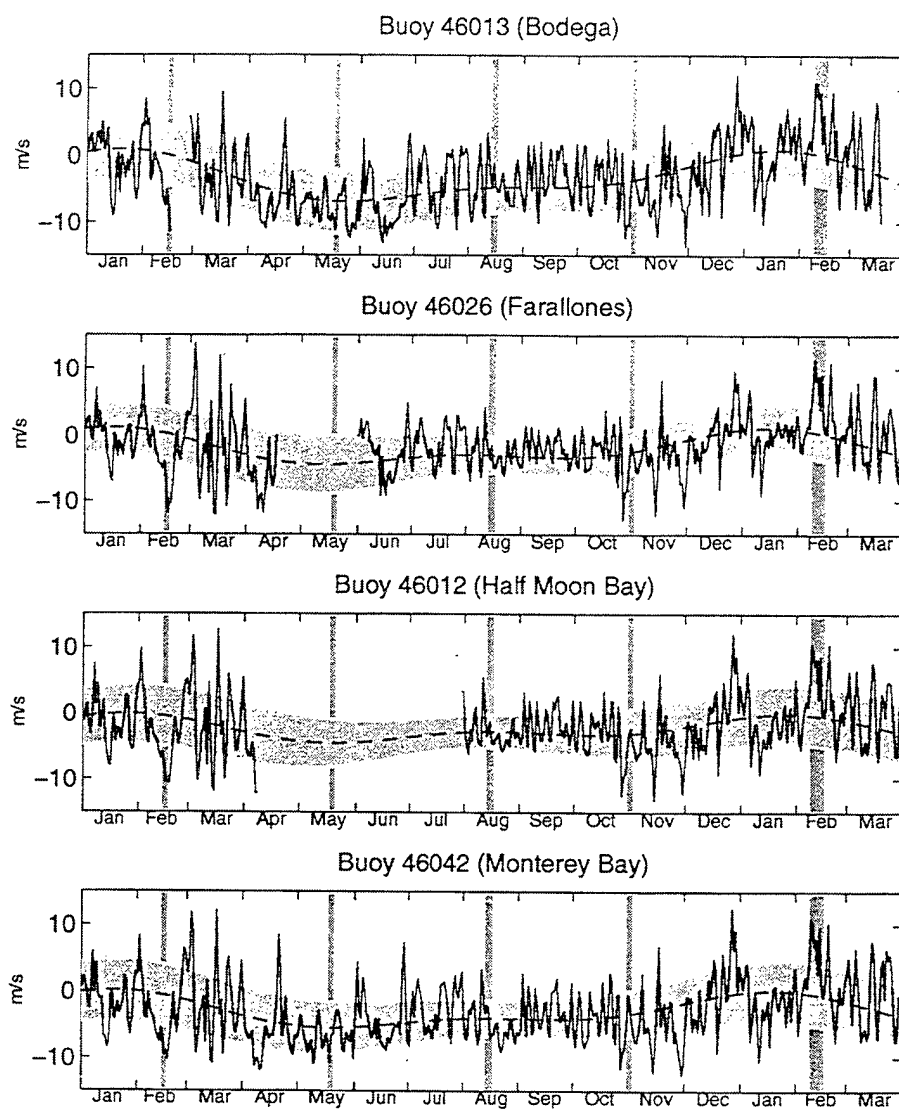


Figure 4.5 Alongshore winds at NDBC buoys a) 46013, b) 46026, c) 46012, and d) 46042 between January 1991 and March 1992. Dark line is daily winds. The dashed line is a biharmonic fit to daily winds from 1991-1996. Daily standard errors to the biharmonic fit were calculated, then fit to a biharmonic curve. The envelope between ± 1 standard error is shaded. Cruise periods are also indicated by vertical bands of shading.

error is fairly constant throughout the year north of the Gulf but higher in October-May (more storms) than in June-September at the other buoys. Week-to-week variability in the observations is as great as seasonal or interannual changes.

On seasonal scales, the winds in 1991 and the first three months of 1992 do not appear to be particularly anomalous when compared to other years. However, the winds prior to and during the individual surveys all show large deviations from the annual signal, and reflect the high variability typical of this region. The later part of the February 1991 cruise experienced substantially stronger than normal equatorward winds and the August cruise followed a day after a short period of anomalously poleward winds. The May and October cruises began with stronger than average equatorward winds that relaxed during the cruise. However, none of the cruises in 1991 seem to have taken place during extreme wind regimes compared to other events during the year. In February 1992, however, there were sustained strong poleward winds throughout the cruise period, the effects of which can be seen in the CTD, ADCP, and satellite SST data presented in Section E. Since the Gulf is not protected from southerly winds, operations had to be repeatedly suspended in February 1992 and only four of the five offshore transections were occupied. It will be shown that ocean circulation and structure appear linked to the recent local wind conditions in all five cruises.

Daily SST harmonics also follow an annual pattern, but unlike the wind the seasonal SST cycles are characterized by two maxima/minima (Figure 4.6). Highest temperatures in the Gulf (14.4°C) are in mid-September, and minimum temperatures (11.6°C at the Farallones buoy and 12.5°C at the Half Moon Bay buoy) are near the beginning of January, presumably in response to the annual solar cycle. After seasonal warming commences in late

SST January 1991 – March 1992

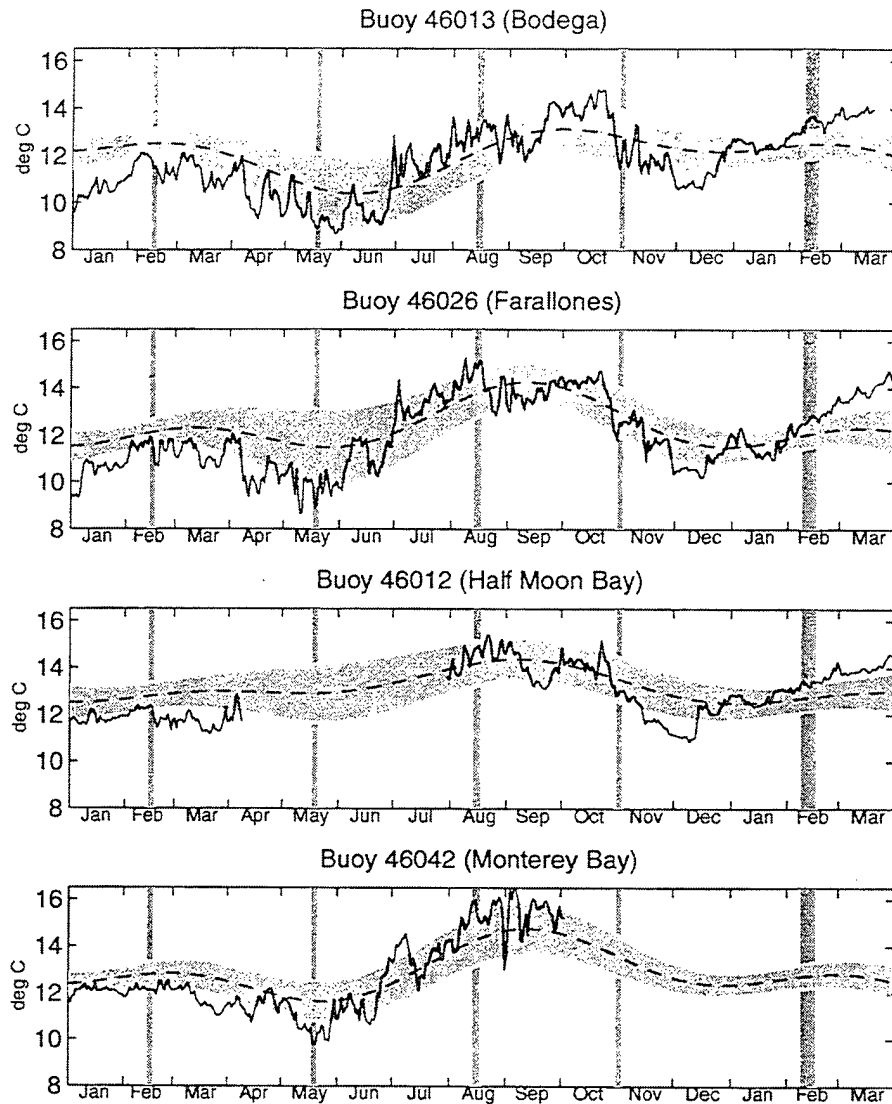


Figure 4.6 Sea surface temperature (SST) at NDBC buoys a) 46013, b) 46026, c) 46012, and d) 46042 between January 1991 and March 1992. Dark line is daily SST. The dashed line is a biharmonic fit to daily SST from 1991-1996. Daily standard errors to the biharmonic fit were calculated, then fit to a biharmonic curve. The envelope between +/- 1 standard error is shaded. Cruise periods are also indicated by vertical bands of shading.

winter, SSTs again decline, reaching the secondary minimum in mid-May. This is caused by coastal upwelling and mixing by the strong winds seen during this season. Outside the Gulf these second minima have lower temperatures than in the January minima. Buoy SSTs in the Gulf seem to be less affected by the onset of upwelling-favorable winds in spring.

SSTs were anomalously low throughout the January-June 1991 period, then near-normal until the end of January 1992. At this point, SST became anomalously warm into March 1992. The period of warming in 1992 followed a month after the initial warm signal of the 1992-93 ENSO (El Niño - Southern Oscillation) reached the eastern equatorial Pacific. This was further explored by Ramp et al. (1997), who speculate the changes in the Gulf were related to the propagation of a Kelvin wave combined with anomalies in local forcing associated with the ENSO event.

D. VERTICAL SECTIONS OF TEMPERATURES AND SALINITIES IN 1991-92

Alongshore-averaged vertical sections of temperature and salinity were created as described in section B (Figures 4.7-11). Averaging alongshore can be justified as there is generally more cross-shore than alongshore variability and eases interpretation and presentation. However, as will be described in section E, there are features such as intrusions of California Current water from offshore that are not symmetric alongshore.

In February 1991 (Figure 4.7) temperatures over the slope varied from 8-11°C and salinities varied from S=33.4-34.0. Isopycnals were nearly horizontal, leading to weak geostrophic currents (Figure 4.12, computed using alongshore-averaged temperatures and salinities). By May (Figure 4.8), the strong upwelling-favorable winds typical of the season had filled the Gulf with cooler and more saline water (7.5-9.5°C, S=33.5-34.05). Isopycnals

Alongshore-Averaged Temperature and Salinity – Feb 13–18, 1991

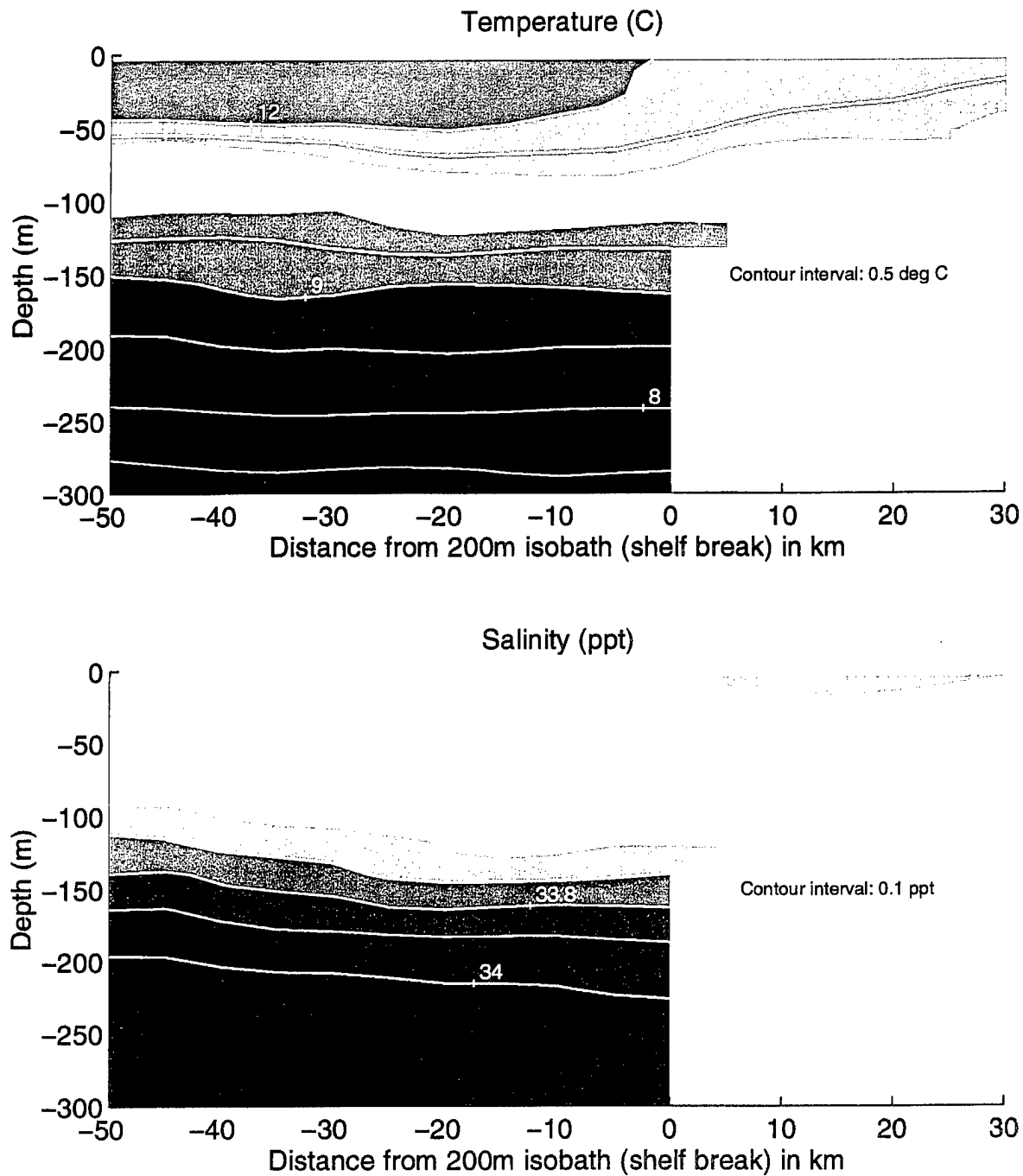


Figure 4.7 Alongshore-averaged temperature (top) and salinity (bottom) from CTD data from the February 13-18, 1991, SSE cruise.

Alongshore-Averaged Temperature and Salinity – May 16–21, 1991

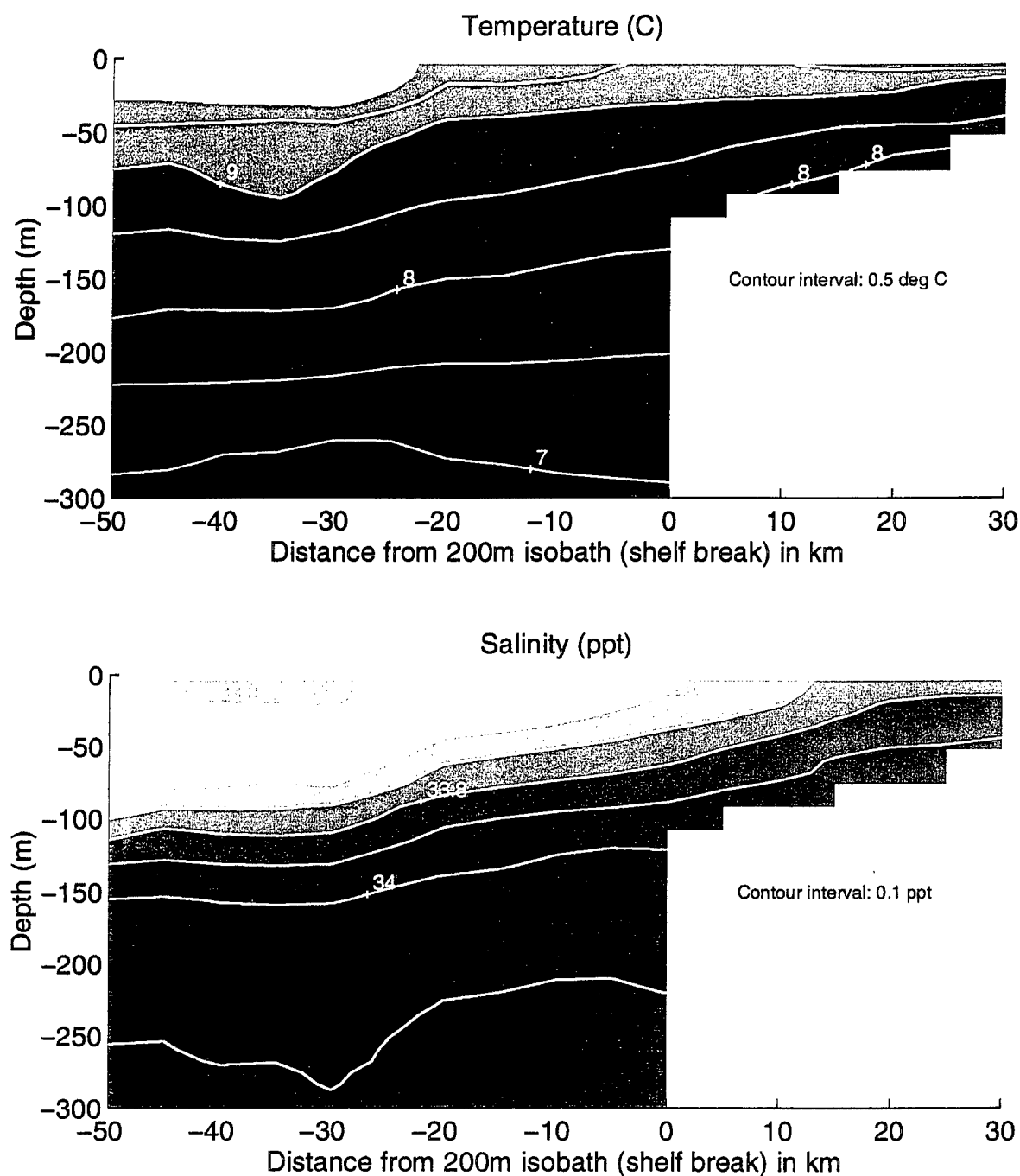


Figure 4.8 Alongshore-averaged temperature (top) and salinity (bottom) from CTD data from the May 16-21, 1991, SSE cruise.

were tilted upward towards the coast, and the geostrophic currents may have been carrying some of the cooler, saltier water from the north (Figure 4.12). In August (Figure 4.9), 50-200 m temperatures ($8-11^{\circ}\text{C}$) and salinity ($S=33.4-34.0$) were similar to those seen in February. Isopycnals below 100 were sloped steeply downwards toward the coast, balancing poleward geostrophic currents (Figure 4.12). By October (Figure 4.10), temperatures were slightly higher ($8.5-11^{\circ}\text{C}$) at 200 m but salinity remained at $S=33.4-34.0$ and isopycnals were nearly horizontal. Under the light mean wind conditions usually found November-February, the hydrography should have changed little through the following February. However, as discussed in Section III, ENSO started in the interim, changing the basin-scale distribution of water characteristics. February 1992 also featured unusually strong poleward winds. Temperatures (between 50-200 m) soared to $9-13^{\circ}\text{C}$ while salinity dropped somewhat ($S=33.25-33.9$) (Figure 4.11). Geostrophic currents were strongly poleward in balance with isopycnals sloped steeply downwards towards the coast (Figure 4.12).

There was greater horizontal variability in the hydrography of the upper 50 m relative to the deeper waters. Except for San Francisco Bay outflow, warmer and fresher waters were always offshore (the lens of fresher water at the surface in the alongshore-average for February 1991 is caused by a tongue of low-salinity water emanating from San Francisco Bay and crossing survey line B (Jessen et al., 1992a, Figure 8)). Near-surface waters in February 1991 were $\sim 12^{\circ}\text{C}$; cooled in May to $\sim 9.5^{\circ}\text{C}$ (upwelling); then warmed in August to $\sim 15^{\circ}\text{C}$ with summer solar heating and lighter winds; and cooled during the Fall to $\sim 13^{\circ}\text{C}$ by the end of October. Near-surface salinities remained $S=33.3-33.4$ except during the May season when salinities from $S=33.2-33.9$ were found.

Alongshore-Averaged Temperature and Salinity – Aug 12–18, 1991

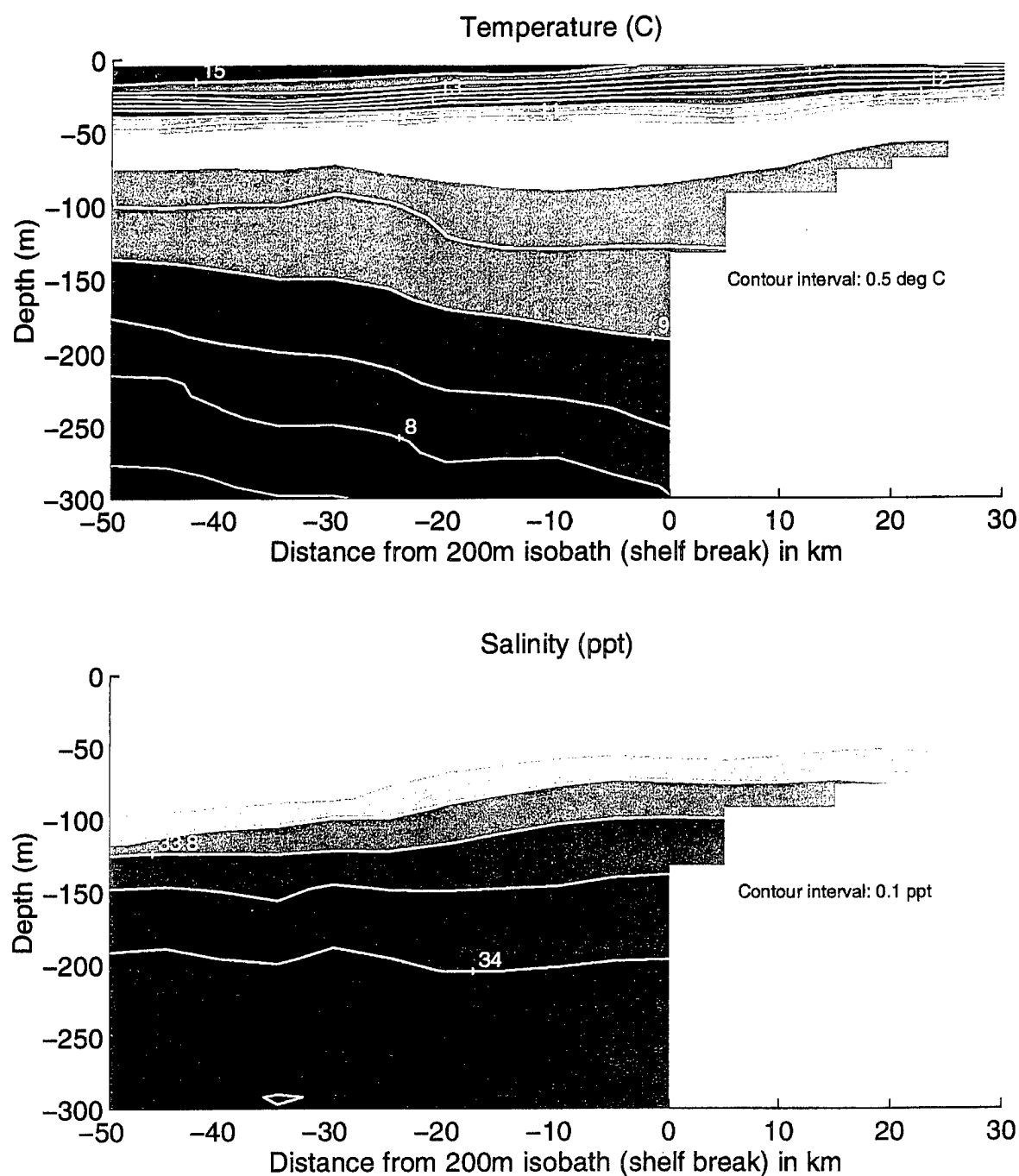


Figure 4.9 Alongshore-averaged temperature (top) and salinity (bottom) from CTD data from the August 12-18, 1991, SSE cruise.

Alongshore-Averaged Temperature and Salinity – Oct 29–Nov 3 '91

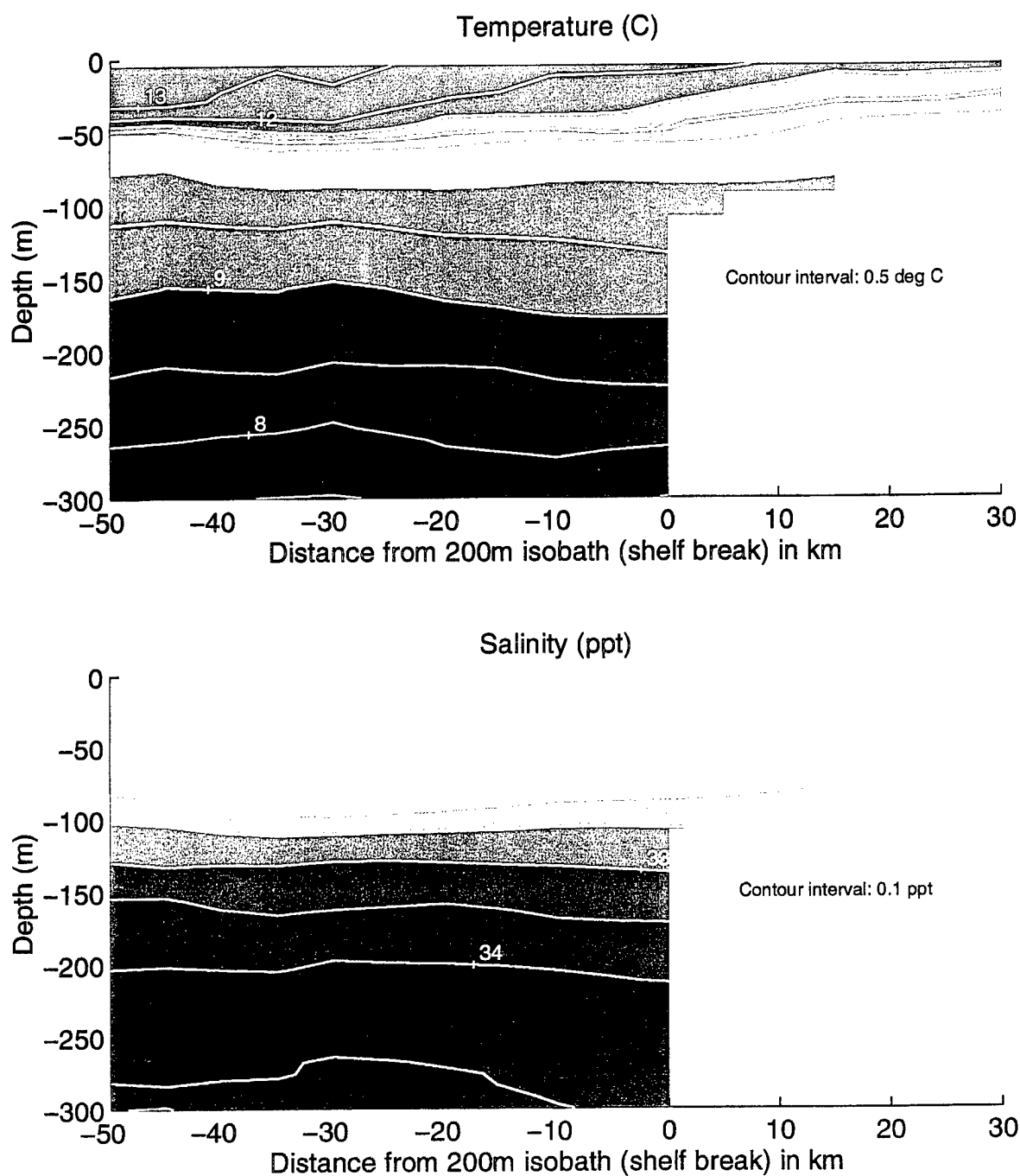


Figure 4.10 Alongshore-averaged temperature (top) and salinity (bottom) from CTD data from the October 29 - November 3, 1991, SSE cruise.

Alongshore-Averaged Temperature and Salinity – Feb 7–17, 1992

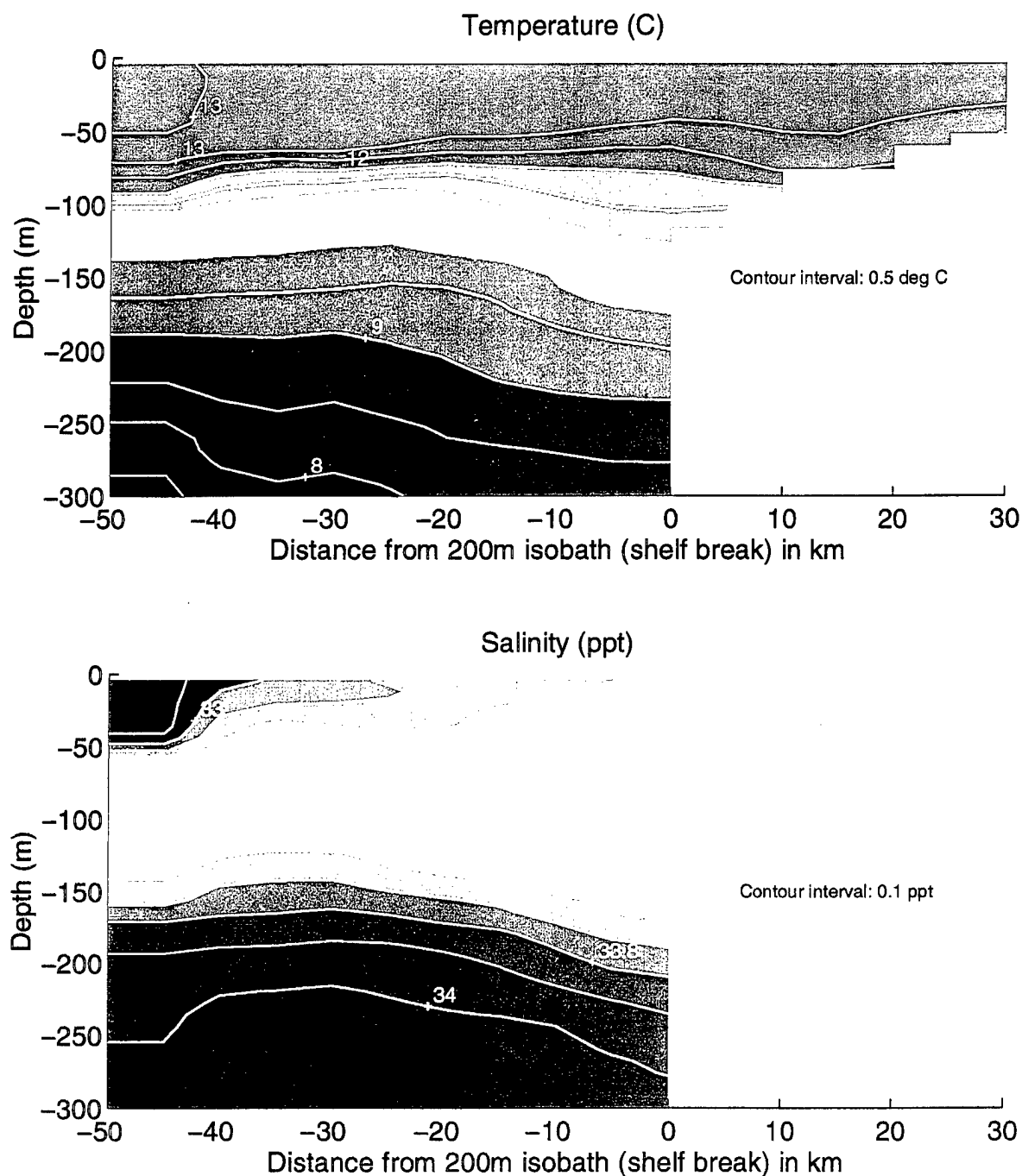


Figure 4.11 Alongshore-averaged temperature (top) and salinity (bottom) from CTD data from the February 7-17, 1992, SSE cruise.

Geostrophic Velocity Relative to 500 db

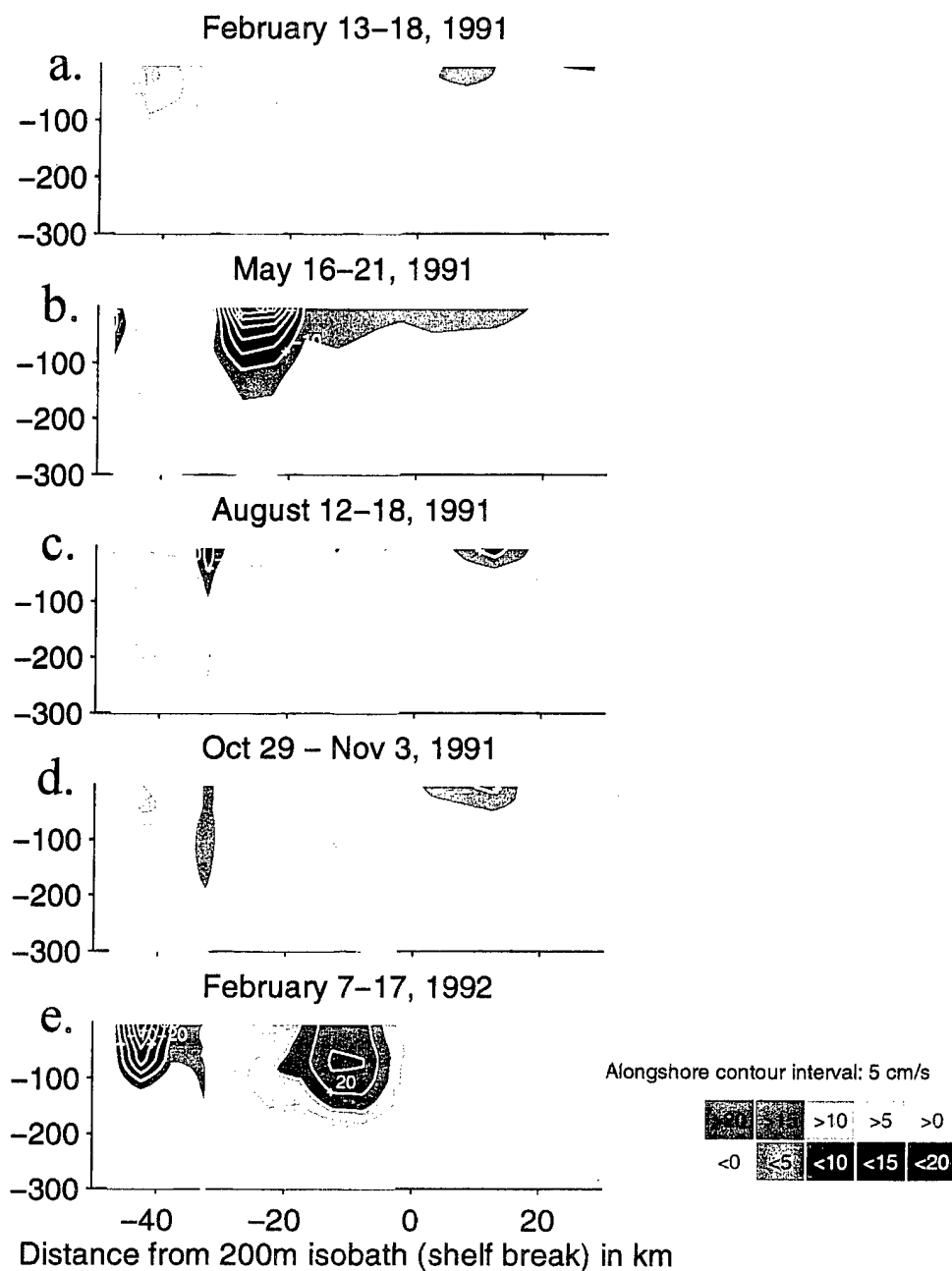


Figure 4.12 Alongshore-averaged geostrophic velocities relative to 500 db. a) February 13-18, 1991. b) May 16-21, 1991. c) August 12-18, 1991. d) October 29 - November 3, 1991. e) February 7-17, 1992.

E. ADCP AND CTD FIELDS

Horizontal velocity plots for 15-23 m and 95-103 m depth bins and an alongshore-averaged vertical section of velocity are presented for each cruise (Figures 4.13, 15, 17, 19, 23). Mean velocities for the four 1991 cruises are presented in Figure 4.21. Conditions at 15-23 m are representative of the near-surface and for clarity will be referred to as such in this section.

1. February 13-18, 1991

Poleward flow is evident over the continental slope and equatorward flow is present over much of the continental shelf (Figure 4.13). Throughout the Gulf, regions of higher velocity ("jets") are contiguous with regions of lower velocity, producing considerable convergence and divergence in horizontal flow. Although there is a general decrease in speed with depth to 5-10 cm/s at 300 m depth, the direction of flow does not generally change with depth.

Nearshore, water enters the Gulf from the north near Pt. Reyes (Figure 4.13a). This jet (40+ cm/s) contains relatively cool, salty water (Figure 4.14a,b), which may have been upwelled further north and advected by the equatorward shelf current typically found between Pt. Arena and Pt. Reyes (Huyer and Kosro, 1987). The jet decelerates after entering the Gulf and meanders southward with speeds ~10-15 cm/s. Part of this flow appears to recirculate cyclonically over the shelf into Drake's Bay. However, most diverges and joins the poleward flow offshore. The temperature and salinity characteristics of this portion of the flow are highly variable (Figure 4.14). The remaining equatorward shelf flow accelerates as it nears Pigeon Point and exits the Gulf in the south.

ADCP Velocities February 13–18, 1991

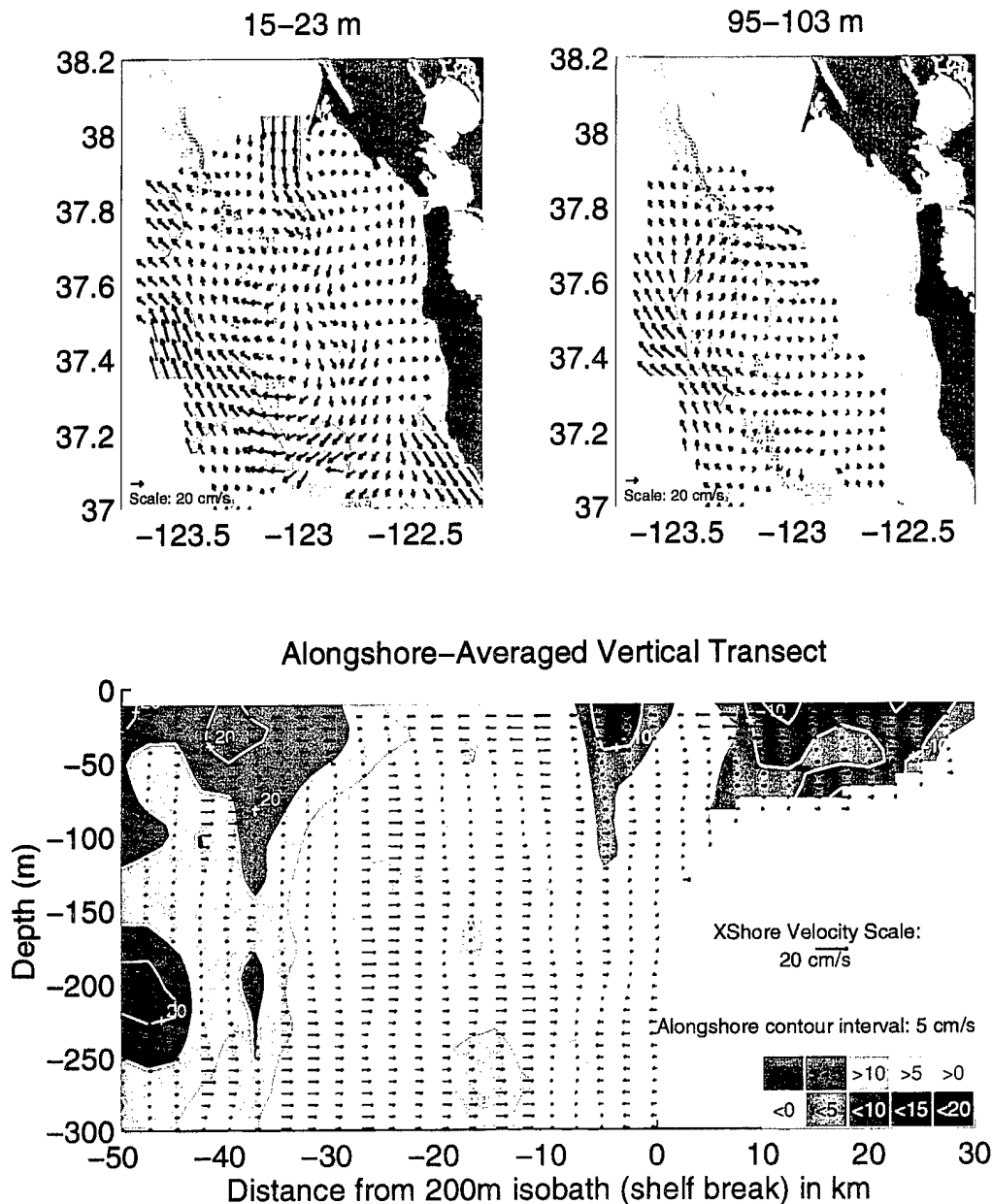


Figure 4.13 ADCP velocities, February 13–18, 1991. a) $.05^\circ \times .05^\circ$ horizontal grid of ADCP velocities in the 15–23 m depth bin. Regions of speeds greater than 15 cm/s are shaded to highlight the jets. Bathymetry is the same as for Figure 1. b) Same as (a) except velocity bin is 95–103 m. c) Alongshore-averaged vertical transect on a 8 m depth by 2.5 km grid. Alongshore currents are fill-contoured. Contours are labeled. Cross-shore currents are plotted as scaled vector arrows.

Temperature and Salinity – February 13–18, 1991

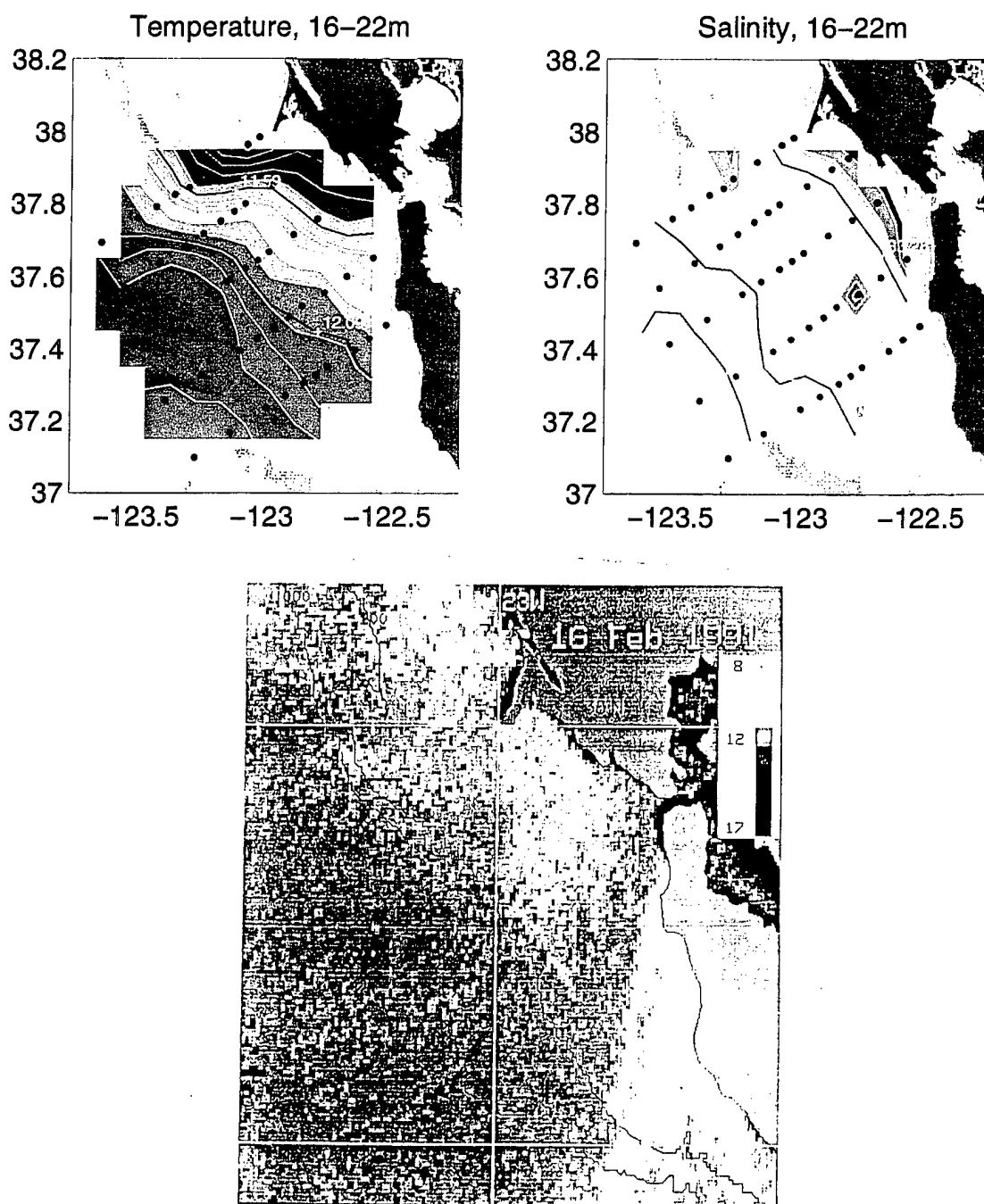


Figure 4.14 Water mass characteristics, February 13–18, 1991. a) Temperature at 16–22 m depth. CTD station positions are indicated by small open circles. b) Salinity at 16–22 m depth. c) Satellite SST image for February 16, 1991. Color schemes scaled for this cruise.

A satellite SST image from February 16 (Figure 4.14c) shows the wedge of cool water entering the Gulf from the north. Most of the cool water remains near the coast and fills at least the northern portion of the shelf in the Gulf (the southern portion of the region is obscured by cloud cover), but cool filaments extend offshore seaward of Point Reyes and Point Montara. The Point Montara filament may be the SST manifestation of the offshore flow seen over the shelf in the ADCP data.

Flow over the slope is poleward with maximum velocities >40 cm/s is found 40+ km offshore of the shelf break. The poleward flow entering the region from the south is relatively warm and salty, associated with a higher concentration of Equatorial Pacific water (Lynn and Simpson, 1987).

The offshore flow is limited to the upper 50 m (Figure 4.14c). Below 50 m depth, flow is onshore. This pattern conforms to the classic model of Ekman circulation during upwelling-favorable winds, where the surface waters along the coast are pushed offshore and water beneath the Ekman layer water moves horizontally onshore and rises to replace the surface water diverging from the coast..

2. May 16-21, 1991

The flow regime is quite different in May. There is no equatorward shelf jet off Point Reyes (Figure 4.15a), although hydrography (Figures 4.16a,b) shows cool, saline water, probably recently upwelled, stretching across the shelf off Point Reyes and southward. Near the Farallon Islands, cool, saline water extends in two tongues, one along the coast and a larger one offshore. As the offshore tongue moves to the southwest it accelerates to >40

ADCP Velocities May 16-21, 1991

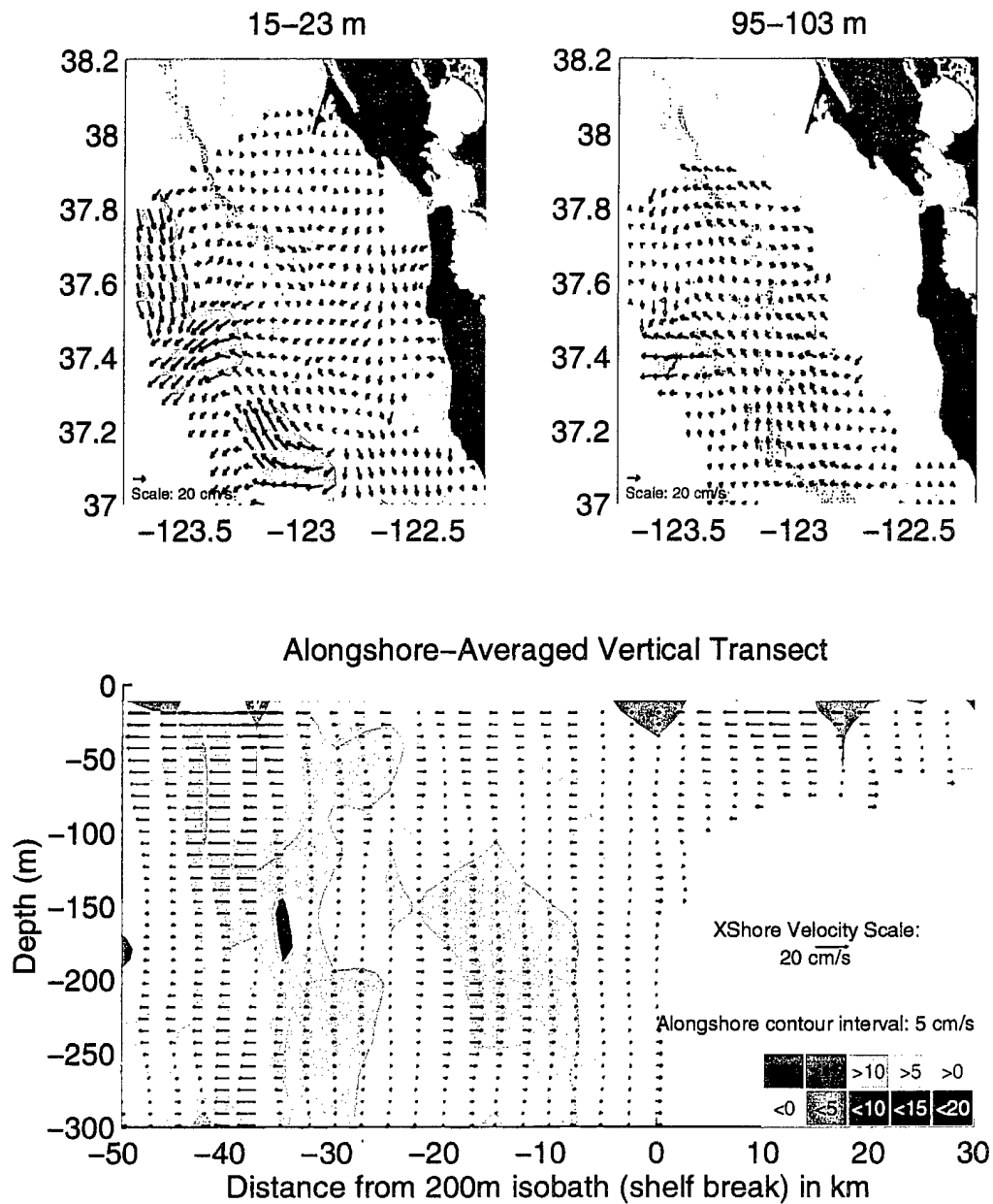


Figure 4.15 ADCP velocities, May 16-21, 1991. Otherwise same as Figure 4.13.

Temperature and Salinity – May 16–21, 1991

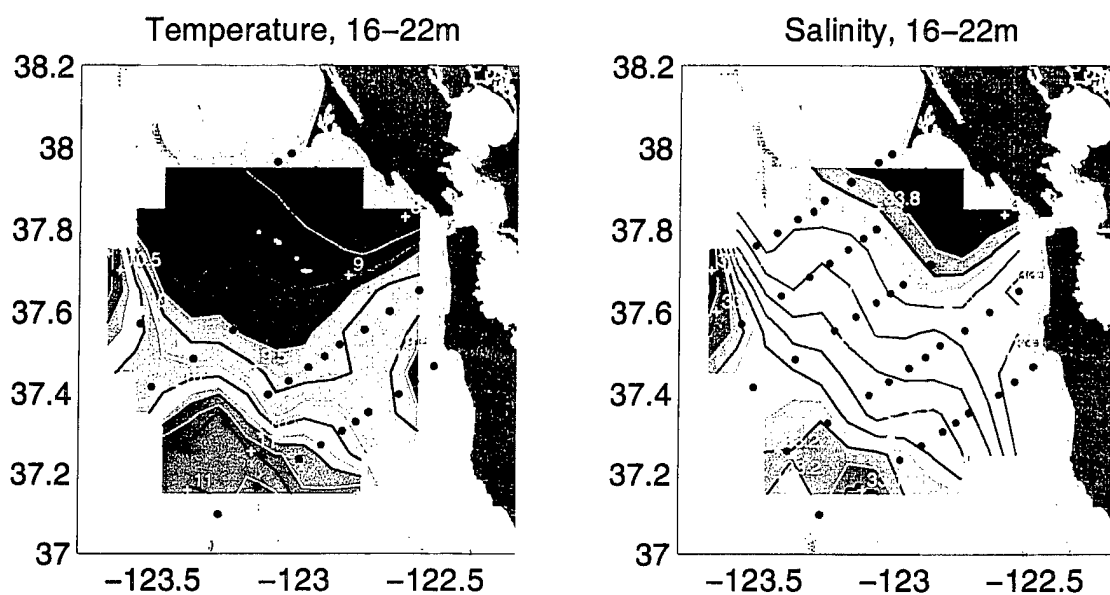


Figure 4.16 Water mass characteristics, May 16–21, 1991. c) Satellite SST image for May 15, 1991. Otherwise same as Figure 4.14.

cm/s. Warm, fresher water converges onto this tongue from both the north and south, with velocities also >40 cm/s.

A satellite SST image captured just before the start of the cruise on May 15 (Figure 4.16c) reveals that the cool (salty) water is part of a large plume of upwelled water extending from north of Point Reyes into and through the Gulf. The plume of upwelled water warms with distance from its source, but bifurcates in the Gulf and extends southeastward and southwestward, as seen in the hydrography. The warm, fresher water appears to be associated with California Current water extending into the Gulf.

The flow is more baroclinic in May than February (cf. Figures 4.15a and b), although Figure 4.15c does not show this well since it averages the opposing surface poleward (in the south) and equatorward (in the north) slope flow. At 100 m, the flow over the slope is generally poleward although weak and meandering (Figure 4.15b). The offshore flowing tongue is still fairly strong but the equatorward jet in the north is barely evident.

During this season upwelling-favorable winds are greatest (Figure 4.5), and the effect on the water mass characteristics is marked. At 20 m depth, the whole region is $2-3^{\circ}\text{C}$ cooler and $S=.1-.5$ more saline (Figures 4.16a,b) than in February. Even at 200 m depth, waters are nearly 1°C cooler and $S=.05-.1$ saltier due to the uplifting of isopycnal surfaces (Figure 4.8). As seen during the upwelling conditions of February, cross-shore velocities (Figure 4.15c) are offshore in the surface Ekman layer and variable below.

3. August 12-18, 1991

Strong poleward flow with an onshore component dominates the region from the shelf break out to the limit of the observations. Unlike in February and May, flow is greatest at

100 m depth rather than at the surface (Figures 4.17a,b,c). There is a strong core of 20-40 cm/s poleward flow between 50-200 m and 20-40 km offshore of the shelf break. The core of the poleward flow is closer to the shelf than seen in February. Unlike May, the poleward slope flow originates south of the Gulf and travels uninterrupted through the region although, as seen in the previous two seasons, there is cross-shelf flow in the south that exceeds 10 cm/s in some areas. The relatively warm and salty flow closely follows the 1000 m isobath through the region. There is a strong cross-shore gradient in temperature and salinity, with fresher California Current water offshore (Figure 4.18). Maximum velocities are found along the axis of the steepest gradients in water mass characteristics.

As in February, water enters the Gulf from north of Point Reyes over the shelf and exits in the south near Pigeon Point. In between, the onshore flow bifurcates as it approaches Point Montara and flows northward and southward along the coast. Surface temperatures are 11.5-13°C over the shelf (and greater than 15°C offshore), a large change from the 8.5-9.5°C shelf temperatures seen in May. Buoy observations (Figure 4.6) suggests conditions were warmer than normal. Water is also fresher over the inner shelf than in May. As in May, cooler temperatures are located off the coast from Point Montara to Pigeon Point, suggesting that this location may be a center of upwelling. Unfortunately, no satellite imagery was available for several weeks before or after the cruise due to pervasive cloud cover.

4. October 29 - November 3, 1991

The circulation in October/November is complex and best introduced by describing the SST patterns in a satellite image captured during the cruise on November 2 (Figure 4.20c). Recently upwelled water bifurcates offshore of Point Reyes, with one portion

ADCP Velocities August 12–18, 1991

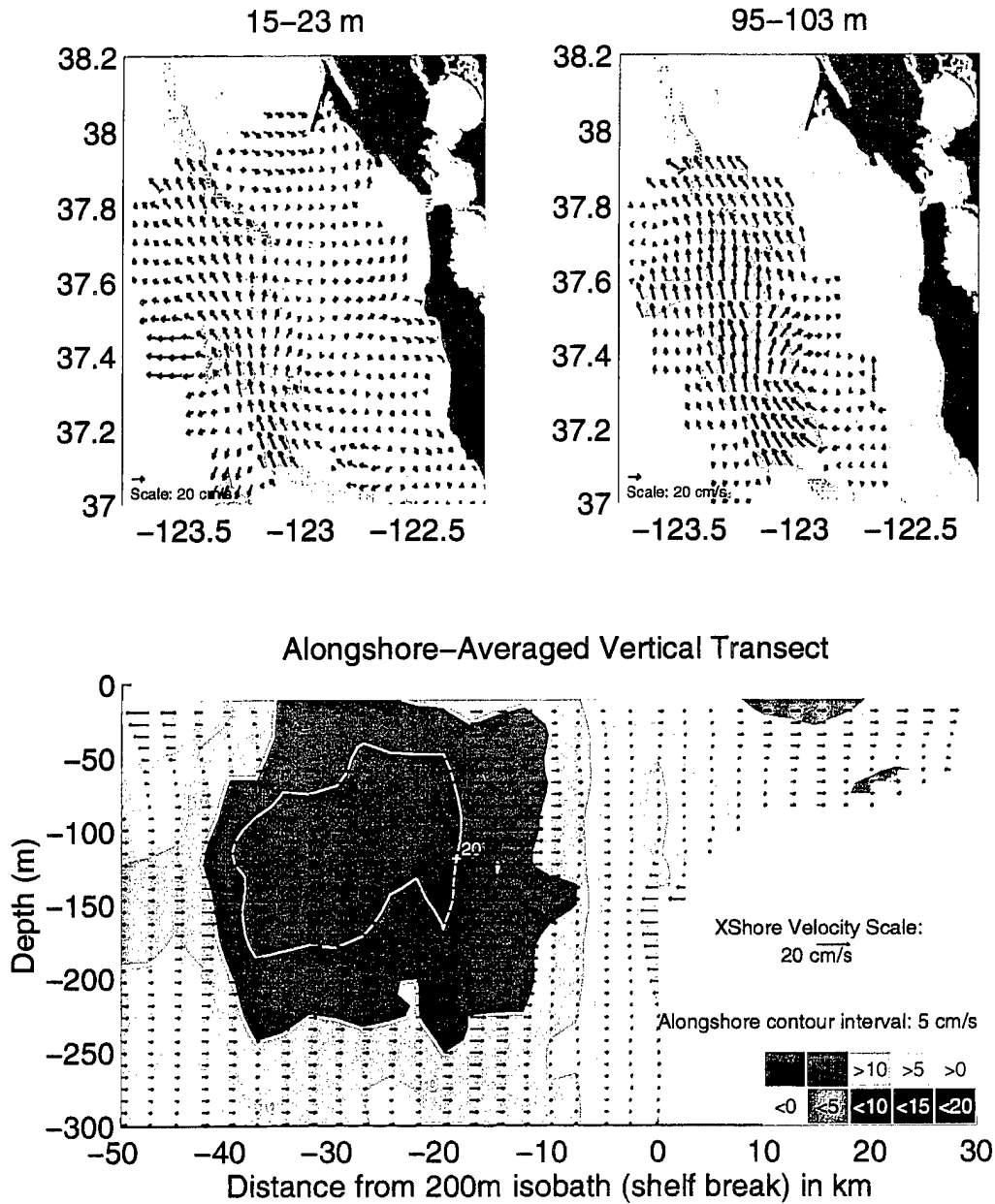


Figure 4.17 ADCP velocities, August 12–18, 1991. Otherwise same as Figure 4.13.

Temperature and Salinity – August 12–18, 1991

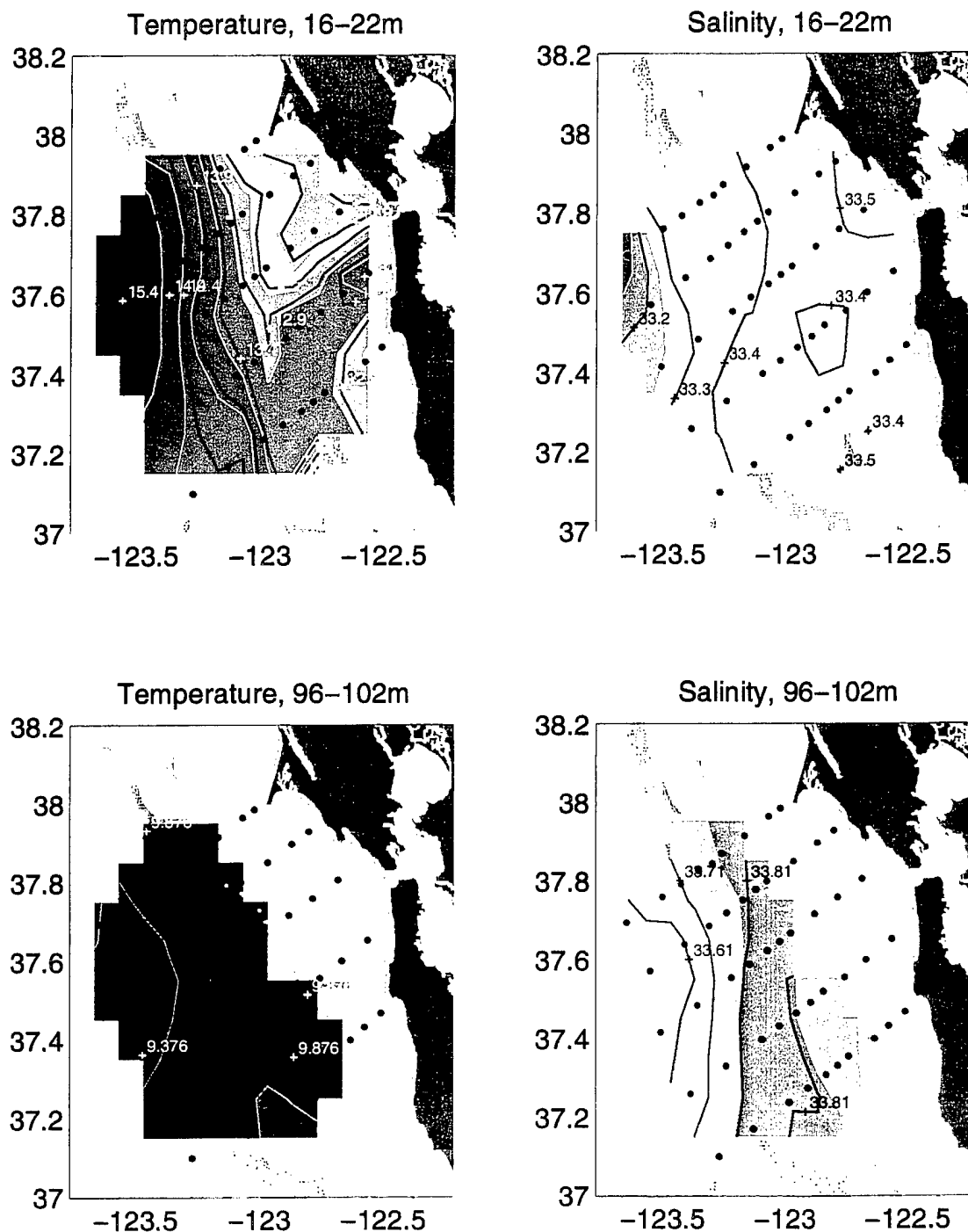


Figure 4.18 Water mass characteristics, August 12–18, 1991. Color schemes scaled for this cruise. a) Temperature at 16–22 m depth. CTD station positions are indicated by small black circles. b) Salinity at 16–22 m depth. c) Temperature at 96–102 m depth. CTD station positions are indicated by small open circles. d) Salinity at 96–102 m depth.

ADCP Velocities October 29 – November 3, 1991

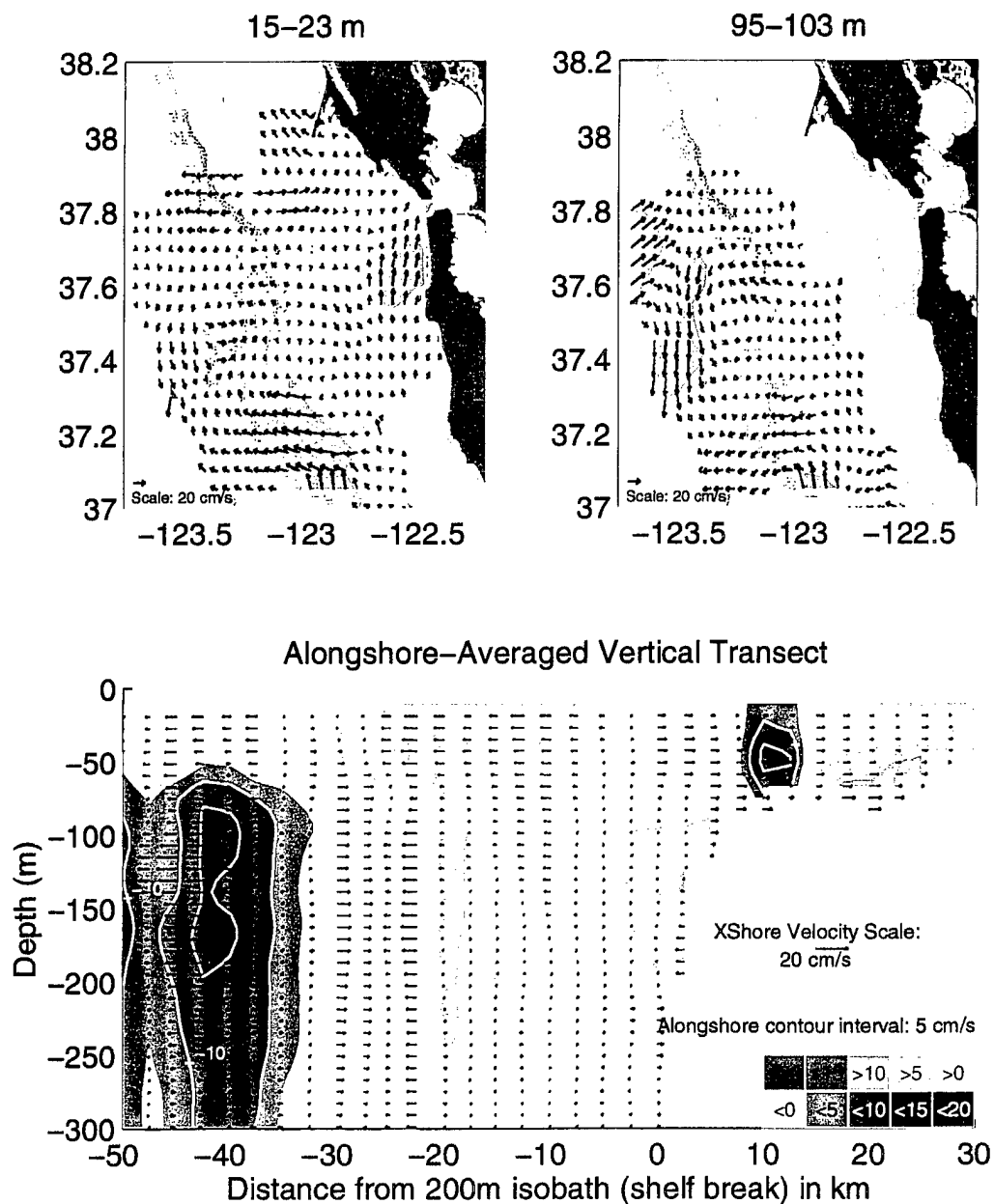


Figure 4.19 ADCP velocities, October 29 - November 3, 1991. Otherwise same as Figure 4.13.

Temperature and Salinity – Oct 29–Nov 3, 1991

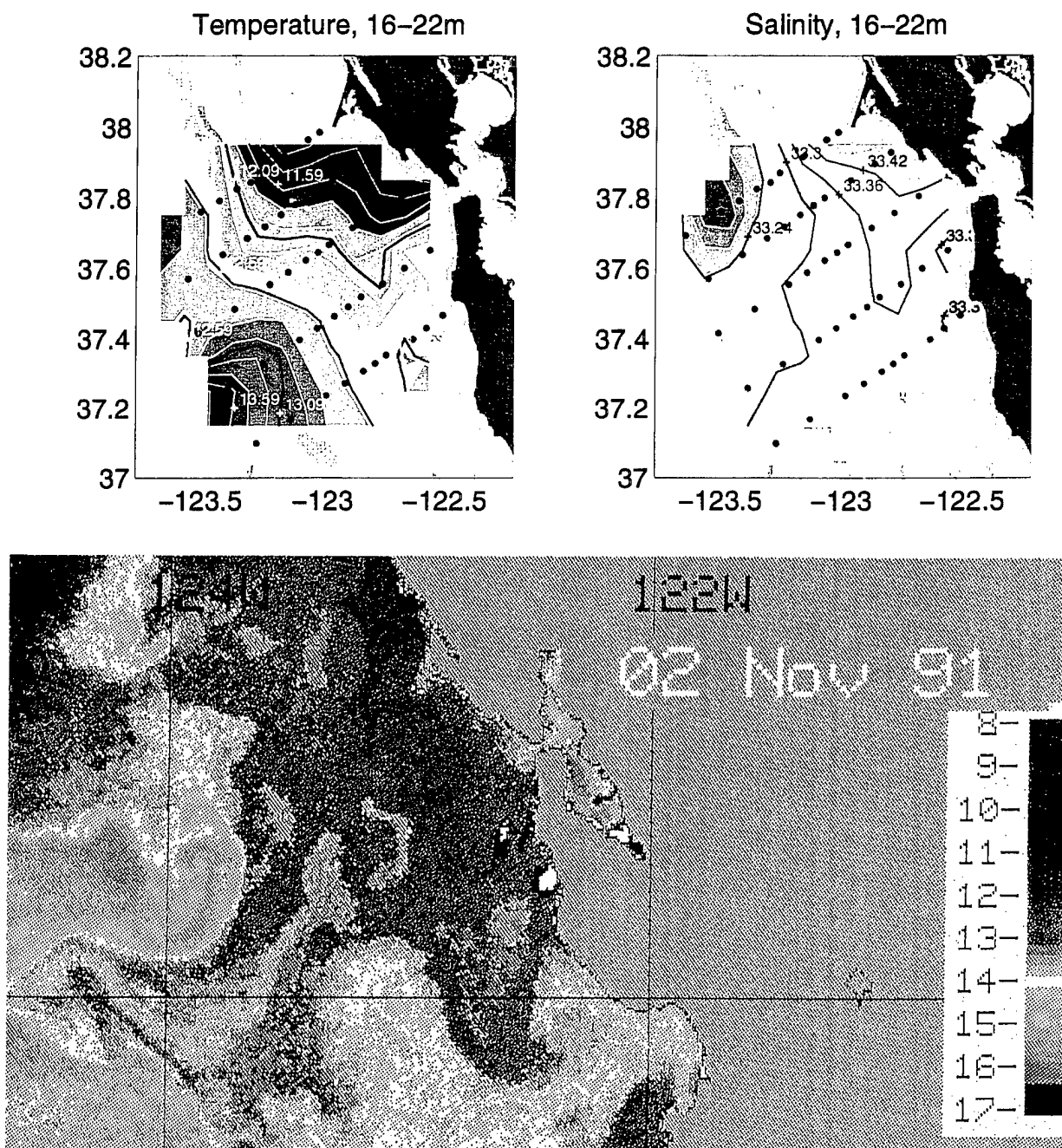


Figure 4.20 Water mass characteristics, October 29 - November 3, 1991. c) Satellite SST image for November 2, 1991. Otherwise same as Figure 4.14.

extending south offshore of the Gulf, and another east into the Gulf before turning towards the southeast. The high degree of mesoscale variability suggests $O(10\text{ km})$.scale eddies that vary in time and location.

As in the other cruises, the strongest poleward flow is seen over the slope at the surface, entering the Gulf from the south. Unlike every other season in 1991, however, poleward shelf flow is also seen over the southern region. The poleward coastal current between Point Montara and the Golden Gate, seen every season except May, is especially strong.

Temperatures are cooler in the top 100 m (Figure 4.22a) than in August, but unchanged in the deeper water (not shown). Salinity is slightly less ($\sim S=.1$) throughout the water column. Cross-shore velocities are onshore over the shelf and offshore in the top 50 m over the slope (Figure 4.19c).

5. 1991 Mean

In the mean, meandering poleward flow of 5-10 cm/s (in the alongshore average) is seen over most of the slope. Inshore, flow enters the Gulf from the north near Point Reyes and exits near Pigeon Point. Equatorward flow in the alongshore mean is $<5\text{ cm/s}$ (Figure 4.21c). In the southern region of the shelf some of the equatorward flow moves offshore and merges with the poleward flow over the slope (Figures 4.21a,b), entering the outer Gulf from the south and exiting to the north. Cross-shore flows are very weak over the shelf; over the slope they are offshore in the top 50 m and mostly onshore below.

Nearsurface waters are coolest and most saline near the coast and become fresher and warmer offshore (Figure 4.22a). Surface temperatures are $\sim 1^\circ$ warmer offshore than over

ADCP Velocities – Mean of Cruises in 1991

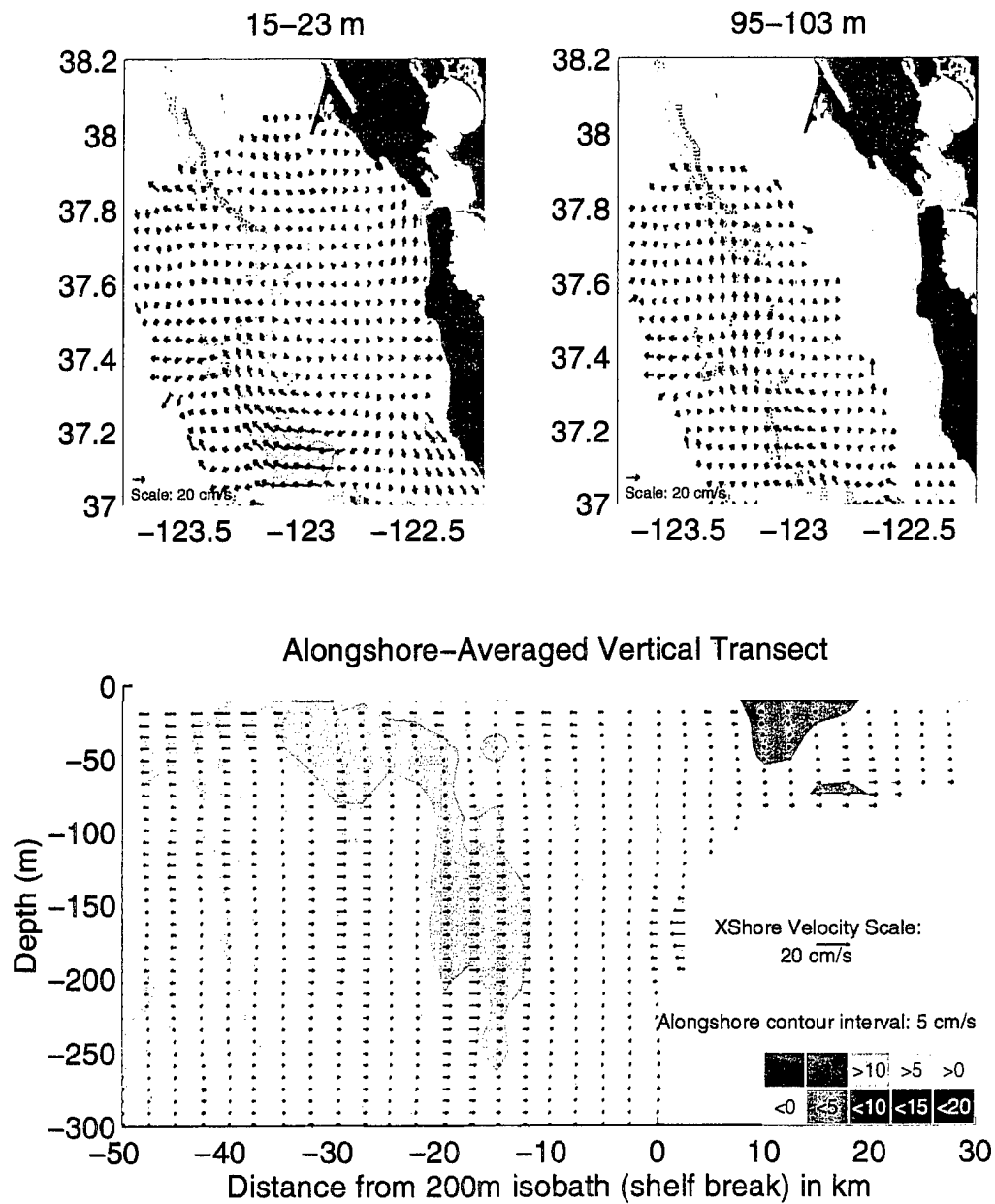


Figure 4.21 ADCP velocities, mean of four cruises in 1991. Otherwise same as Figure 4.13.

Temperature and Salinity – Mean of Cruises in 1991

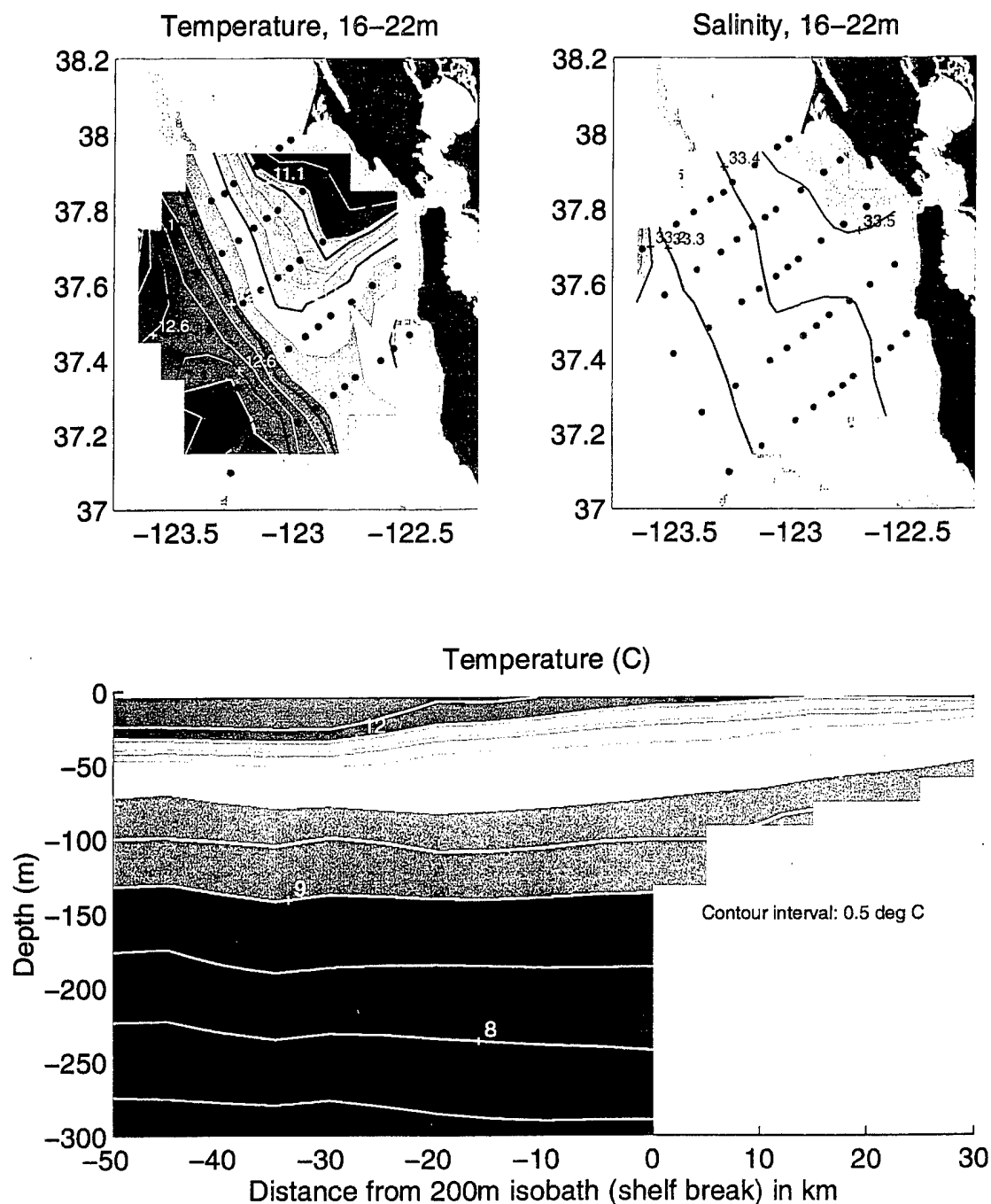


Figure 4.22 Water mass characteristics, mean of four cruises in 1991. a) Temperature at 16–22 m depth. CTD station positions are indicated by small open circles. b) Salinity at 16–22 m depth. c) Alongshore-averaged vertical transect of temperature, mean of 1991 cruises.

the shelf. Isotherms are mostly horizontal below 100 m but slope upward toward shore in the top 100 m (Figure 4.22c). The salinity pattern is similar, with offshore surface water $\sim S=1$ fresher than over the shelf (Figure 4.22b).

6. February 7-17, 1992

The circulation and hydrography in February 1992 are very different from the 1991 cruises and especially striking compared to February 1991. Except for an onshore intrusion of relatively cool, fresh equatorward flow at the southwest corner of the region, strong poleward flow with an onshore component is observed over the slope and shelf throughout the Gulf (Figures 4.23a,b,c).

Poleward flow is particularly strong (>25 cm/s in the alongshore average, >40 cm/s in the horizontal plots) and coherent in the upper 150 m over the slope. As in August, there are strong cross-shore gradients in temperature and salinity and the velocity jet is found where the water mass gradients are steepest. This poleward flow is associated with the warmest and freshest water seen at 100 m in all the cruises. Waters were generally $\sim 1^\circ$ warmer and $\sim S=1$ fresher than in February 1991 (cf. Figures 4.14a,b and Figures 4.24a,b), probably the result of onshore transport of Pacific Subarctic water in response to the strong downwelling-favorable winds (the California Current was also observed by Lynn et al. (1995) to be displaced onshore off Southern California in early 1992). The offshore thermocline is 30 m deeper than in February 1991.

No satellite SST image was available during the period of the cruise, but images captured just before the cruise and a week after the cruise show the remarkable changes that

ADCP Velocities February 7-17, 1992

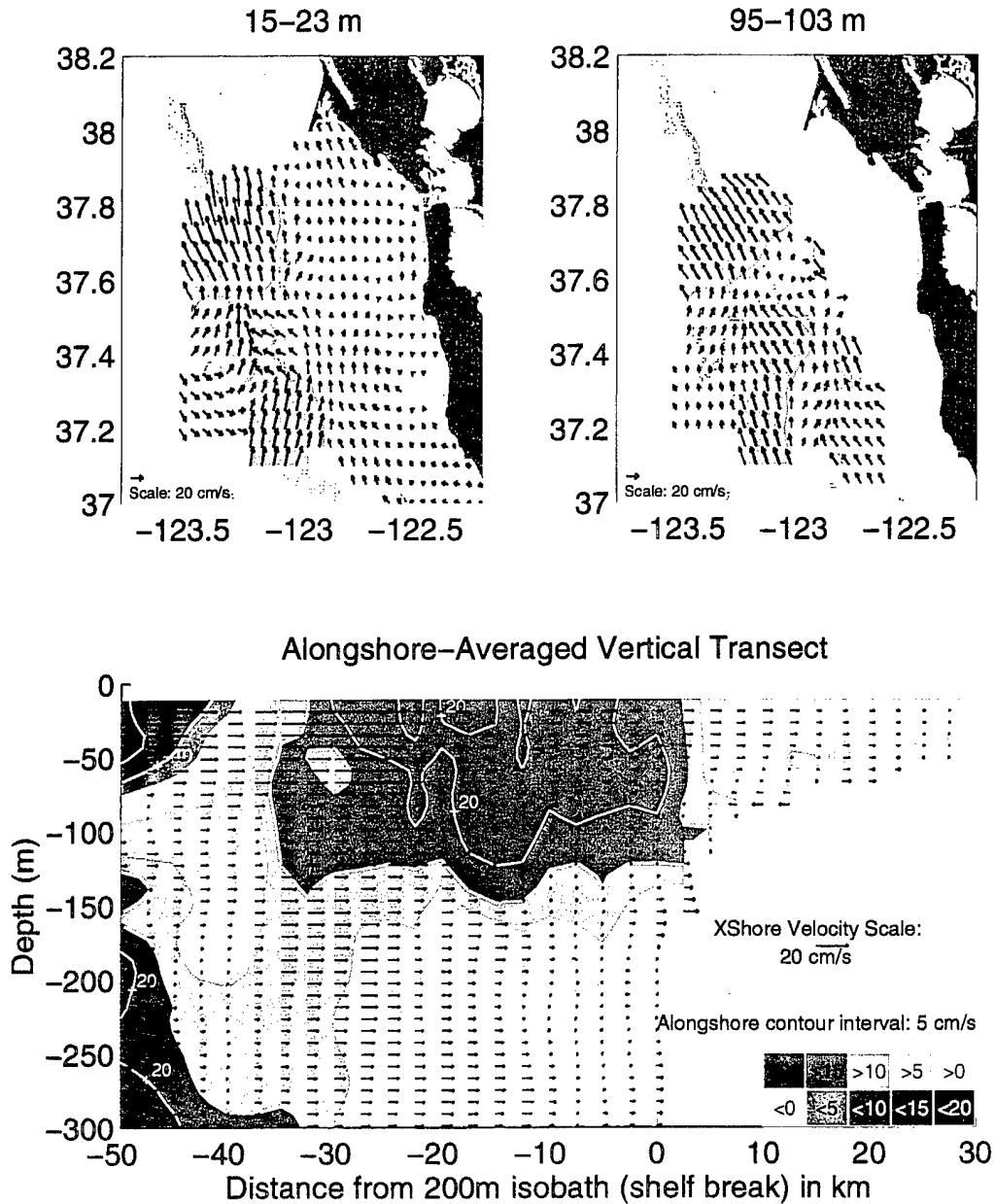


Figure 4.23 ADCP velocities, February 7-17, 1992. Otherwise same as Figure 13.

were taking place (Figures 4.24c,d). On February 4, SSTs in the Gulf and the surrounding region were 11-12°C, while on February 25 the temperatures have risen to 13.5-14.5°C.

F. TRANSPORTS AND RESIDENCE TIMES

1. Transports

A simple box model for the Gulf, subdivided into slope and shelf regions, was created to study the transport of water into and out of the region during each cruise (Figures 4.25 - .29). Referring to the figures, the box for the shelf consists of leg AB that runs southwest from Point Reyes, outer alongshore leg BE, cross-shelf leg EF off Pigeon Point, and inner alongshore leg FA. The depth range of each shelf box leg extends from 7 m (the upper limit of the shallowest ADCP bin) to within ~10% of the overall depth from the bottom. The offshore slope box model consists of legs BC, CD, DE, and EB. The depth range for the slope box extends from 7 m to the shallower of 400 m or within ~10% of the depth from the bottom. Transports through a larger "entire Gulf" box (polygon ACDF) were also calculated.

Transports were calculated by summing the gridded cross-leg ADCP velocities over the horizontal and vertical extent of each leg and multiplying by the cross-sectional area of the leg. If a leg contained ADCP velocities both "into" and "out of" the Gulf, the algebraic sum was calculated to arrive at a net transport. The box models are somewhat different for February 1992 because the northern and western legs were not occupied. To give more detail on the spatial variability of transport, exploded box diagrams are also shown where contiguous regions of transport into or out of the Gulf were integrated even if they extended over more than a leg (for ease in presentation, small regions of transport of less than 0.05 Sv in opposition to the prevailing transport were neglected in the sums shown for the

Temperature and Salinity – February 7–17, 1992

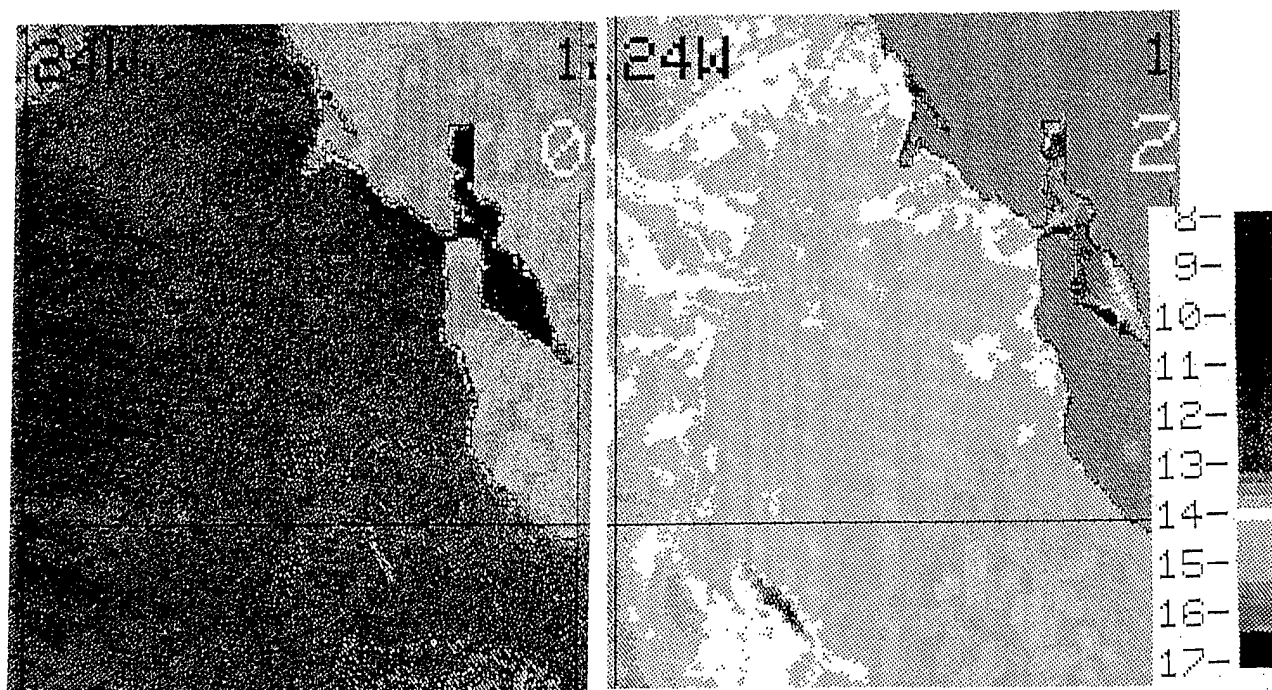
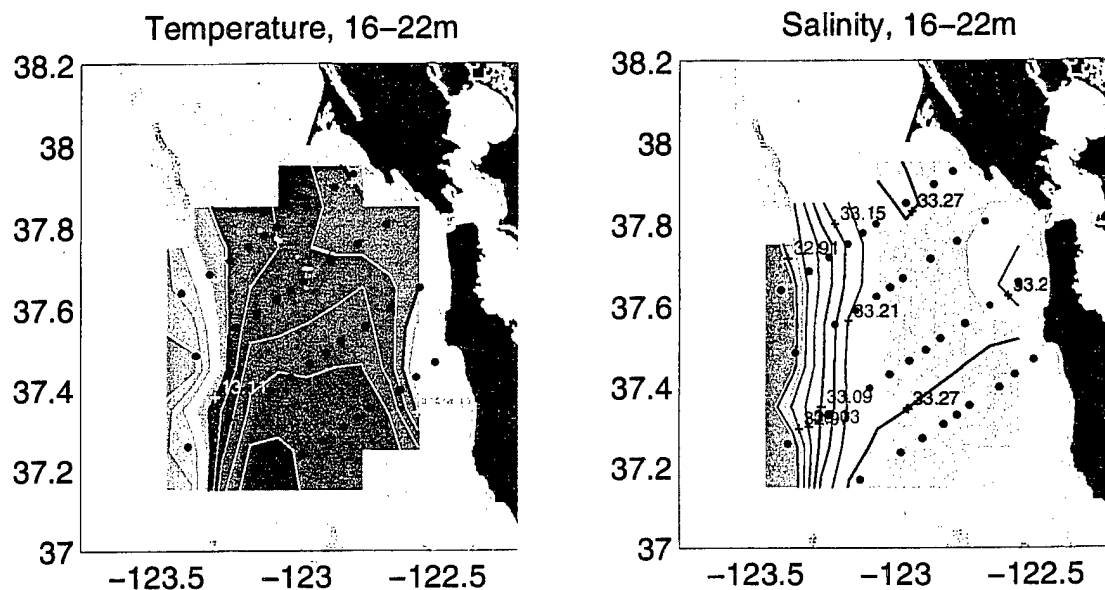


Figure 4.24 Water mass characteristics, February 7–17, 1992. c) Satellite SST image for February 4, 1992. d) Satellite SST image for February 25, 1992. Otherwise same as Figure 4.14.

exploded boxes). The net transports through each leg and into and out of the shelf, slope, and entire-Gulf boxes for each cruise are listed in Table 4.1.

The net transports into and out of each box should be zero by mass conservation (if evaporation is exactly balanced by precipitation and runoff). However, the net transports into a box during a cruise did not equal total outflow. The reasons for this include ADCP measurement errors, the lack of synopticity in measurements, and the lack of measurements from the surface layer (0 to 7 m) that the ADCP does not capture and the deep layer (within 10% of the bottom depth) that is removed in pre-processing. A method of estimating the average ADCP velocity error is to divide the amount of inflow or outflow by the sum of the area around the box. The mean error for the shelf box from the five cruises is 1.6 cm/s; the mean error for the box of the entire Gulf is 0.6 cm/s.

There is a persistent pattern of transport through the Gulf that varies only somewhat from cruise to cruise. *Net transport is always poleward over the slope*, entering through leg DE and exiting the Gulf through legs BC and/or CD. During the October/November cruise when there was a net equatorward flow through leg BC and in February 1992 cruise when there was a net onshore flow into leg CD. The transport through the shelf box is less than that through the slope box, no surprise since the volume of the slope box is six times greater than the shelf box ($12.9 \times 10^{11} \text{ m}^3$ vs. $2.0 \times 10^{11} \text{ m}^3$). The direction of the transport through the shelf is also more variable than over the slope. Transport through the inshore AF leg is very small, partly because the area is shallow.

In February 1991, the poleward transport over the slope (through the box model) was between 1.4 and 1.9 Sv (Figure 4.25). The transport over the slope was equatorward

Transports (in Sverdrups) Positive (negative) numbers indicate transport into (out of) box. Refer to Figures 4.26-30 for locations of Legs.							
Box of Entire Gulf							
	Leg DF	Leg CD	Leg AC	Leg AF	Σ Into Box	Σ Out of Box	Difference
Feb 91	0.78	-0.58	-0.68	0.01	0.79	-1.26	-0.47
May 91	2.73	-0.74	-1.34	0.06	2.79	-2.08	0.71
Aug 91	2.41	-0.32	-1.92	-0.05	2.41	-2.29	0.12
Oct 91	0.96	-0.49	0.18	-0.20	1.14	-0.69	0.45
1991	1.72	-0.53	-0.94	-0.04	1.72	-1.51	0.21
Feb 92*	2.08	1.49	-2.23	-0.05	3.57	-2.28	1.29
Box of Shelf Waters							
	Leg EF	Leg BE	Leg AB	Leg AF	Σ Into Box	Σ Out of Box	Difference
Feb 91	-0.08	0.36	0.21	0.01	0.58	-0.08	0.50
May 91	-0.09	-0.31	0.01	0.06	0.07	-0.40	-0.33
Aug 91	-0.06	0.12	0.16	-0.05	0.28	-0.11	0.17
Oct 91	0.17	0.13	-0.14	-0.20	0.30	-0.34	-0.04
1991	-0.01	0.08	0.06	-0.04	0.14	-0.05	0.09
Feb 92*	0.33	1.04	-0.23	-0.05	1.37	-0.28	1.09
Box of Slope Waters							
	Leg DE	Leg CD	Leg BC	Leg BE	Σ Into Box	Σ Out of Box	Difference
Feb 91	0.86	-0.58	-0.89	-0.36	0.86	-1.83	-0.97
May 91	2.82	-0.74	-1.35	0.31	3.13	-2.09	1.04
Aug 91	2.47	-0.32	-2.08	-0.12	2.47	-2.52	-0.05
Oct 91	0.79	-0.49	0.32	-0.13	1.11	-0.62	0.49
1991	1.74	-0.53	-1.00	-0.08	1.74	-1.61	0.13
Feb 92*	1.75	1.49	-2.00	-1.04	3.24	-3.04	0.20
*Transports for February 1992 cruise are not directly comparable to other cruises because the survey pattern was different.							

Table 4.1 Transports through the Gulf of the Farallones.

between 0.4 and 0.2 Sv. During the May cruise, the poleward slope transport was about double (2.4 to 3.0 Sv) that of February (Figure 4.26). The equatorward shelf flow though was negligible, especially in the north near Point Reyes. May is the only season where the net transports through legs BE and AF are significantly offshore, which agrees with May being the season of maximum upwelling. Strong poleward transport over the slope (2.7 to 2.9 Sv) persisted into August 1991 (Figure 4.27). Net shelf transport was equatorward between 0.1 and 0.2 Sv. The circulation pattern in October-November was not as coherent as seen in the previous seasons (Figure 4.28). Over both the slope and shelf there was considerable small-scale variability in direction of transport, leading to weak poleward transport. In February 1992, extremely strong poleward transport was seen throughout the shelf and slope regions (Figure 4.29). There appeared to be strong convergence onto the shelf from offshore, but this may be due to high variability in the wind and a lack of synopticity (the ship broke off operations several times to find shelter from rough seas). The onshore flow through leg BE is very strong, especially considering the leg was 25% shorter than in the other seasons.

ADCP data reveals that the poleward flow occurs from surface to bottom over the slope in all seasons and is much stronger than previously estimated from geostrophic calculations. Bray and Greengrove (1993) estimate 0.1 Sv poleward transport through their much larger cross-shore transect off Point Reyes that went 150 km offshore and extended much deeper than the SSE surveys (the transports presented here extend ~80 km from the coast). Also, the bidirectional flow (equatorward at the surface, poleward at depth, cf. Figure 4.2) Bray and Greengrove inferred from the hydrographic data is not seen in the SSE ADCP data.

February 1991

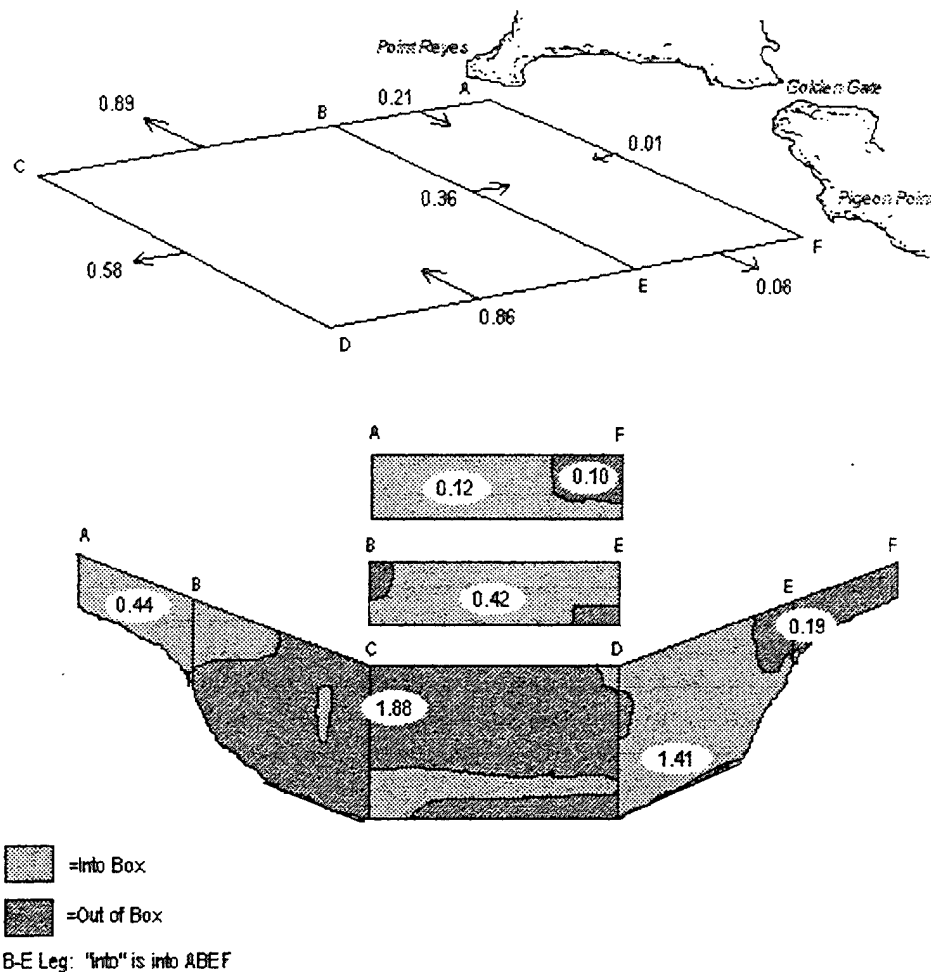


Figure 4.25 Transports through the Gulf, February 13-18, 1991. top) Box model of Gulf. Box ABEF represents the shelf (depths less than 200 m), and box BCDE covers the slope region. Transports through each leg of the boxes were calculated and are labeled. bottom) exploded view of the box model showing variation with depth. Broad regions with transports into the box are lightly shaded while regions with transports out of the box have a darker shading. Sums for contiguous regions of in or out transports are labeled. Small regions with transports less than 0.05 Sv are not labeled. For leg BE, "into the box" is defined to be into the shelf box.

May 1991

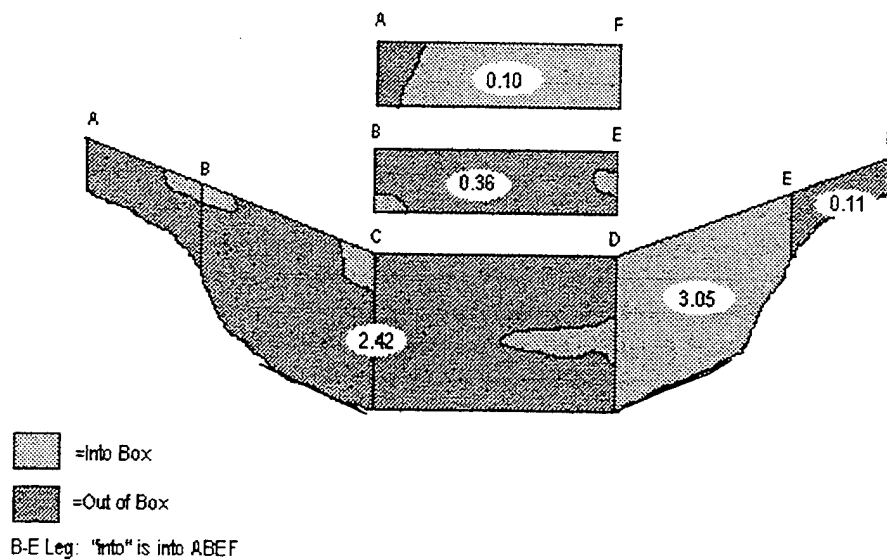
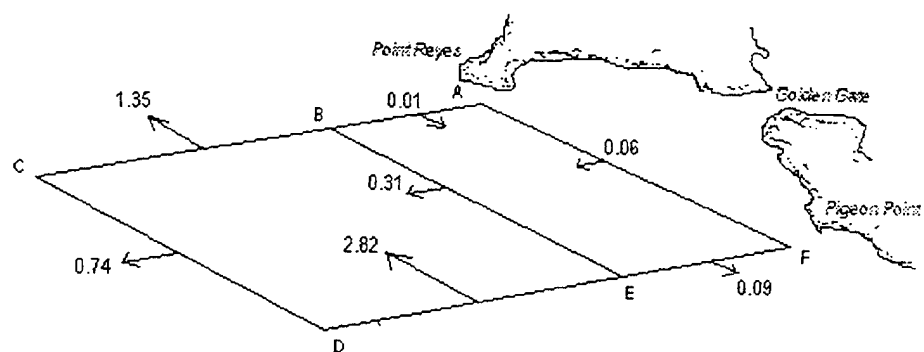


Figure 4.26 Same as Figure 4.25 except for the period May 16-21, 1991.

August 1991

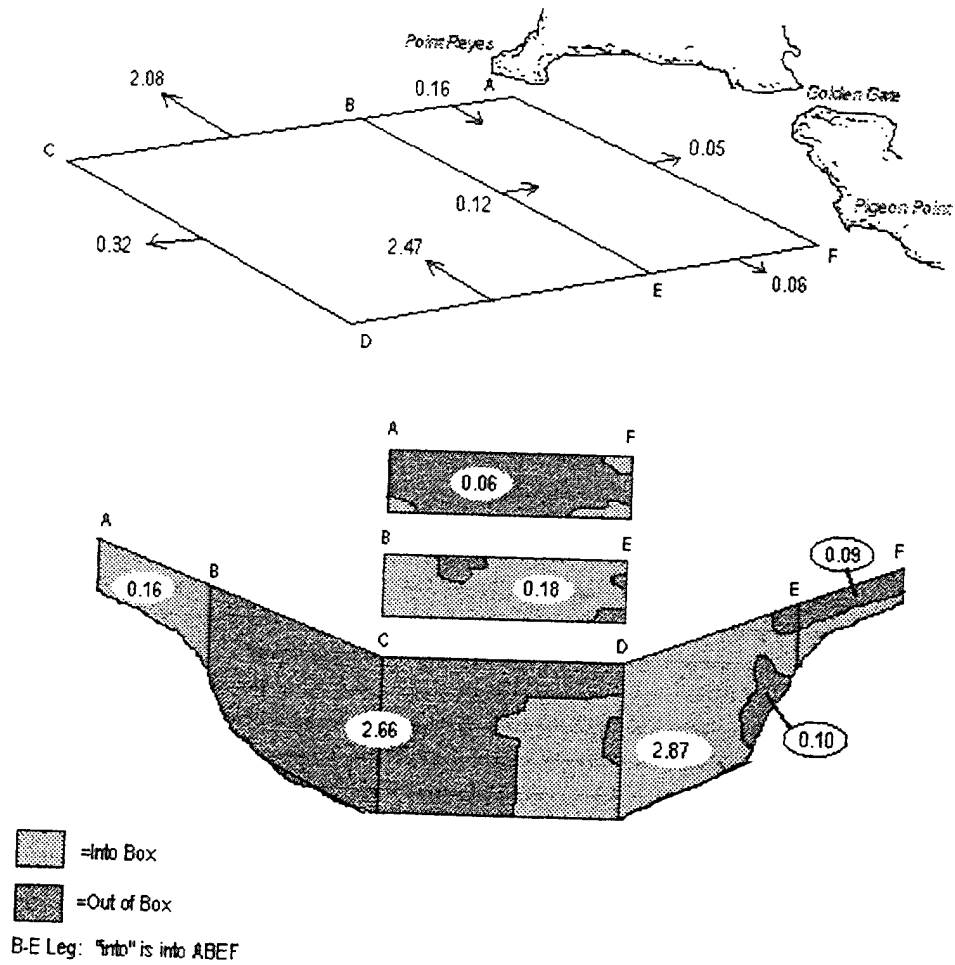


Figure 4.27 Same as Figure 4.25 except for the period August 12-18, 1991.

October/November 1991

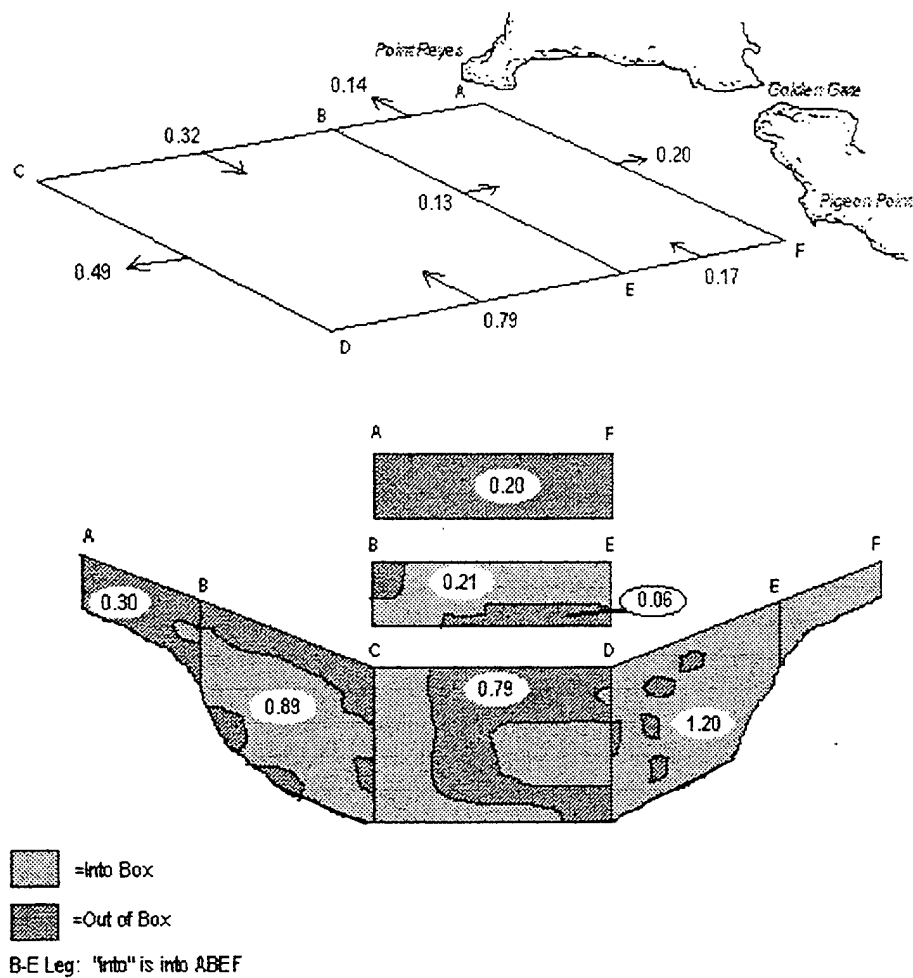


Figure 4.28 Same as Figure 4.25 except for the period October 29 - November 3, 1991.

February 1992

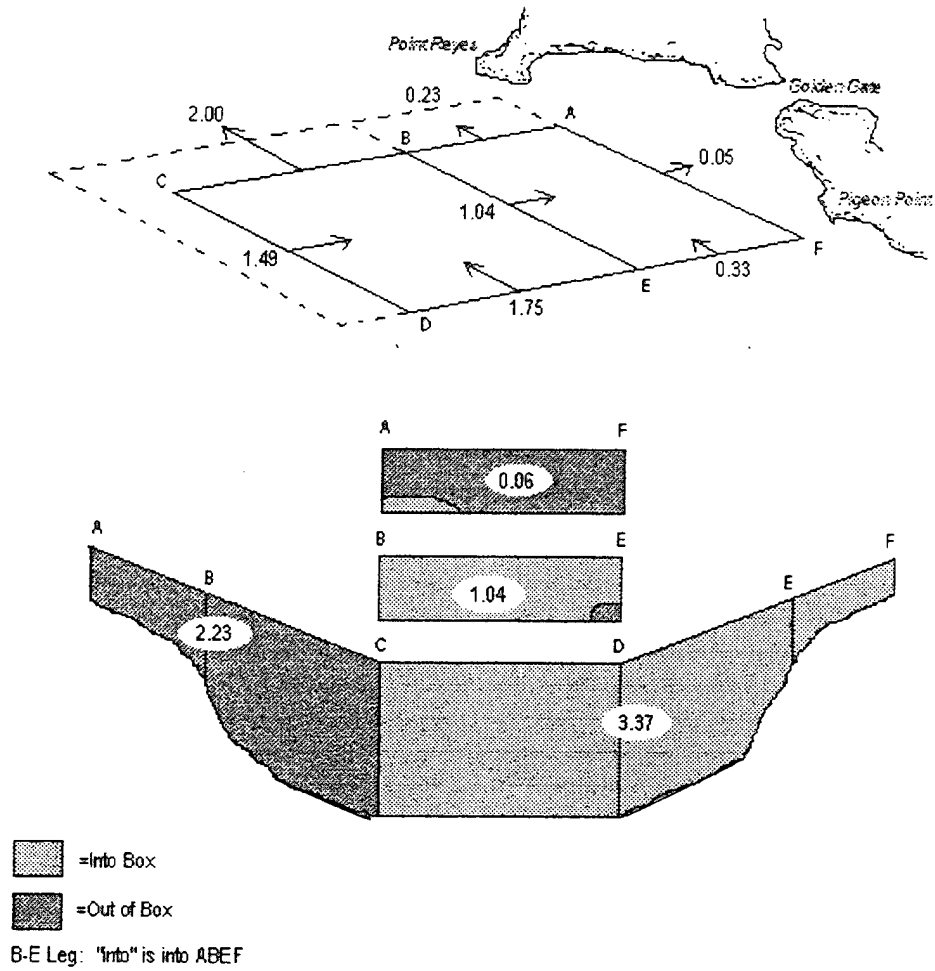


Figure 4.29 Same as Figure 4.25 except for the period February 7-17, 1992

2. Residence Times

Dividing the transport into, or out of, the region by the volume of the Gulf produces a lower-bound estimate of the time required to completely flush the Gulf. True residence times are longer as a certain amount of recirculation is expected. Tidal transports are not considered here since typical maximum semidiurnal tidal velocities are $O(3 \text{ cm/s})$ (Appendix A, Table A2) for which the tidal excursion distance is less than 0.5 km. Transport into (out of) each region (slope, shelf) of the Gulf was estimated by summing all the volume transport into (out of) the region, rather than summing the in and out through each leg as in Table 1 and Figures 4.25 -.29. Additionally, the residence time was calculated by using the average of the inflow and outflow. The residence times for the shelf, slope, and entire Gulf are listed in Table 4.2.

The mean residence time for each area is about one week, with a range in the estimates of about 2-13 days. Despite a much smaller volume, the residence time of the shelf region appears to be only slightly less than that of the slope region. There is no clear seasonal signal to the residence times. Residence times for the shelf are somewhat larger than the 3-day residence time calculation by Gezgin (1991), but the numbers are not completely comparable since his region was smaller (and for similar flow regimes larger volumes have larger residence times).

G. DISCUSSION

Contrary to what should be expected from the existing model of the large-scale California Current system circulation, increased poleward flow in the Gulf of the Farallones is accompanied by a *decrease* in salinity of the surface waters over the slope. To explain this phenomena, a conceptual model of the relationship between poleward

Residence Time (T_R) (in Days)						
Box of Entire Gulf						
	Transport In	T_R	Transport Out	T_R	$\overline{Transport}$	$\overline{T_R}$
Feb 91	2.0	8.6	2.1	8.2	2.1	8.2
May 91	3.3	5.2	2.5	6.9	2.9	5.9
Aug 91	3.1	5.6	2.9	5.9	3.0	5.8
Oct 91	2.1	8.2	1.3	13.3	1.7	10.0
1991	2.6	6.6	2.2	7.8	2.4	7.2
Feb 92*	3.6	4.8	2.4	7.2	2.9	4.7
Box of Shelf Waters						
	Transport In	T_R	Transport Out	T_R	$\overline{Transport}$	$\overline{T_R}$
Feb 91	0.7	3.1	0.2	9.4	0.5	4.6
May 91	0.2	11.9	0.5	4.4	0.4	6.4
Aug 91	0.4	5.8	0.2	10.8	0.3	7.5
Oct 91	0.4	5.8	0.4	5.3	0.4	5.6
1991	0.4	5.3	0.3	6.5	0.4	5.7
Feb 92*	1.4	1.6	0.3	7.6	0.8	2.2
Box of Slope Waters						
	Transport In	T_R	Transport Out	T_R	$\overline{Transport}$	$\overline{T_R}$
Feb 91	1.7	8.7	2.4	6.2	2.0	7.3
May 91	3.5	4.3	2.4	6.2	3.0	5.0
Aug 91	2.9	5.1	2.9	5.1	2.9	5.1
Oct 91	2.0	7.3	1.2	12.4	1.6	9.3
1991	2.5	6.0	2.2	6.8	2.4	6.2
Feb 92*	3.2	3.8	3.1	4.8	3.2	3.8
*Transports and Residence Times for February 1992 cruise are not directly comparable to other cruises because the survey pattern was different.						

Table 4.2 Residence Times in the Gulf of the Farallones.

flow over the continental slope, wind relaxation, cross-shore flow, and the characteristics of the water mass over the slope is presented. The model is consistent with historical observations and explains conditions seen in the Gulf of the Farallones during the 1991-92 Slope-Shelf Experiment.

The model postulates: (1) There exists a relatively barotropic poleward flow over the continental slope of the west coast, probably seasonally varying, which transports Equatorial Pacific water northward. The poleward flow extends from the surface to greater than 1000 m depth within ~50 km of the shelf break. (2) Off central California, southward blowing winds cause offshore Ekman transport of the surface layers and upwelling of cool, salty water. As sea levels at the coast drop, an equatorward surface geostrophic flow is set up. This equatorward flow is superimposed upon the broad poleward flow and, depending on the strength of each, net poleward or equatorward flow may be present. (3) When the winds periodically relax or reverse and blow towards the north, geostrophic adjustment brings fresher Pacific Subarctic water onshore. As the equatorward geostrophic flow diminishes, more of the barotropic poleward flow is apparent. A baroclinic component of poleward flow may commence if the sea surface slopes upwards towards the coast (full downwelling). (4) Mesoscale mixing caused by the periodic onshore movement of Pacific Subarctic water into the region dilutes the Equatorial Pacific water carried by the poleward flow. A diagram of the essentials of the model is shown in Figure 4.30.

1. Barotropic Poleward Flow

Poleward flows of various strengths, positions, and depths have been repeatedly sighted over the slope from the tip of Baja to Washington and, especially in observations

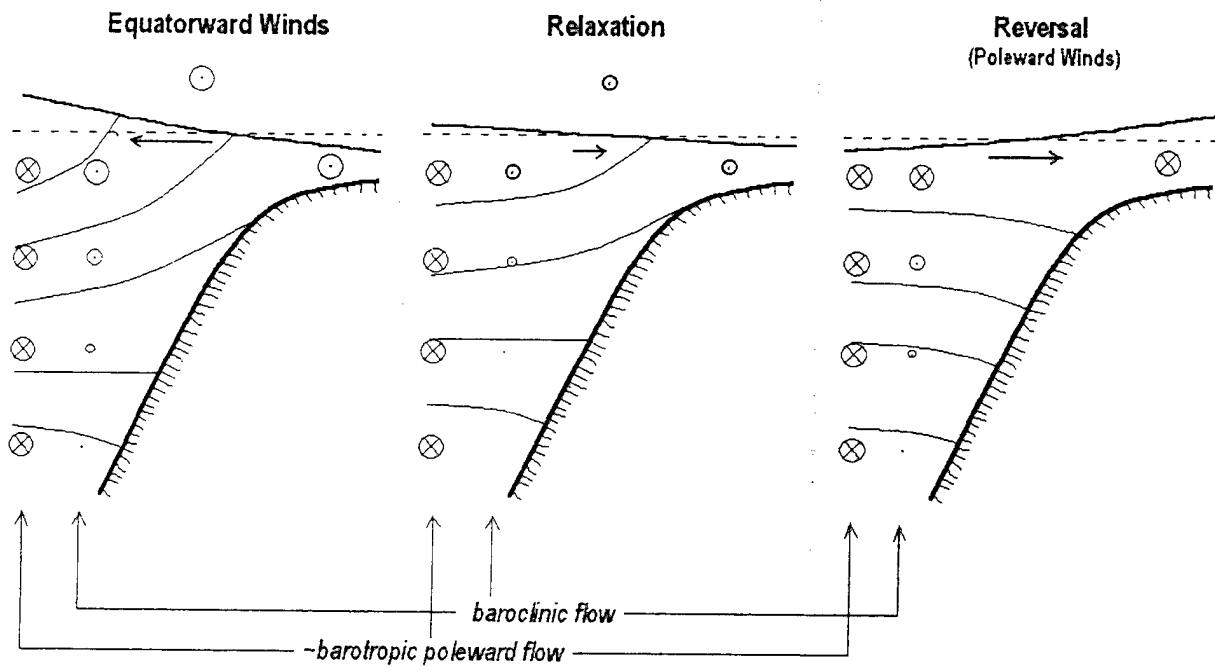


Figure 4.30 Conceptual model of the relationship between the wind, water mass characteristics, and flow over the slope during conditions of equatorward winds, relaxation, and poleward winds. Circle with a center dot (cross) indicates equatorward (poleward) flow. Size of circle represents magnitude of flow. Dashed line represents a level surface.

collected south of Point Conception, are associated with warm, salty Equatorial Pacific water (Hickey, 1979; Lynn et al., 1982). The variability and sometimes absence of the poleward flow could be the result of several factors. Observations at different times of the year could be capturing annual variability. Poleward flow could be moving on and offshore out of the range of observations. There could be errors in the methods of observation. Or, poleward flow could be fluctuating more frequently than seasonally in response to external driving forces.

Historical information derived from dynamic topography estimated from temperature and salinity data collected during oceanographic cruises is problematic. Recent current meter time series have shown that there can be significant poleward flow at depths greater than 1000 m over the slope (Kinoshita et al., 1992), suggesting that the historical calculations of dynamic topography which assumed a zero-velocity layer at 500 m under represent (or perhaps in some cases misrepresent) the poleward flow. For example, monthly and seasonal climatologies of geostrophic velocities off California suggest that poleward flow is weak or absent in the spring (Wyllie, 1966; Pavlova, 1966; Chelton, 1984; Lynn and Simpson, 1987; Tisch et al., 1992), yet current meter time series show that spring is the season of maximum poleward flow (Wickham et al., 1987; Collins et al., 1996; Huyer et al., 1989). Therefore, direct measurements of currents are necessary for determining the prevalence and seasonality of the poleward flow.

There is evidence that poleward flow varies seasonally. Huyer and Smith (1976) saw poleward flow increase in May 1975 at a slope current meter mooring off Oregon, and Hickey (1981) later saw an increase in Equatorial water off Washington in July-August which may

have been the result of increased poleward flow. The best evidence of an annual cycle of alongshore flow comes from a nearly six-year current meter mooring at 350 m depth off Point Sur (Collins et al., 1996). They found 4-8 cm/s poleward flow most of the year, which increased to 10-16 cm/s from early April to mid-August.

The curl of the wind stress as a likely origin for a barotropic poleward flow over the slope was suggested by Hickey (1979) and shown to produce poleward flow in numerical models (McCreary et al., 1987). The seasonality of the flow may be a result of the seasonally varying band of positive wind curl along the west coast that extends several hundred kilometers offshore throughout the year (Nelson, 1977). Other possible driving mechanisms for poleward flow have been suggested and reviewed by Clarke (1989). However, the mechanism that generates poleward flow is unimportant to the principles of the conceptual model presented here, as long as it provides for a broad, nearly continuous barotropic flow.

In addition to seasonal variability, current meter time series also show that alongshore currents vary on scales of days to weeks, which may be another explanation for the variability in historical observations. In the next two subsections, mechanisms for this variability are proposed which also explain the variations in poleward flow seen in the detided ADCP data collected during the Slope/Shelf Experiment cruises.

2. Equatorward Winds

The generally equatorward winds off central California produce a classical coastal upwelling pattern (Nelson, 1977). In the presence of these winds, the surface layer of the ocean is transported offshore (Ekman, 1905), depressing sea level along the coast and causing the isopycnals in the upper 200-250 m to slope upwards towards the coast.

In the alongshore-averaged transects of temperature and salinity measured during the May 1991 Slope/Shelf Experiment cruise (the period of greatest seasonal upwelling (Nelson, 1977)), isotherms and isohalines slope upward towards the coast as far as 50 km from the shelf break (Figure 4.8). Cross-shore ADCP velocities are offshore in the upper 100 m while generally onshore or weakly offshore at depth (Figure 4.15). The downward slope of the sea surface downwards towards the coast is balanced by an equatorward geostrophic current (Figure 4.12). The alongshore-averaged geostrophic velocity transect for May 1991 (calculated relative to 500 m depth) shows a core of strong (10-35 cm/s) equatorward flow in the upper 100 m between 20-30 km from the shelf break.

However, detided ADCP alongshore currents are *poleward* over most of the slope (Figure 4.15). The geostrophic calculations do not include the poleward flow probably because it is barotropic beyond 500 m depth, but there may also be an ageostrophic character to the poleward flow in the vicinity of the coast. The coastward slope of the isopycnals is greatest near the surface (Figure 4.8) which accounts for the baroclinic character of the equatorward flow. As the baroclinic equatorward flow attenuates with depth, the large-scale barotropic poleward flow becomes prevalent.

3. Relaxation

While the alongshore winds off the coast of central California are generally equatorward, they are also marked by periods of relaxation or reversal to poleward stress. These non-periodic relaxation events occur about every ten days and last for periods of hours up to several days (Figure 4.5). In the conceptual model presented here, two phenomena

occur as a result of the wind relaxation; offshore water of lower salinity associated with the California Current moves onshore, and the apparent poleward flow increases.

During upwelling-favorable winds, the surface Ekman layer flows offshore where it mixes with the higher-salinity Pacific Subarctic water of the California Current, becoming fresher. It is also exposed to the effects of solar heating and can become warmer. When the wind relaxes and there is no longer an external force to balance the sloping sea surface, the equatorward geostrophic current is reduced. The upward sloping isopycnals adjust downward, producing a warmer and fresher signal on pressure surfaces throughout the upper 200-300 m.

As the reduced sea surface slope no longer provides the impetus for geostrophic equatorward flow, the omnipresent poleward flow appears to accelerate. If the sea surface begins to tilt upward towards the coast to balance an increasing poleward (downwelling-favorable) wind stress, a baroclinic poleward geostrophic current (similar to the baroclinic equatorward flow during upwelling-favorable winds) will develop. The acceleration of poleward flow with wind relaxations has been seen elsewhere (Hickey, 1979; Tisch et al., 1992; Chelton et al., 1987, 1988). An increase in the relative concentration of warm, fresh water near the central California coast during wind relaxations was also observed by Rosenfeld et al. (1994) and Parker (1996). Both suggested it was due to onshore movement of California Current water.

Since during relaxation conditions poleward flow accelerates at the same time that fresher water moves onshore, increased poleward flow should not necessarily be correlated with an increase in warm, salty Equatorial Pacific water in the region, as models of the

seasonal California Current suggest (Figure 6.13, Johnson, 1990). This was the case twice during the Slope/Shelf Experiment. In August 1991, winds were anomalously poleward just prior to the start of the cruise. Strong poleward flow is seen over the entire slope, but surface Ekman velocities are strongly onshore and salinities and temperatures are much lower throughout the Gulf of the Farallones (cf. Figures 4.8 and -9) suggesting a downwelling event. Geostrophic velocities are poleward but weaker than the mostly barotropic ADCP measurements (Figure 4.12).

In February 1992, there were sustained, strongly anomalously poleward winds. Strong poleward ADCP flow is seen over the slope but the strongest flow is much more concentrated in the upper 100 m than seen in August. The core of poleward flow is very evident in geostrophic velocities at the surface (cf. Figure 4.23c and 4.12). Flow is strongly onshore and the Gulf is warmer and fresher relative to October 1991 (cf. Figures 4.10 and 4.11). Essentially, the sustained strong poleward winds have displaced the California Current onshore creating a deeper mixed layer and a positive surface pressure gradient. The adjustments in the density field in the upper 300 m are balanced by a strongly baroclinic geostrophic poleward flow in the upper 150-200 m.

The changes in the Gulf of the Farallones in February 1992 have been explored by Ramp et al. (1997) who attribute it partly to the 1992 ENSO. They suggest that the anomalously poleward winds are atmospherically teleconnected to the ENSO changes in the tropics. Sea level heights and output from a global circulation model suggest that an ENSO-related Kelvin Wave passed through the Gulf at the same time as the February cruise. Ramp et al. were also struck by the low salinity found in the Gulf and proposed a similar model of onshore flow of California Current water driven by the poleward winds, and predicted that

the increased poleward flow would eventually raise salinity in the Gulf by April or May. In fact, T-S analysis of Gulf waters from a cruise in May-June 1992 show that salinity was still lower than normal on density surfaces (Baltz, per. comm.).

Send et al. (1987) have presented a different model of relaxation. Data from current meter moorings on the shelf north of Point Reyes (The Coastal Ocean Dynamics Experiment - CODE) showed a strong correlation between wind relaxation, increased poleward flow, and increased temperature (Winant et al., 1987). They concluded that during relaxation cross-shore advection was small and northward alongshore advection of solar-heated waters was responsible for the rise in temperature. Salinity data was only available during hydrographic cruises but in the sparse data they found little change in salinity when the wind relaxed. When on occasion lower salinity was seen during relaxation, they suggested it was fresh water disembogued from San Francisco Bay and transported northward around Point Reyes.

However, the Send model for relaxation is designed to explain the observations collected over the shelf region north of Point Reyes, and does not explain the fresher waters (or onshore currents) seen over the slope in the Gulf of the Farallones during relaxation. Climatological maps of temperature and salinity (Lynn et al., 1982) show that *the only reasonable source of warm, fresh water is from offshore.*

4. Event-driven Mixing

The relative quantity of Equatorial Pacific water over the slope with distance north in the California Current (Lynn et al., 1982). This has been explained as gradual mixing of the Equatorial Pacific water carried by the poleward flow with the offshore Pacific Subarctic. However, in the conceptual model presented here, the periodic onshore movement of Pacific

Subarctic water accompanied with acceleration of the poleward flow may be the major mixing agent. Thus, instead of gradual mixing along the course of the poleward flow, the mixing may be episodic, driven by wind events approximately every 10 days.

The flow in the Gulf of the Farallones region is the sum of a large-scale barotropic poleward slope flow and the mesoscale Ekman circulation set up by regional wind forcing (which fluctuates on synoptic time scales). During periods of strong equatorward wind stress (e.g. May 1991) shelf and near-surface slope flow is equatorward with the traditional model of a poleward undercurrent. If winds are relaxing or poleward, however, the entire area features a generally poleward flow at all depths that appears to be relatively barotropic.

H. APPLICATIONS TO THE DISPOSAL OF DREDGE SPOILS

Material dredged from San Francisco Bay to maintain safe navigation is transported offshore in barges and dumped at a site over the continental slope off the Gulf of the Farallones. It is undesirable for currents to carry the dredged materials back onshore and into the federally-protected waters of the Gulf of the Farallones National Marine Sanctuary and the Monterey Bay National Marine Sanctuary. The observations presented here strongly suggest that it would not be prudent to dump over the slope during a wind relaxation or reversal event as these are the periods of maximum onshore flow. Wind reversals may occur at any time during the year.

I. SUMMARY

Based on five cruises in 1991-92, the circulation in the Gulf of the Farallones appears to be dominated by forces acting on an event scale rather than on a seasonal scale. For example, February is not normally a strong upwelling month yet during strong than normal

equatorward winds in 1991 the ocean quickly adjusted and the pattern of Ekman transport was seen. Likewise, anomalously poleward winds like those in August 1991 and February 1992 are believed to instigate dramatic changes in water characteristics and a strong poleward flow. However, during all wind conditions, poleward flow was seen over the slope from the surface to the limit of the ADCP data. Increased poleward flow was associated with wind relaxations and reversals, during which onshore transport of warmer, fresher water was observed. ADCP data provide much more detail on the structure of the currents over the slope and shelf in the Gulf and reveal the pervasive, barotropic nature of the poleward flow that was not evident in the historical inferences of velocity from hydrographic samples.

V. FUTURE WORK

High-quality ADCP data collected from research ships while underway has become available only since the recent advent of continuous GPS coverage in the early 1990s. The data sets described here, collected in 1991, 1992, and 1993, illustrate the value of direct measurements to test circulation models of areas based on historical hydrographic data. Steady improvement of transducers, signal processing, and navigation means that the quality and quantity of ADCP data will steadily improve in the future. Indeed, the development of autonomous surface drifting buoys that continually profile currents cannot be far away. Physically-based models that can easily assimilate ADCP and CTD data would contribute greatly to the determination of circulation patterns and their causes.

In the investigation of the currents near the Galapagos Islands in Chapter II, the divergence of the Equatorial Undercurrent around the archipelago predicted by analyses of hydrographic records was observed. A specific study to determine the cause of the biologically rich plumes west of the Archipelago would combine a current meter mooring at 0.5°S , 92°W with routine SeaWiFS measurements from space. The IRONEX program was not specifically designed to study the divergence of the currents and it is hoped future cruises in the region are able to collect data southwest of Isla Isabella to learn the fate of the deflected water and whether it is a persistent feature. The relationship between the strength of the regional currents and westward-propagating Legeki waves also needs to be investigated.

As mentioned in the last paragraph of Chapter III, there are a number of possible improvements to the method of constructing a tidal model from empirical data. It would be good to further quantify the effects of increasing the order of fit on the mean and tidal constituents. Additionally, there are outstanding questions on whether the model would be improved by giving different weights to the ADCP and current meter measurements.

The two-dimensional conceptual model of the relationship between the winds, water characteristics, and currents could be strengthened by incorporating the effects of alongshore variability. A good test of the model would be to analyze the correlation between hourly winds and current meter data collected during the SSE. Several of the moorings also had temperature sensors. Although this data set was not specifically designed to study mesoscale variability in the Gulf, the data should be further investigated to find the degree of variability and the importance of $O(10\text{ km})$ eddies on the circulation. Processes cover many scales and more detailed space and time sampling of the inner Gulf is warranted. Possible important processes are the tidal jet out of the Golden Gate, strength of the nearshore currents, the residual flow affecting the exchange of waters between San Francisco Bay and the Gulf, and mixing due to island wakes and banks. Ocean surface current radar observations would be useful in this region. In addition to the mass transports presented here, the heat and salt fluxes should be calculated.

APPENDIX A. CURRENT METERS IN THE GULF OF THE FARALLONES

To provide a resource for further studies in the Gulf of the Farallones, a listing of all known current meters moorings deployed in the region is included (Table A1). In addition to these meters, a large number of moorings which are not listed have been deployed within the Golden Gate and inside San Francisco Bay.

For all available current meter time series (except those on the 1975 and 1977 EPA moorings), the tidal ellipse characteristics have been calculated for the M_2 , S_2 , K_1 , and O_1 constituents (Tables A2-A5) and plotted as the magnitudes and orientations of the semi-major axes (Figure 3.2).

KNOWN MOORINGS IN THE GULF OF THE FARALLONES				
Experiment	Mooring	Location	Depth	Dates
Hickey ¹	RP3	37.878N 122.623W	10m	11/13/92-2/25/93
Slope/Shelf Experiment ²	A	37.545N 122.854W	10m	3/8/91-5/17/91 ; 7/14/91-1/5/92
			50m	3/8/91-5/17/91 ; 7/4/91-2/8/91
			80m	3/8/91-8/13/91
	B	37.477N 122.996W	10m	7/4/91-9/23/91
			150m	3/9/91-2/8/92
			260m	3/9/91-2/8/92
			390m	3/9/91-2/8/92
	C	37.422N 123.135W	10m	3/9/91-5/17/91 ; 7/4/91-2/8/92
			75m	3/9/91-3/21/91 ; 7/5/91-2/8/92
			150m	3/9/91-8/13/91
			250m	3/9/91-8/13/91
			400m	3/9/91-3/18/91 ; 8/14/91-9/10/91
			790m	3/9/91-3/30/91 ; 8/14/91-3/11/92
	D	37.364N 123.267W	75m	3/10/91-5/21/91 ; 7/5/91-2/13/92
			250m	3/10/91-9/3/91
			400m	3/10/91-2/13/91
			800m	3/10/91-6/11/91 ; 8/1/91-2/13/92
			1390m	8/14/91-2/13/92
	E	37.640N 123.300W	75m	3/11/91-4/16/91
			250m	3/11/91-8/15/91
			400m	3/11/91-2/12/92
			800m	3/11/91-2/12/92
			1400m	3/11/91-2/12/92
			1987m	3/11/91-2/12/92
	F	37.700N 123.144W	75m	3/11/91-4/4/91 ; 8/15/91-2/10/92
			150m	3/12/91-2/13/92
			250m	3/11/91-2/13/92
			387m	3/11/91-2/13/92

Table A1 Known current meter moorings in the Gulf of the Farallones. Data for each meter except those on the 1975 and 1977 EPA moorings have been located and found to be usable. Locations of the moorings are shown in Figure 2.1.

USGS/ Corps of Engineers ³	346	37.635N 123.352W	200m	7/7/90-8/21/90
			400m	7/7/90-8/21/90
			800m	7/7/90-8/21/90
	334	37.686N 122.796W	30m	5/5/89-10/13/89
			49m	5/5/89-10/11/89
	335	37.784N 122.933W	30m	5/5/89-10/13/89
			59m	5/5/89-10/10/89
	Corps of Engineers ⁴	1M	21m	5/8/88-6/7/88 ; 1/30/89-5/27/89
			40m	5/8/89-5/27/89
		B1B	21m	4/27/88-1/20/89
			46m	4/27/88-6/2/89
			85m	4/27/88-1/20/89
CH2M Hill ⁵	A	37.705N 122.584W	8m	6/19/87-8/2/87 ; 8/17/87-8/19/87 9/25/87-4/21/88 ; 5/9/88-7/18/88
			14m	6/19/87-7/27/87 ; 8/17/87-9/9/87 9/24/87-11/06/87 ; 11/18/87- 4/21/88 5/9/88-7/18/88
			20m	6/19/87-7/26/87 ; 8/17/87-8/19/87 9/24/87-4/21/88 ; 5/9/88-7/18/88
	B	37.705N 122.547W	8m	9/26/87-10/28/87 ; 4/27/88-6/3/88
			14m	4/27/88-6/3/88
	C	37.704N 122.517W	8m	9/26/87-10/28/87 ; 4/27/88-6/3/88
	D	37.748N 122.555W	8m	9/25/87-10/28/87 ; 4/27/88-6/3/88
	E	37.788N 122.527W	8m	9/25/87-10/28/87 ; 4/26/88-6/4/88
			14m	9/25/87-10/28/87 ; 4/26/88-6/4/88
			20m	9/25/87-10/28/87 ; 4/26/88-6/4/88
	F	37.725N 122.605W	8m	4/26/88-6/3/88
			14m	4/26/88-6/3/88
CCCCS ⁶	K	37.289W 122.668W	70m	2/14/84-2/3/85
	L	37.173N 122.926W	70m	2/14/84-1/25/85
			210m	2/14/84-1/25/85
			470m	2/20/84-10/17/84

Table A1 (cont.)

SuperCODE	H3	37.370N 122.650W	35m	4/22/81-3/10/82 ; 5/23/82-9/11/82
			65m	4/22/81-9/11/82
	H4	37.370N 122.850W	38m	5/8/81-6/4/81
			70m	5/8/81-6/4/81
			110m	5/8/81-6/4/81 ; 8/16/81-3/6/82
EPA 1977 ⁸	2920	37.610N 123.126W	911m	10/25/77-3/15/78
	2830	37.614N 123.246W	912m	10/25/77-2/6/78
	VACM		911m	10/25/77-10/24/78
	2918	37.614N 123.291W	1800m	10/25/77-12/21/77
	2919		1829m	10/25/77-3/10/78
EPA 1975 ⁹	1009	37.625N 123.283W	1729m	8/21/75-9/17/75
	1028	37.642N 123.300W	1849m	8/22/75-9/17/75
FOOTNOTES: 1. Personal communication with Barbara Hickey. 2. Ref.: Kinoshita et al., 1992. 3. Ref.: Noble and Gelfenbaum, 1991. 4. Ref.: Sherwood et al., 1989. 5. Ref.: CH2M Hill, 1989. 6. Ref.: Bratkovich et al., 1991. 7. Ref.: Denbo et al., 1984. 8. Ref.: Crabbs, 1983 which references Interstate Electronics Corp, 1982 as primary source. 9. Ref.: Crabbs, 1983 which references unpub. material from R. Schwartzlose of SIO as primary source.				

Table A1 (cont.)

M2 Tidal Ellipse Characteristics									
Station Name and Depth	Semi-major Axis (cm/s)	Semi-minor Axis (cm/s)	Inclination (deg fm E)	Phase (deg)	Station Name and Depth	Semi-major Axis (cm/s)	Semi-minor Axis (cm/s)	Inclination (deg fm E)	Phase (deg)
Hickey RP1 10m	10.9	0.5	346.9	104.4	USGS/COE 335 59m	3.1	1.4	30.5	63.5
SSE A 10m	5.7	0.9	55.2	61.9	USGS/COE 346 200m	4.0	0.1	156.3	130.5
SSE A 50m	4.0	1.4	97.1	116.3	USGS/COE 346 400m	2.7	1.4	73.4	60.7
SSE A 80m	4.1	1.2	84.0	91.5	USGS/COE 346 800m	4.3	-1.9	161.4	134.1
SSE B 10m	1.0	-0.6	153.5	145.5	COE 1M 21m	7.5	0.3	76.2	82.2
SSE B 150m	4.1	0.2	82.9	101.7	COE 1M 40m	5.9	1.5	67.5	67.9
SSE B 260m	4.3	0.6	111.3	85.3	COE B1B 21m	3.4	2.8	166.1	158.0
SSE B 390m	4.1	0.5	109.8	137.2	COE B1B 46m	4.3	1.2	104.7	105.2
SSE C 10m	3.1	1.2	104.2	129.7	COE B1B 85m	4.5	0.3	96.3	121.7
SSE C 75m	4.0	0.0	80.8	123.6	CH2M Hill A 8m	17.2	-3.0	88.3	108.0
SSE C 150m	4.2	-0.1	75.6	102.2	CH2M Hill A 14m	17.4	-2.6	78.3	91.3
SSE C 250m	4.6	-0.4	76.2	102.3	CH2M Hill A 20m	16.4	0.4	69.1	74.6
SSE C 400m	6.4	-1.9	95.9	109.0	CH2M Hill B 8m	22.0	-1.6	92.5	110.7
SSE C 790m	8.7	-3.0	105.9	131.6	CH2M Hill B 14m	4.0	-0.5	58.6	92.0
SSE D 75m	4.2	-0.4	116.2	144.2	CH2M Hill C 8m	21.1	0.4	112.7	88.3
SSE D 250m	2.3	1.2	113.6	188.2	CH2M Hill D 8m	33.9	-1.2	79.3	104.2
SSE D 400m	2.7	0.5	101.5	127.8	CH2M Hill E 8m	71.7	-6.4	70.0	126.9
SSE D 800m	5.1	-1.2	93.2	85.9	CH2M Hill E 14m	58.6	-0.5	72.8	126.4
SSE D 1390m	5.1	0.5	116.6	93.6	CH2M Hill E 20m	41.2	4.6	75.4	124.8
SSE E 75m	2.7	-1.7	137.0	333.0	CH2M Hill F 8m	25.7	-4.9	69.9	105.4
SSE E 250m	2.5	1.0	50.7	85.1	CH2M Hill F 14m	19.6	-0.1	59.4	85.2
SSE E 400m	2.4	1.6	84.9	84.0	CCCCS K 70m	9.6	-1.3	84.9	119.4
SSE E 800m	3.7	-1.1	138.6	145.7	CCCCS L 70m	10.5	-5.6	100.9	313.4
SSE E 1400m	2.2	-0.5	107.2	99.2	CCCCS L 210m	6.1	-1.2	94.6	122.1
SSE F 75m	2.5	0.1	24.6	51.3	CCCCS L 470m	4.9	-0.4	94.6	227.3
SSE F 150m	2.2	0.2	164.2	164.5	SuperCODE H3 35m	8.8	-0.2	100.5	76.7
SSE F 250m	1.1	0.3	141.6	96.8	SuperCODE H3 65m	7.5	0.8	91.8	94.2
SSE F 387m	0.8	0.1	69.1	332.5	SuperCODE H4 38m	13.7	-4.0	133.8	116.3
USGS/COE 334 30m	6.0	1.1	80.8	109.7	SuperCODE H4 70m	9.8	-0.5	139.1	125.0
USGS/COE 334 49m	6.0	1.2	66.1	94.3	SuperCODE H4 110m	4.9	2.0	109.9	119.3
USGS/COE 335 30m	3.3	1.3	26.5	61.1					

Table A2 Ellipse characteristics for the M₂ tide calculated for each current meter deployed in the Gulf of the Farallones since 1981. Inclination is the bearing of the semi-major axis as measured counterclockwise from east (090°). Phase is the time in hours since 00:00 January 1, 1980 that the tide is oriented with the semi-major axis, divided by the tidal frequency (12.42 hours), multiplied 360°, and finally truncated to fall within 0-360°.

S2 Tidal Ellipse Characteristics									
Station Name and Depth	Semi-major Axis (cm/s)	Semi-minor Axis (cm/s)	Inclination (deg fn E)	Phase (deg)	Station Name and Depth	Semi-major Axis (cm/s)	Semi-minor Axis (cm/s)	Inclination (deg fn E)	Phase (deg)
Hickey RP1 10m	1.9	0.0	165.8	351.9	USGS/COE 335 59m	1.2	0.3	163.4	252.7
SSE A 10m	2.2	0.8	58.9	124.5	USGS/COE 346 200m	0.7	0.2	160.5	250.8
SSE A 50m	1.6	-0.1	137.0	194.1	USGS/COE 346 400m	1.3	0.0	70.0	156.3
SSE A 80m	2.1	0.0	141.1	9.2	USGS/COE 346 800m	1.4	-0.6	157.5	213.7
SSE B 10m	2.2	-1.1	129.0	221.2	COE 1M 21m	2.4	0.5	88.7	146.1
SSE B 150m	1.5	-0.2	103.2	168.2	COE 1M 40m	1.6	0.8	70.6	122.1
SSE B 260m	1.5	0.5	134.5	164.7	COE B1B 21m	1.5	1.0	168.7	228.4
SSE B 390m	4.8	-0.3	136.8	191.7	COE B1B 46m	1.8	0.2	131.8	186.5
SSE C 10m	1.6	0.2	92.1	220.8	COE B1B 85m	1.7	-0.3	119.6	193.0
SSE C 75m	3.7	-1.5	61.1	197.5	CH2M Hill A 8m	4.8	-0.6	93.2	157.1
SSE C 150m	2.4	-1.5	78.2	199.5	CH2M Hill A 14m	5.7	-0.1	84.1	137.6
SSE C 250m	1.5	-1.1	98.9	181.9	CH2M Hill A 20m	4.0	0.8	78.0	114.1
SSE C 400m	2.3	-1.0	89.3	206.7	CH2M Hill B 8m	5.3	0.0	94.4	149.3
SSE C 790m	5.1	-2.3	129.0	222.8	CH2M Hill B 14m	2.5	0.7	166.8	325.5
SSE D 75m	1.4	-0.2	109.6	218.9	CH2M Hill C 8m	4.9	0.7	114.9	142.3
SSE D 250m	1.1	0.0	70.5	170.6	CH2M Hill D 8m	7.9	-0.1	87.3	155.0
SSE D 400m	1.0	-0.3	67.5	176.5	CH2M Hill E 8m	17.3	-0.5	69.3	167.4
SSE D 800m	2.5	-0.9	107.6	165.3	CH2M Hill E 14m	13.9	-1.4	67.1	166.7
SSE D 1390m	2.9	-0.1	118.7	171.5	CH2M Hill E 20m	9.5	-1.4	65.2	160.2
SSE E 75m	2.9	-0.7	140.0	120.9	CH2M Hill F 8m	4.1	0.0	81.3	153.2
SSE E 250m	1.0	0.0	33.1	152.2	CH2M Hill F 14m	2.6	0.6	50.9	117.8
SSE E 400m	1.1	0.2	108.6	186.9	CCCCS K 70m	4.5	-0.8	113.5	178.7
SSE E 800m	1.2	-0.2	142.0	211.9	CCCCS L 70m	3.4	-1.9	98.6	24.5
SSE E 1400m	1.0	-0.2	123.6	156.3	CCCCS L 210m	2.6	-0.9	98.4	1.1
SSE F 75m	1.4	-0.4	174.9	298.2	CCCCS L 470m	1.3	0.7	125.5	145.1
SSE F 150m	0.6	0.1	0.8	52.6	SuperCODE H3 35m	2.5	0.1	113.0	145.4
SSE F 250m	0.5	0.0	148.3	171.6	SuperCODE H3 65m	2.5	-0.1	88.4	165.0
SSE F 387m	0.4	0.0	72.2	86.0	SuperCODE H4 38m	3.6	-2.2	45.9	150.6
USGS/COE 334 30m	1.5	0.7	120.6	205.7	SuperCODE H4 70m	2.5	-1.4	105.4	168.5
USGS/COE 334 49m	1.5	0.5	105.7	189.4	SuperCODE H4 110m	2.8	-1.2	129.0	185.5
USGS/COE 335 30m	1.3	0.4	14.0	98.1					

Table A3 Ellipse characteristics for the S_2 tide calculated for each current meter deployed in the Gulf of the Farallones since 1981. Inclination is the bearing of the semi-major axis as measured counterclockwise from east (090°). Phase is the time in hours since 00:00 January 1, 1980 that the tide is oriented with the semi-major axis, divided by the tidal frequency (12.00 hours), multiplied 360°, and finally truncated to fall within 0-360°.

K1 Tidal Ellipse Characteristics									
Station Name and Depth	Semi-major Axis (cm/s)	Semi-minor Axis (cm/s)	Inclination (deg fm E)	Phase (deg)	Station Name and Depth	Semi-major Axis (cm/s)	Semi-minor Axis (cm/s)	Inclination (deg fm E)	Phase (deg)
Hickey RPI 10m	5.4	1.1	176.3	6.5	USGS/COE 335 59m	5.7	-1.0	134.3	185.5
SSE A 10m	5.3	-2.7	75.3	106.2	USGS/COE 346 200m	2.3	0.1	150.9	206.6
SSE A 50m	6.1	-3.3	88.6	112.6	USGS/COE 346 400m	2.1	-0.1	148.4	209.8
SSE A 80m	6.2	-2.2	125.0	143.3	USGS/COE 346 800m	1.8	-0.5	149.7	194.3
SSE B 10m	1.3	-0.8	88.2	143.3	COE 1M 21m	8.2	-2.9	88.3	113.6
SSE B 150m	2.8	-0.3	88.9	150.8	COE 1M 40m	4.5	0.0	120.6	134.2
SSE B 260m	2.0	-0.4	107.8	152.5	COE B1B 21m	6.0	-2.3	83.7	113.8
SSE B 390m	1.4	-0.4	133.4	165.8	COE B1B 46m	6.8	-3.5	84.1	115.6
SSE C 10m	0.7	0.0	53.7	310.7	COE B1B 85m	4.4	-1.4	126.2	145.1
SSE C 75m	1.7	-1.0	104.4	205.6	CH2M Hill A 8m	9.6	-5.7	97.5	103.4
SSE C 150m	2.8	-0.5	95.8	157.1	CH2M Hill A 14m	6.3	0.6	106.6	98.5
SSE C 250m	2.1	-0.2	91.9	157.0	CH2M Hill A 20m	7.0	3.3	137.0	131.7
SSE C 400m	1.3	0.3	70.6	172.8	CH2M Hill B 8m	8.7	-2.3	101.8	99.7
SSE C 790m	6.4	-1.8	78.6	155.5	CH2M Hill B 14m	2.7	0.2	16.9	20.9
SSE D 75m	2.0	-0.1	110.6	158.6	CH2M Hill C 8m	7.6	-0.3	117.1	67.4
SSE D 250m	1.8	0.0	101.8	162.2	CH2M Hill D 8m	12.7	-3.5	86.1	122.5
SSE D 400m	1.7	0.1	87.5	168.3	CH2M Hill E 8m	24.3	-2.5	71.5	145.6
SSE D 800m	2.0	-0.2	68.2	151.3	CH2M Hill E 14m	20.1	-4.1	66.1	147.4
SSE D 1390m	1.5	-1.2	129.8	147.0	CH2M Hill E 20m	15.3	-2.7	57.3	154.7
SSE E 75m	2.3	-1.3	177.1	313.9	CH2M Hill F 8m	15.3	-7.6	82.5	116.1
SSE E 250m	2.2	0.2	116.6	202.5	CH2M Hill F 14m	8.6	-0.1	105.2	120.7
SSE E 400m	1.9	0.1	119.2	194.0	CCCCS K 70m	7.1	-2.7	62.0	85.0
SSE E 800m	1.1	-0.2	121.8	179.6	CCCCS L 70m	2.0	-0.2	48.0	30.2
SSE E 1400m	1.5	-1.0	2.3	298.1	CCCCS L 210m	2.2	0.2	85.4	51.9
SSE F 75m	3.3	-1.0	114.3	147.6	CCCCS L 470m	3.3	0.4	97.7	110.8
SSE F 150m	4.2	0.1	121.3	177.0	SuperCODE H3 35m	6.4	-2.5	79.6	89.8
SSE F 250m	2.6	0.2	124.8	168.3	SuperCODE H3 65m	4.9	-1.4	95.9	105.9
SSE F 387m	0.3	0.0	170.9	106.6	SuperCODE H4 38m	5.9	-2.2	69.2	119.4
USGS/COE 334 30m	8.4	-3.4	100.9	150.9	SuperCODE H4 70m	7.3	-1.0	72.0	123.6
USGS/COE 334 49m	6.5	-1.5	122.2	166.2	SuperCODE H4 110m	6.1	-3.3	70.1	119.7
USGS/COE 335 30m	7.5	-2.8	112.1	160.9					

Table A4 Ellipse characteristics for the K₁ tide calculated for each current meter deployed in the Gulf of the Farallones since 1981. Inclination is the bearing of the semi-major axis as measured counterclockwise from east (090°). Phase is the time in hours since 00:00 January 1, 1980 that the tide is oriented with the major axis, divided by the tidal frequency (23.93 hours), multiplied 360°, and finally truncated to fall within 0-360°.

O1 Tidal Ellipse Characteristics									
Station Name and Depth	Semi-major Axis (cm/s)	Semi-minor Axis (cm/s)	Inclination (deg fm E)	Phase (deg)	Station Name and Depth	Semi-major Axis (cm/s)	Semi-minor Axis (cm/s)	Inclination (deg fm E)	Phase (deg)
Hickey RP1 10m	3.3	0.6	175.1	314.5	USGS/COE 335 59m	3.4	-0.8	127.5	109.5
SSE A 10m	2.7	-1.4	69.5	79.5	USGS/COE 346 200m	1.7	0.0	145.9	162.6
SSE A 50m	3.1	-1.6	79.7	72.5	USGS/COE 346 400m	1.3	0.2	138.2	168.7
SSE A 80m	3.0	-1.3	111.8	89.1	USGS/COE 346 800m	1.0	-0.2	161.6	183.7
SSE B 10m	0.6	0.1	171.4	99.7	COE 1M 21m	5.4	-2.6	86.0	65.1
SSE B 150m	1.3	0.0	83.0	115.3	COE 1M 40m	2.8	-0.4	109.0	75.9
SSE B 260m	0.9	-0.1	117.3	122.8	COE B1B 21m	3.4	-1.7	79.5	58.0
SSE B 390m	0.8	0.0	117.5	137.6	COE B1B 46m	3.8	-1.8	76.6	52.9
SSE C 10m	0.7	-0.4	10.9	0.8	COE B1B 85m	2.6	-1.0	112.7	76.5
SSE C 75m	0.9	0.3	115.8	101.9	CH2M Hill A 8m	5.3	-3.8	95.0	70.3
SSE C 150m	1.4	0.3	97.7	138.3	CH2M Hill A 14m	3.9	-0.2	92.5	45.8
SSE C 250m	1.0	0.2	73.4	109.8	CH2M Hill A 20m	2.7	1.9	167.5	121.1
SSE C 400m	1.2	0.0	92.9	144.7	CH2M Hill B 8m	5.4	-1.9	101.3	69.1
SSE C 790m	4.0	-1.0	80.8	115.3	CH2M Hill B 14m	2.5	-1.0	102.3	338.6
SSE D 75m	1.0	0.1	89.3	118.7	CH2M Hill C 8m	6.0	0.2	118.5	28.7
SSE D 250m	1.0	0.3	92.8	120.7	CH2M Hill D 8m	7.9	-3.4	85.9	101.4
SSE D 400m	1.1	0.1	82.6	135.1	CH2M Hill E 8m	15.6	-1.1	70.3	117.3
SSE D 800m	1.3	0.0	73.2	129.9	CH2M Hill E 14m	13.8	-3.3	59.5	121.7
SSE D 1390m	1.1	-0.6	103.1	130.7	CH2M Hill E 20m	11.6	-3.5	50.7	128.0
SSE E 75m	2.0	0.5	132.6	303.3	CH2M Hill F 8m	8.9	-6.4	94.3	73.4
SSE E 250m	1.4	0.3	113.2	169.0	CH2M Hill F 14m	4.8	-0.5	91.3	61.2
SSE E 400m	1.3	0.2	122.7	167.7	CCCCS K 70m	3.7	-1.0	46.5	15.6
SSE E 800m	0.8	-0.1	123.3	163.4	CCCCS L 70m	1.1	0.0	53.9	336.1
SSE E 1400m	0.8	-0.6	25.2	240.7	CCCCS L 210m	1.1	0.1	60.4	334.0
SSE F 75m	2.4	-1.0	105.1	114.0	CCCCS L 470m	1.6	0.2	100.4	236.3
SSE F 150m	2.9	0.0	122.5	142.1	SuperCODE H3 35m	2.7	-1.5	71.4	357.8
SSE F 250m	1.7	0.1	125.3	128.4	SuperCODE H3 65m	1.9	-0.8	86.8	15.6
SSE F 387m	0.3	0.0	166.5	55.0	SuperCODE H4 38m	2.5	-0.7	108.7	63.0
USGS/COE 334 30m	4.4	-2.6	91.7	977.1	SuperCODE H4 70m	3.2	-1.5	96.4	35.0
USGS/COE 334 49m	3.8	-1.8	112.1	105.4	SuperCODE H4 110m	2.2	-1.4	62.4	39.9
USGS/COE 335 30m	4.4	-1.7	104.6	94.3					

Table A5 Ellipse characteristics for the O₁ tide calculated for each current meter deployed in the Gulf of the Farallones since 1981. Inclination is the bearing of the semi-major axis as measured counterclockwise from east (090°). Phase is the time in hours since 00:00 January 1, 1980 that the tide is oriented with the semi-major axis, divided by the tidal frequency (25.82 hours), multiplied 360°, and finally truncated to fall within 0-360°.

APPENDIX B. CONSTRUCTING THE TIDAL MODEL

For m observations of velocity and n tidal frequencies, an m by $8n+4$ matrix A is created. The i^{th} row of matrix A is:

$$[1 \quad \lambda_i \quad \phi_i \quad z_i \quad \cos(2\pi\omega_1 t_i) \quad \lambda \cos(2\pi\omega_1 t_i) \quad \phi \cos(2\pi\omega_1 t_i) \quad z \cos(2\pi\omega_1 t_i) \quad \dots \\ \sin(2\pi\omega_1 t_i) \quad \lambda \sin(2\pi\omega_1 t_i) \quad \phi \sin(2\pi\omega_1 t_i) \quad z \sin(2\pi\omega_1 t_i) \quad \dots \\ \cos(2\pi\omega_2 t_i) \quad \lambda \cos(2\pi\omega_2 t_i) \quad \phi \cos(2\pi\omega_2 t_i) \quad z \cos(2\pi\omega_2 t_i) \quad \dots \\ \sin(2\pi\omega_2 t_i) \quad \lambda \sin(2\pi\omega_2 t_i) \quad \phi \sin(2\pi\omega_2 t_i) \quad z \sin(2\pi\omega_2 t_i) \quad \dots \\ \vdots \\ \cos(2\pi\omega_n t_i) \quad \lambda \cos(2\pi\omega_n t_i) \quad \phi \cos(2\pi\omega_n t_i) \quad z \cos(2\pi\omega_n t_i) \quad \dots \\ \sin(2\pi\omega_n t_i) \quad \lambda \sin(2\pi\omega_n t_i) \quad \phi \sin(2\pi\omega_n t_i) \quad z \sin(2\pi\omega_n t_i)]$$

The first four elements of each row represent the overall mean flow and steady flows that vary with longitude, latitude, and depth. Column vectors b_u and b_v of i length are created where each element is the u or v velocity observed. $Ac_u = b_u$ and $Ac_v = b_v$ are solved for column vectors c_u and c_v by inverting A , $c_u = A^{-1}b_u$ and $c_v = A^{-1}b_v$. Each c_u and c_v has $8n+4$ elements. The first four elements in c_u and c_v correspond to the mean flow, followed by four sets of eight elements. The elements of each set correspond to the coefficients a-h in the equation of the spatially varying model on page 47. Thus,

$$u_0(\lambda, \phi, z) = c_u(1) + c_u(2)\lambda + c_u(3)\phi + c_u(4)z \\ v_0(\lambda, \phi, z) = c_v(1) + c_v(2)\lambda + c_v(3)\phi + c_v(4)z$$

and at any time t the u and v tidal velocities at λ, ϕ, z , for frequency ω_k is:

$$\begin{aligned}u(\lambda, \phi, z, t) &= A_1 \cos(2\pi\omega_k t) + B_1 \sin(2\pi\omega_k t) \\v(\lambda, \phi, z, t) &= A_2 \cos(2\pi\omega_k t) + B_2 \sin(2\pi\omega_k t)\end{aligned}$$

where:

$$\begin{aligned}A_1 &= c_u(8k-3) + c_u(8k-2)\lambda + c_u(8k-1)\phi + c_u(8k)z \\B_1 &= c_u(8k+1) + c_u(8k+2)\lambda + c_u(8k+3)\phi + c_u(8k+4)z \\A_2 &= c_v(8k-3) + c_v(8k-2)\lambda + c_v(8k-1)\phi + c_v(8k)z \\B_2 &= c_v(8k+1) + c_v(8k+2)\lambda + c_v(8k+3)\phi + c_v(8k+4)z\end{aligned}$$

However, tidal currents are in many ways easier to express as the sum of clockwise and counterclockwise rotating vectors (Godin, 1972), $U = u + iv = U_+ e^{i\omega t} + U_- e^{-i\omega t}$. Here, $e^{i\omega t}$ and $e^{-i\omega t}$ are unit vectors rotating in opposite directions and U_+ and U_- are complex quantities representing the vector magnitudes.

$$\begin{aligned}|U_+| &= \frac{1}{2}[(A_1 + B_2)^2 + (A_2 - B_1)^2]^{\frac{1}{2}} \\|U_-| &= \frac{1}{2}[(A_1 - B_2)^2 + (A_2 + B_1)^2]^{\frac{1}{2}}\end{aligned}$$

And the length of the ellipse axes are:

$$\begin{aligned}\text{major axis} &= |U_+| + |U_-| \\ \text{minor axis} &= |U_+| - |U_-|\end{aligned}$$

The sign of the semi-minor axis gives the sense of the tides rotation; positive means counterclockwise and negative means clockwise. The orientation of the semi-major axis with respect to east is:

$$\theta = \frac{1}{2} \tan^{-1} \left[\frac{2(A_1 A_2 + B_1 B_2)}{A_1^2 + B_1^2 - A_2^2 - B_2^2} \right]$$

and the phase of the semi-major axis is:

$$\tau = \frac{1}{2} \tan^{-1} \left[\frac{2(A_1 B_1 + A_2 B_2)}{A_1^2 - B_2^2 + A_2^2 - B_1^2} \right]$$

LIST OF REFERENCES

- Allen, J.T., Subtidal and tidal currents in the vicinity of the Iceland-Færøes front, *J. Atmos. Oceanic Tech.*, 12, 567-588, 1995.
- Bratkovich, A., R.L. Bernstein, D.B. Chelton, and P.M. Kosro, Central California coastal circulation study: program overview and representative results, in *Southern California Bight Physical Oceanography, Proceedings of a Workshop*, pp. 91-109, OCS Study MMS 91-0033, 1991.
- Bray, N.A. and C.L. Greengrove, Circulation over the shelf and slope off northern California, *J. Geophys. Res.*, 98, 18,119-18,145, 1993.
- Candela J., R.C. Beardsley, and R. Limeburner, Removing tides from ship-mounted ADCP data, with application to the Yellow Sea, in *Proceedings of the IEEE Fourth Working Conference on Current Measurements*, edited by G.F. Appell and T.B. Curtin, pp. 258-266, Institute of Electrical and Electronics Engineers, New York, 1990.
- Candela, J., R.C. Beardsley, and R. Limeburner, Separation of tidal and subtidal currents in ship-mounted acoustic doppler current profiler observations, *J. Geophys. Res.*, 97, 769-788, 1992.
- Cartwright, D.E. and R.D. Ray, Energetics of global ocean tides from Geosat altimetry, *J. Geophys. Res.*, 96, 16897-16912, 1991.
- CH2M Hill, Wastewater transport and bacteriological compliance studies of the San Francisco ocean outfall, City and County of San Francisco, 1989.
- Chelton, D.B., Seasonal variability of alongshore geostrophic velocity off central California, *J. Geophys. Res.*, 89, 3473-3486, 1984.
- Chelton, D.B., R.L. Bernstein, A. Bratkovich, and P.M. Kosro, The central California coastal circulation study, *EOS Trans. AGU*, 68(1), 12-13, 1987.
- Chelton, D.B., A.W. Bratkovich, R.L. Bernstein, and P.M. Kosro, Poleward flow off central California during the Spring and Summer of 1981 and 1984, *J. Geophys. Res.*, 93, 10604-10620, 1988.
- Christensen, N., Observations of the Cromwell Current near the Galapagos Islands. *Deep-Sea Research*, 18, 27-33, 1971.

Clarke, A.J., Theoretical understanding of eastern ocean boundary poleward undercurrents, in *Poleward Flows Along Eastern Oceanic Boundaries, Coastal Estuarine Stud.*, no. 34, pp. 26-39, Springer-Verlag, New York, 1989.

Climate Analysis Center, Climate Diagnostics Bulletin, November, 1993. NOAA, U.S. Department of Commerce, 74 pp., 1993.

Climate Analysis Center, Climate Diagnostics Bulletin, February, 1994. NOAA, U.S. Department of Commerce, 80 pp., 1994.

Collins, C.A., R.G. Paquette, and S.R. Ramp, Annual variability of ocean currents at 350-m depth over the continental slope of Point Sur, California, *Calif. Coop. Oceanic Fish. Invest. Rep.*, 37, 257-263, 1996.

Crabbs, D.E., Analysis of ocean current meter records obtained from a 1975 deployment off the Farallon Islands, California, Interstate Electronics Corp., Anaheim, CA, 68 pp., 1983.

Denbo, D.W., K. Polzin, J.S. Allen, A. Huyer, and R.L. Smith, Current meter observations over the continental shelf off Oregon and California, February 1981 - January 1984, Data Rpt 112, Oregon State University, 7 chapters + appendix, 1984.

Dowd, M. and K.R. Thompson, Extraction of tidal streams from ship-borne acoustic Doppler current profiler using a statistical-dynamical model, *J. Geophys. Res.*, 101, 8943-8956, 1996.

Egbert, G., A.F. Bennett, and M.G. Foreman, Topex/Poseidon tides estimated using a global inverse model, *J. Geophys. Res.*, 99, 24821-24852, 1994.

Ekman, V.W., On the influence of the earth's rotation on ocean currents, *Arkiv for Matematik, Astronomi, och Fysik*, 2, 1-52, 1905.

Feldman, G. C., Patterns of the phytoplankton production around the Galapagos Islands. In: J. Brown, M. Yentsch and W. T. Peterson (Editors), *Tidal Mixing and Plankton Dynamics: Notes on Coastal and Estuarine Studies*, Springer, Berlin, 77-106, 1986.

Firing, E., Deep zonal currents in the central equatorial Pacific. *J. Marine Res.* 45(4) 791-812, 1987.

Flament, P., A note on seawater spiciness and diffusive stability, unpublished, 1986.

Foreman, M.G.G, Tidal analysis program package, Pacific Marine Science Report 78-6, Institute of Ocean Sciences, 70 pp., 1978.

- Foreman, M.G.G. and H.J. Freeland, A comparison of techniques for tide removal from ship-mounted acoustic doppler measurements along the southwest coast of Vancouver Island, *J. Geophys. Res.*, 96, 17,007-17,021, 1991.
- Geyer, W.R. and R. Signell, Measurements of tidal flow around a headland with a shipboard acoustic doppler current profiler, *J. Geophys. Res.*, 95, 3189-97, 1990.
- Gezgin, E., A study on hydrographic conditions and salt budget calculation for the Gulf of the Farallones with the data collected in August 1990, M.S. Thesis, Naval Postgraduate School, Monterey, CA, 82 pp., 1991.
- Godin, G.G., The Analysis of Tides, Univ. Of Toronto Press, 264pp., 1972.
- Hayes, S. P., Sea level and near surface temperature variability at the Galápagos Islands, 1979-1983. In: El Niño in the Galápagos Islands: The 1981-1983 Event, G. Robinson and E. Del Pino, editors, Charles Darwin Foundation for the Galápagos Islands, Quito, 49-81, 1985.
- Hayes, S. P., L. J. Mangum, R. T. Barber, A. Huyer, and R. L. Smith, Hydrographic variability west of the Galapagos Islands during the 1982-93 El Niño, *Prog. Oceanog.*, 17, 137-162, 1986.
- Hellerman, S. and M. Rosenstein, Normal monthly wind stress over the world ocean with error estimates, *J. Phys. Oceanogr.*, 13, 1093-1104, 1983.
- Hendershott, M.C., Ocean tides, EOS Trans. AGU, 54, 76-86, 1973.
- Hickey, B.M., The California current system - hypotheses and facts, *Prog. Oceanog.*, 8, 191-279, 1979.
- Hickey, B.M., Alongshore coherence on the Pacific Northwest continental shelf, *J. Phys. Oceanogr.*, 11, 822-835, 1981.
- Huyer, A. and P.M. Kosro, Mesoscale surveys over the slope and shelf in the upwelling region near Point Arena, California, *J. Geophys. Res.*, 92, 1655-1682, 1987.
- Huyer, A. and R.L. Smith, Observations of a poleward undercurrent over the continental slope off Oregon, May-June 1975, *Trans. Am. Geophys. Union*, 57, 263, 1976.
- Huyer, A., P.M. Kosro, S.J. Lentz, and R.C. Beardsley, Poleward flow in the California Current system, in *Poleward Flows Along Eastern Oceanic Boundaries, Coastal Estuarine Stud.*, no. 34, pp. 142-156, Springer-Verlag, New York, 1989.

Interstate Electronics Corporation, Farallon Islands oceanographic data analysis, vol I and II, Final Report to the Office of Radiation Programs, U.S. Environmental Protection Agency, Washington, D.C., 1982.

Jessen, P.F., S.R. Ramp, C.A. Collins, N. Garfield, L.K. Rosenfeld, and F.B. Schwing, Hydrographic and acoustic doppler current profiler (ADCP) data from the Farallones shelf and slope study 13-18 February 1991, Naval Postgraduate School Technical Report NPS-OC-92-003, Monterey, CA, 168 pp., 1992a.

Jessen, P.F., S.R. Ramp, C.A. Collins, N. Garfield, L.K. Rosenfeld, and F.B. Schwing, Hydrographic and acoustic doppler current profiler (ADCP) data from the Farallones shelf and slope study 16-21 May 1991, Naval Postgraduate School Technical Report NPS-OC-92-004, Monterey, CA, 171 pp., 1992b.

Jessen, P.F., S.R. Ramp, C.A. Collins, N. Garfield, L.K. Rosenfeld, and F.B. Schwing, Hydrographic and acoustic doppler current profiler (ADCP) data from the Farallones shelf and slope study 7-17 February 1992, Naval Postgraduate School Technical Report NPS-OC-92-005, Monterey, CA, 139 pp., 1992c.

Jessen, P.F., S.R. Ramp, C.A. Collins, N. Garfield, L.K. Rosenfeld, and F.B. Schwing, Hydrographic and acoustic doppler current profiler (ADCP) data from the Farallones shelf and slope study 29 October - 3 November 1991, Naval Postgraduate School Technical Report NPS-OC-92-007, Monterey, CA, 183 pp., 1992d.

Johnson, J.E., An assessment of data requirements for quasi-geostrophic nowcasts and hindcasts of a mesoscale eddy field in the California Current System with application to the Fall Transition, Ph.D. Dissertation, Naval Postgraduate School, Monterey, CA, 345 pp., 1990.

Joyce, T. M., On in situ calibration of shipboard ADCPs, *J. Atmos. Ocean. Tech.*, 6, 169-172, 1989.

Katoh, O., K. Teshima, O. Abe, H. Fujita, K. Miyaji, K. Moriga, and N. Nakagawa, Process of Tsushima current formation revealed by ADCP measurements in summer, *J. of Oceanography*, 52, 491-507, 1996.

Kinoshita, K., M. Noble, and S.R. Ramp, The Farallones moored array data report, USGS, Menlo Park, CA, 1992.

Kinsella, A., Numerical solutions for error evaluation, *Am. J. of Physics*, 54, 464-466, 1986.

Knauss, J. A., Measurements of the Cromwell Current. *Deep-Sea Research*, 6(4), 265-285, 1960.

Knauss, J. A. , Further measurements and observations on the Cromwell Current. *J. Mar. Res.*, 24(2), 205-240, 1966.

Largier, J. L., Hydrodynamic exchange between San Francisco Bay and the ocean: the role of ocean circulation and stratification, pages 69-104 in San Francisco Bay: the Ecosystem, ed. J.T. Hollinbaugh, American Assoc. for the Advancement of Sci., San Francisco, CA, 1996.

Leetmaa, A., Observations of near-equatorial flows in the eastern Pacific. *J. Mar. Res.*, 40 (supplement), 357-370, 1982.

Leetmaa, A. and D. Wilson, Characteristics of near surface circulation patterns in the eastern equatorial Pacific, *Prog. Oceanogr.*, 14, 339-352, 1985.

Lukas, R., The termination of the Equatorial Undercurrent in the Eastern Pacific, *Prog. Oceanog.* (16), 63-90, 1986.

Lynn, R.J., K.A. Bliss, and L.E. Eber, Vertical and horizontal distributions of seasonal mean temperature, salinity, sigma- t , stability, dynamic height, oxygen and oxygen saturation in the California Current, 1950-1978, *CalCOFI Atlas 30*, 513 pp., State of Calif. Mar. Res. Comm., La Jolla, 1982.

Lynn, R.J. and J.J. Simpson, The California Current system: the seasonal variability of its physical characteristics, *J. Geophys. Res.*, 92, 12,947-12,966, 1987.

Lynn, R.J., F.B. Schwing, and T.L. Hayward, The effect of the 1991-1993 ENSO on the California Current system, *Calif. Coop. Oceanic Fish. Invest. Rep.*, 36, 57-71, 1995.

Martin, J. H., K. H. Coale, K. S. Johnson, S. E. Fitzwater, R. M. Gordon, S. J. Tanner, C. N. Hunter, V. A. Elrod, J. L. Coley, R. T. Barber, S. Lindley, A. J. Watson, K. Van Scoy, C. S. Law, M. I. Liddicoat, R. Ling, T. Stanton, J. Stockel, C. Collins, A. Anderson, R. Bidigare, M. Ondrusek, M. Latasa, F. J. Millero, K. Lee, W. Yao, J. Z. Zhang, G. Friederich, C. Sakamoto, F. Chavez, K. Buck, Z. Kolber, R. Greene, P. Falkowski, S. W. Chisholm, F. Hoge, R. Swift, J. Yungel, S. Turner, P. Nightingale, A. Hatton, P. Liss, and N. W. Tindale, Testing the iron hypothesis in ecosystems of the equatorial Pacific Ocean, *Nature*, 371, 123-129, 1994.

McCreary, J.P., P.K. Kundu, and S.-Y. Chao, On the dynamics of the California Current system, *J. Mar. Res.*, 45, 1-32, 1987.

- Miller, B. H., V. N. Anderson, and C. A. Collins, Hydrographic data from equatorial Pacific waters near the Galapagos, November 1993, NPS Tech. Rpt. NPS-OC-94-002, Naval Postgraduate School, Monterey, CA, 54 pp, 1994.
- Mofjeld, H.O., F.I. Gonzalez, and M.C. Eble, Ocean tides in the continental margin off the Pacific northwest shelf, *J. Geophys. Res.*, 100, 10,789-10,800, 1995.
- Morgan, P.P., SEAWATER: a library of MATLAB computational routines for the properties of sea water, CSIRO Marine Laboratories Rep. 222, Tasmania, Australia, 1994.
- Nelson, C.S., Wind stress and wind stress curl over the California current, U.S. Dept. Of Commer., NOAA Tech. Rep. NMFS-SSRF-714, 89 pp., 1977.
- Noble, M., L.K. Rosenfeld, R.L. Smith, J.V. Gardner, and R.C. Beardsley, Tidal currents seaward of the northern California continental shelf, *J. Geophys. Res.*, 92, 1733-1744, 1987.
- Noble, M. and G. Gelfenbaum, A pilot study of currents and suspended sediment in the Gulf of the Farallones, USGS, Menlo Park, CA, 90 pp., 1990.
- Pak, H. and J. R. V. Zaneveld, The Cromwell Current on the east side of the Galapagos Islands, *J. Geophys. Res.* 78, 7845-7859, 1973.
- Parker, H.A., Variations in coastal circulation off central California, spring-summer of 1993, 1994, 1995, 1996, M.S. Thesis, Naval Postgraduate School, Monterey, CA, 1996.
- Pavlova, Y.V., Seasonal variations of the California Current, *Oceanology*, 6, 806-814, 1966.
- Petruncio, E.T., Observations and modeling of the internal tide in a submarine canyon, Ph.D. Dissertation, Naval Postgraduate School, Monterey, CA, 181 pp., 1996.
- Petrick, E.P., C.A. Collins, and W.C. Boicourt, Currents through the Golden Gate, pages 105-122 in San Francisco Bay: the Ecosystem, ed. J.T. Hollinbaugh, American Assoc. for the Advancement of Sci., San Francisco, CA, 1996.
- Pollard, R. and J. Read, A method for calibrating shipmounted acoustic Doppler profilers and the limitations of gyro compasses, *J. Atmos. Ocean. Tech.*, 6, 859-865, 1989.
- Pond, S. and G.L. Pickard, Introductory Dynamical Oceanography, 2nd ed., Pergamon Press, Oxford, 329 pp., 1983.

Prazuck, C., Anomalous diurnal currents in the vicinity of the Yermak Plateau, Ph.D. Dissertation, Naval Postgraduate School, Monterey, CA, 125 pp., 1991.

R D Instruments, Acoustic Doppler current profilers Principles of operation: a practical primer. Available from RD Instruments, 9855 Businesspark Av., San Diego, CA 92131, 39 pp., 1989.

R D Instruments, TRANSECT Users Manual for Narrow Band ADCPs, R. D. Instruments, San Diego, CA, 1992.

Rago, T.A., L.K. Rosenfeld, P.F. Jessen, S.R. Ramp, C.A. Collins, N. Garfield, and F.B. Schwing, Hydrographic and acoustic doppler current profiler (ADCP) data from the Farallones shelf and slope study 12-18 August 1991, Naval Postgraduate School Technical Report NPS-OC-92-006, Monterey, CA, 186 pp., 1992.

Ramp, S.R., N. Garfield, C.A. Collins, L.K. Rosenfeld, and F. Schwing, Circulation studies over the continental shelf and slope near the Farallon Islands, CA, Naval Postgraduate School Technical Report NPS-OC-95-004, Monterey, CA, 1995.

Ramp, S.R., J.L. McClean, C.A. Collins, A.J. Semtner, and K.A.S. Hays, Observations and modeling of the 1991-1992 El Niño signal off central California, *J. Geophys. Res.*, 102, 5553-5582, 22 pp., 1997.

Reid, J.L. Jr. and A. W. Mantyla, The effects of the geostrophic flow upon coastal sea elevations in the northern Pacific Ocean, *J. Geophys. Res.*, 81, 3100-3110, 1976.

Rosenfeld, L.K., and R.C. Beardsley, Barotropic semidiurnal tidal currents off northern California during the Coastal Ocean Dynamics Experiment (CODE), *J. Geophys. Res.*, 92, 1721-1732, 1987.

Rosenfeld, L.K., F.B. Schwing, N. Garfield, and D.E. Tracy, Bifurcated flow from an upwelling center: a cold source for Monterey Bay, *Cont. Shelf Res.*, 14, 931-964, 1994.

Sakuma, K.M., F.B. Schwing, K. Baltz, D. Roberts, H.A. Parker, and S. Ralston, The physical oceanography off the central California coast during May-June 1995: a summary of CTD data from pelagic juvenile rockfish surveys, NOAA Tech. Rep. NOAA-TM-NMFS-231, US Dept of Commer., 144 pp., 1996.

Schwiderski, E. W., Atlas of Ocean Tidal Charts and Maps, Part I: The Semidiurnal Principal Lunar Tide M2, *Marine Geodesy* 6(3-4) 219-265, 1983.

- Schwing, F.B., D.M. Husby, N. Garfield, and D.E. Tracy, Mesoscale oceanic response to wind events off central California in Spring 1989: CTD surveys and AVHRR imagery, *CalCOFI Reports*, 32, 47-62, 1991.
- Schwing, F.B., M. O'Farrell, J. Steger, and K. Baltz, Coastal upwelling indices, west coast of North America 1946-1995, NOAA Tech. Rep. NOAA-TM-NMFS-SWFSC-231, US Dept of Commer., 207 pp., 1996.
- Send, U., R.C. Beardsley, and C.D. Winant, Relaxation from upwelling in the Coastal Ocean Dynamics Experiment, *J. Geophys. Res.*, 92, 1683-1698, 1987.
- Sherwood, C.R., D. Coats, and B. Walls, Current and suspended sediment measurements on the central California continental shelf, in proceedings of Oceans '89 conference, pp. 320-325, IEEE pub no. 89CH2780-5, 1989.
- Simpson, J. H. and J. R. Hunter, Fronts in the Irish Sea, *Nature*, 250, 404-406, 1974.
- Steiner, M., Detiding shipboard-mounted ADCP data: an analysis of model data and observations using a polynomial interpretation method, M.S. Thesis, Naval Postgraduate School, Monterey, CA, 83 pp., 1994.
- Strub, P.T., J.S. Allen, A. Huyer, and R.L. Smith, Seasonal cycles of currents, temperatures, winds, and sea level over the northeast Pacific continental shelf: 35°N to 48°N, *J. Geophys. Res.*, 92, 1507-1526, 1987.
- Tisch, T.D., S.R. Ramp, and C.A. Collins, Observations of the geostrophic current and water mass characteristics off Point Sur, California, from May 1988 through November 1989, *J. Geophys. Res.*, 97, 12,535-12,555, 1992.
- Wickham, J.B., A.A. Bird, and C.N.K. Mooers, Mean and variable flow over the central California continental margin, 1978-1980, *Cont. Shelf Res.*, 7, 827-849, 1987.
- Winant, C.D., R.C. Beardsley, and R.E. Davis, Moored wind, temperature, and current observations made during Coastal Ocean Dynamics Experiments 1 and 2 over the northern California continental shelf and upper slope, *J. Geophys. Res.*, 92, 1569-1604, 1987.
- Wyllie, J.G., Geostrophic flow of the California Current at the surface and at 200 m, *CalCOFI Atlas 4*, 303 pp., State of Calif. Mar. Res. Comm., La Jolla, 1966.
- Wyrtki, K. and B. Kilonsky, Mean water and current structure during the Hawaii-to-Tahiti Shuttle Experiment, *J. Phys. Oc (14)*, 242-254, 1984.
- Wyrtki, K., Circulation and water masses in the eastern equatorial Pacific Ocean, *Int. J. Oceanology and Limnology 1(2)*, 117-147, 1967.

INITIAL DISTRIBUTION LIST

	No. Copies
1. Defense Technical Information Center 8725 John J. Kingman Rd., STE 0944 Ft. Belvoir, VA 22060-6218	2
2. Dudley Knox Library Naval Postgraduate School 411 Dyer Rd. Monterey, CA 93943-5101	2
3. Dr. Curtis A. Collins Department of Oceanography Naval Postgraduate School Monterey, CA 93943-5121	1
4. Dr. Franklin B. Schwing NOAA Pacific Fisheries Environmental Laboratory 1352 Lighthouse Ave. Pacific Grove, CA 93950	1
5. Dr. Leslie K. Rosenfeld Department of Oceanography Naval Postgraduate School Monterey, CA 93943-5121	1
6. Dr. Newell Garfield Department of Oceanography Naval Postgraduate School Monterey, CA 93943-5121	1
7. Library Scripps Institute of Oceanography University of California at San Diego La Jolla, CA 92093	1
8. LCDR John M. Steger, NOAA NOAA Ship RAINIER 1801 Fairview Ave. East Seattle, WA 98102	1

9. Dr. Steve Ramp 1
Code 32
Office of Naval Research
800 N. Quincy St.
Arlington, VA 22217-5660
10. Dr. Marlene Noble 1
U.S. Geological Survey
Mailstop 79
345 Middlefield Rd.
Menlo Park, CA 93025
11. Mr. Ed Ueber 1
Gulf of the Farallones National Marine Sanctuary
Fort Mason
San Francisco, CA 94123
12. Mr. William van Peters, Code 2032WP 1
Naval Facilities Engineering Command
Western Division
P.O. Box 727
San Bruno, CA 94066
13. Mr. Alan Ota 1
U.S. Environmental Protection Agency
Region IX
75 Hawthorne St.
San Francisco, CA 94105